Doctoral Thesis

Solution-Processed Oxide and Sulfide Semiconductors for Thin-Film Electronics

Jungwoo Heo

Department of Physics

Graduate School of UNIST

2019

Solution-Processed Oxide and Sulfide Semiconductors for Thin-Film Electronics

Jungwoo Heo

Department of Physics

Graduate School of UNIST

Solution-Processed Oxide and Sulfide Semiconductors for Thin-Film Electronics

A thesis/dissertation
submitted to the Graduate School of UNIST
in partial fulfillment of the
requirements for the degree of
Doctor of Philosophy

Jungwoo Heo

11/27/2018 of submission

Approved by

Advisor
Jin Young Kim

Solution-Processed Oxide and Sulfide Semiconductors for Thin-Film Electronics

Jungwoo Heo

This certifies that the thesis/dissertation of Jungwoo Heo is approved.

11/27/2018 of submission

signature

Advisor: Jin Young Kim

signature

Jun Hee Lee: Thesis Committee Member #1

signature

Hyesung Park: Thesis Committee Member #2

signature

Young Chul Jun: Thesis Committee Member #3

signature

Jung Hwa Seo: Thesis Committee Member #4

Abstract

Solution-processing of metal oxides and sulfides is considered as one of the promising electronics technologies due to its simple, cheap, and large-area processability. This thesis covers developing solution-processing techniques for metal oxides and sulfides, and their device applications. Firstly, newly developed sol-gel method for amorphous HfO_2, ZrO_2, and Ta_2O_5 is introduced. The processed oxides exhibited high visible transparency and dielectric constant (κ), and excellent electrical insulation. Then, they were applied to thin film transistors (TFTs) as high-κ gate dielectrics. The incorporation of solution-processed metal oxides led to the devices exhibiting comparable field-effect mobility and significantly reduced operating voltage (~ 95% reduction) than the devices with a conventional SiO_2 gate dielectric. Next chapter is devoted to the introduction of efficient and universal metal sulfide precursors. Simple mixing of alkanethiolates with metal acetates (or isopropoxides) allowed the formation of soluble metal thiolates, which are the resultant precursors for metal sulfides. Decomposition of metal thiolates occurred via SN_1 reaction, giving carbon-free metal sulfide films with volatile dialkylsulfide byproducts. It is further found that mixing two (or three) precursors results in ternary (or quaternary) sulfide compounds. Based on this, CdS TFTs and $CuInS_2$ thin film solar cells are fabricated and characterized. Following chapters deal with another solution-processing approach, synthesizing colloidal nanoparticles. To prepare efficient electron transporting layer for polymer solar cells, colloidal ZnO and TiO_2 nanoparticles are prepared. By using the nanoparticle solutions, ZnO and TiO_2 thin films were successfully deposited on ITO substrates without any possible damages to pre-coated Ag quantum dots on the substrates. It is observed that surface plasmon resonance peaks are strongly affected by the refractive index of surrounding oxide medium. Computer simulation further unveils detailed behavior of incident photons interacting with Ag quantum dots surrounded by solution-processed metal oxide media. Finally, simple and efficient strategy to boost colloidal stability of ZnO nanoparticles are discussed. The addition of a coordination complex, titanium diisopropoxide bis(acetylacetonate) significantly improved colloidal stability of ZnO nanoparticles in methanol, isopropanol, and chlorobenzene. Acetylacetonates on the surface of the nanoparticles effectively reduced the aggregation between the nanoparticles and the electron donation from Ti filled up deep level traps, which results in the reduced trap-assisted radiative recombination. In the device applications, it is confirmed that the colloidal stability of functionalized ZnO nanoparticles is prolonged at least 2 months. Not only comparable material properties of solution-processed oxide and sulfide thin films with those of the films prepared via conventional processing, but additional positive contributions to the device performance show their great potential for thin film electronics technology.

Table of Contents

List of Figures

List of Tables

Abbreviation

Abbreviation	Description
TFT	thin film transistors
PD	photodiode
SC	solar cell
TFSC	thin film solar cell
QD	quantum dot
PSC	polymer solar cell
PCE	power conversion efficiency
Acac	acetylacetone or acetylacetonate
CB	conduction band
VB	valance band
HOMO	the highest occupied molecular orbital
LUMO	the lowest occupied molecular orbital
AM	airmass
EQE	external quantum efficiency
IPCE	incident photon to electron conversion efficiency
IQE	internal quantum efficiency
FET	field effect transistor
DVI	digital visual interface
HDMI	high definition multimedia interface
P3HT	poly(3-hexylthiophene)
PCBM	phenyl-c61-butyric acid methyl ester
ITO	indium tin oxide
TNT	t-nonanethiol or t-nonanethiolate
PTFE	polytetrafluoroethylene
AFM	atomic force microscope

XRD	X-ray diffraction
HREELS	high resolution electron energy loss spectroscopy
OiPr	isopropoxide
OEt	ethoxide
XPS	X-ray photoelectron spectrum
OFET	organic FET
TDT	t-dodecanethiol or t-dodecanethiolate
TGA	thermogravimetric
RMS	root-mean-square
PTB7	poly[[4,8-bis[(2-ethylhexyl)oxy]benzo[1,2-b:4,5-b′]dithiophene-2,6-diyl][3-fluoro-2-[(2-ethylhexyl)carbonyl]thieno[3,4]thiophenediyl]]
BHJ	bulk heterojunction
DSSC	dye-sensitized solar cells
CQD	colloidal quantum dot solar cells
NP	nanoparticle
TBOC	t-butoxy carbonyl
TAMT	tertiary-alkyl metal thiolate
THF	tetrahydrofuran
MS	gas chromatography – mass spectrometry
MW	molecular weight
SEM	scanning electron micrograph
UPS	ultraviolet photoelectron spectrum
ESE	electron secondary edgy
CIGS	copper indium gallium sulfide selenide
2D Ag QA	two-dimensional ag quantum dot array
ETL	electron transport layer
BCML	block copolymer micellar lithography
PS-*b*-P2VP	polystyrene-*block*-poly(2-vinylpyridine)
LSPR	localized surface plasmon resonance
DDA	discrete dipole approximation

PC71BM	[6,6]-phenyl c_{71} butyric acid methyl ester
fZnO	functionalized ZnO
pZnO	pristine ZnO
PTB7-Th	poly[4,8-bis(5-(2-ethylhexyl)thiophen-2-yl)benzo[1,2-b;4,5-b']dithiophene-2,6-diyl-alt-(4-(2-ethylhexyl)-3-fluorothieno[3,4-b]thiophene-)-2-carboxylate-2-6-diyl)]
ITIC	3,9-bis(2-methylene-(3-(1,1-dicyanomethylene)-indanone))-5,5,11,11-tetrakis(4-hexylphenyl)-dithieno- [2,3-d:2′,3′-d′]-s-indaceno[1,2-b:5,6-b′]dithiophene
PBDB-T	poly[(2,6-(4,8-bis(5-(2-ethylhexyl)thiophen-2-yl)-benzo[1,2-b:4,5-b']dithiophene))-alt-(5,5-(1',3'-di-2-thienyl-5',7'-bis(2-ethylhexyl)benzo[1',2'-c:4',5'-c']dithiophene-4,8-dione)]
IT-M	3,9-bis(2-methylene-((3-(1,1-dicyanomethylene)-6/7-methyl)-indanone))-5,5,11,11-tetrakis(4-hexylphenyl)-dithieno[2,3-d:2',3'-d']-s-indaceno[1,2-b:5,6-b']dithiophene
IEICO-4F	2,2'-((2z,2'z)-(((4,4,9,9-tetrakis(4-hexylphenyl)-4,9-dihydro-s-indaceno[1,2-b:5,6-b']dithiophene-2,7-diyl)bis(4-((2-ethylhexyl)oxy)thiophene-5,2-diyl))bis(methanylylidene))bis(5,6-difluoro-3-oxo-2,3-dihydro-1h-indene-2,1-diylidene))dimalononitrile
PL	photoluminescence
GL	green luminescence
PEDOT:PSS	poly(3,4-ethylenedioxythiophene) polystyrene sulfonate

CHAPTER 1. Introduction

Since 3rd industrial revolution, we are living in an era where we are not able to predict the near-future lifestyle. You work with computers in your company, communicate with someone far away. The progress on mobile payment technology made you no longer need to carry paper money to buy things. No one could imagine watching 4K movies or TV shows with a massive screen in your room via live streaming. Most of cars on the road will be driverless cars in the near future. Our life is being affected by the development of electronics technology.

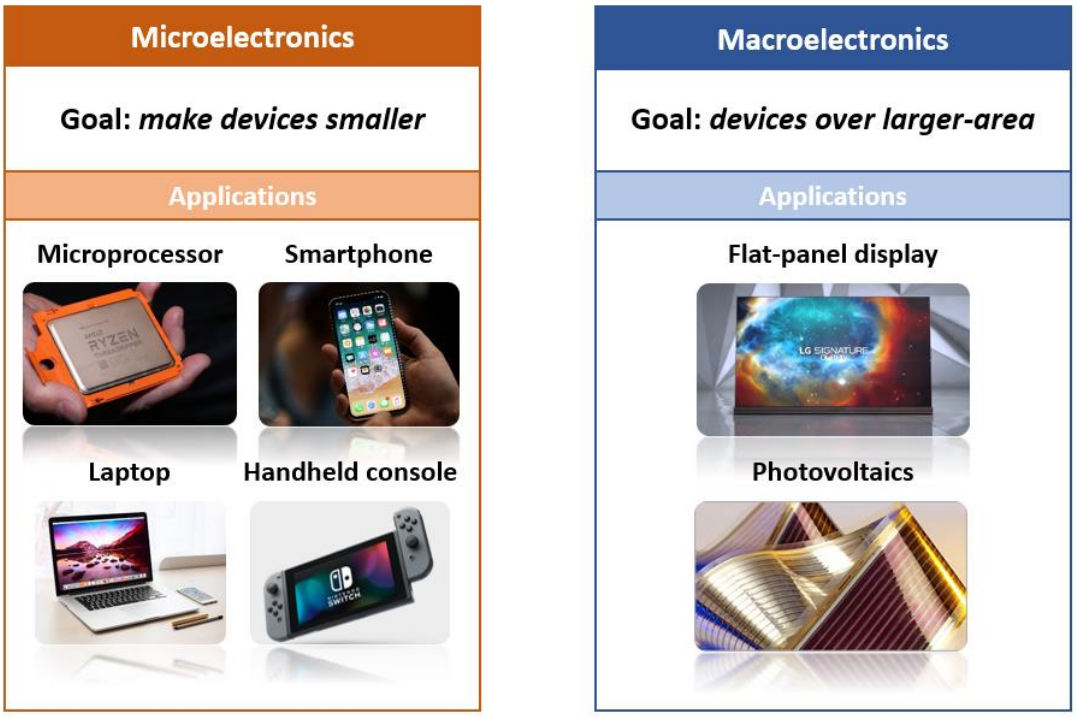

Figure 1. 1. Summary of two mainstreams in electronics research

There are two mainstreams in electronics research. Most studies on microelectronics focus on making device smaller. Integrating microelectronic devices on a limited area with higher spatial density allows an improved performance of electronic devices.[1-3] For example, a single Apple iPhone 4, released in 2010, performs equal processing power of the supercomputer, Cray-2, made by Cray Research in 1985. While, a goal of macroelectronics is making devices over larger area. Thin film electronic devices such as thin film transistors (TFTs), photodiodes (PDs), flat panel displays, and solar cells (SCs) are representatives of macroelectronic devices.[4-5]

Oxide and sulfide semiconductors have played a vital role in thin film electronic devices due to its

superior (opto)electronic properties. Most oxide semiconductors exhibit high transmittance as well as a wide range of electrical conductivity from insulating to metallic, which are preferable for thin-film transistors and transparent electrodes and buffer layers in optoelectronic devices.[6-7] Sulfide semiconductors have superior charge carrier mobility with a narrower optical bandgap, which is suitable for light-harvesting devices or photodiode.[8-9]

Keeping the goal of macroelectronics in mind, it is critical issue to prepare oxide and sulfide semiconductors-based thin film over larger area. Solution-processing is a promising technique to deposit large-area thin film on an arbitrary substrate.[10-11] Briefly, solution-processing is a technique to make thin films on substrates from “solution”. Inkjet printer is one example of solution-processing; ink(solution) is propelled onto paper to express letters or images. Solution-processing techniques include inkjet printing,[12] slot-die coating,[13] blade coating,[14] spray coating,[15] spin-coating,[16] and even 3d printing,[17] which are suitable for large area processing.

The simplest method to solution-process oxide or sulfide semiconductors on substrates is dissolving target materials in an appropriate solvent. However, oxide or sulfide semiconductors are soluble in extreme chemical environments such as highly acidic or basic solvent in most cases, by losing its original chemical structures.[18-19] As a result, developing proper solution for the deposition of oxide and sulfide semiconductor thin film has been attractive research topic in the corresponding research field.

Many attempts have been studied for the solution-processing of these semiconductors and the studies can be categorized into two; 1) preparing oxide or sulfide precursors and 2) synthesizing colloidal nanoparticles. Both methods have in common that they prepare materials that are soluble in a solvent. Main difference between two methods is that the former is synthesizing a precursor material for the target material and the latter is preparing a target oxide or sulfide semiconductor itself in nano-form.

This thesis covers my studies on developing solution-processing technique for oxide and sulfide semiconductors using both approaches mentioned above and their application to thin film electronics. It begins with a chapter introducing device physics of thin film solar cells and transistors, that is not described in detail in each chapter, but needs for a deep understanding of the following studies.

Following three chapters demonstrate solution-processing of metal oxides and sulfides via the newly developed molecular precursors, followed by their applications to thin film transistors and solar cells. Many studies have been suggested to prepare such oxide films via sol-gel technique using a variety of metal precursors such as metal nitrates, chlorides, or oxychlorides. However, intrinsic toxicity of the materials and complex preparation procedures are the major obstacles to adopt it to thin film deposition process in the electronics industry. Hence, my studies are focusing on reducing toxicity of the precursor solutions and optimizing processing condition for high-quality oxide and sulfide thin films.

In **Chapter 3**, simple and universal synthetic approach, but less toxic preparation of metal oxide precursors is demonstrated. High-κ dielectrics such as HfO_2, ZrO_2, and Ta_2O_5 thin films are prepared using the precursor solutions and their optical, electrical, and chemical properties are characterized.

Finally, the prepared films are applied to TFTs in order to implement low-power electronic devices.

Chapter 4 and **5** is devoted to developing molecular precursors for metal sulfides and applying them to TFTs and thin film solar cells (TFSCs). Again, I focused on developing non-toxic and universal synthetic approach for molecular precursors of metal sulfides. By following nearly identical synthetic scheme, CdS, Cu_2S, In_2S_3, and Ga_2S_3 thin films are prepared and characterized. Owing to superior electron mobility of CdS, high performance CdS thin film transistors are fabricated and characterized (**Chapter 4**). Furthermore, ternary and quaternary metal sulfide thin films are prepared and characterized in **Chapter 5** via simple mixing of the precursor solutions of each sulfide. Decomposition process of thiolate precursors are investigated in detail. Then, thin film solar cells with broadband response from UV to near IR are successfully demonstrated by using solution-processed $CuInS_2$ thin film which exhibits excellent and well-defined light absorption up to 860 nm.

Chapter 6 deals with the application of metal oxide nanoparticles to alter localized surface plasmon resonance by Ag quantum dots (Ag QDs) embedded in the polymer solar cells (PSCs) to boost power conversion efficiency (PCE). ZnO and TiO_2 nanoparticles dispersed in alcohol solvents are solution-processed on Ag QDs coated ITO substrate in order to minimize unintended damages to Ag QDs during thin film deposition process. Optical properties of Ag QDs, which can be altered by surrounded media, are characterized through both experiments and numerical calculations. By using two metal oxides as efficient electron transport layer, PSCs with inverted structures are fabricated. Computer simulation on the device identifies the behavior of incident photons interacting with Ag QDs inside the devices.

Finally, simple and efficient method to enhance colloidal stability of ZnO nanoparticles are demonstrated in **Chapter 7**. High surface to volume ratio of nanoparticles spontaneously induces interparticle attraction resulting in reduced surface energy. Unintended formation of nanoparticle aggregation leads to poor solubility of ZnO nanoparticles in both polar and nonpolar solvents. In order to form high quality ZnO thin film on soft matters like organic materials with least damages, it is critical to improve colloidal stability of ZnO nanoparticles in polar solvents. To do so, a coordination complex, Ti(acac) is introduced as efficient and universal stabilizer. Optical and structural differences of ZnO nanoparticles w/ and w/o the stabilizer are demonstrated. Significantly improved colloidal stability of the nanoparticles are proved using UV-vis absorption spectra and solar cell applications.

The conclusion and outlook of the studies are summarized in the last chapter.

CHAPTER 2. Device Physics of Thin Film Transistors and Solar Cells

This chapter provides theoretical background of device physics on which there is little discussion in each chapter. It covers from operating mechanism of thin film electronics (here, transistors and solar cells) and figures of merit of each thin film device to get a thorough understanding of device application.

2.1 Working principle of thin film transistors

Thin film transistor (TFT) is a switching component in electronic devices, which comprises sequential deposition of metal (source, drain, and gate), insulator (dielectric), and semiconductor (channel) thin films on an insulating substrate. There exist three contacts; source (grounded), drain, and gate in TFT. For n-type channel, electron flows from source to drain and the amount of electron flow is controlled by gate. The position of gate electrode can be the top or bottom of the device; the former is called top-gate TFT and the latter called bottom-gate TFT. Staggered and coplanar structure are possible according to the position of source and drain relative to gate. Semiconducting channel is positioned between gate and source/drain in staggered structure and positioned out of source (or drain) / dielectric / gate stack in coplanar structure. **Figure 2.1** exhibits four possible geometries of TFT.

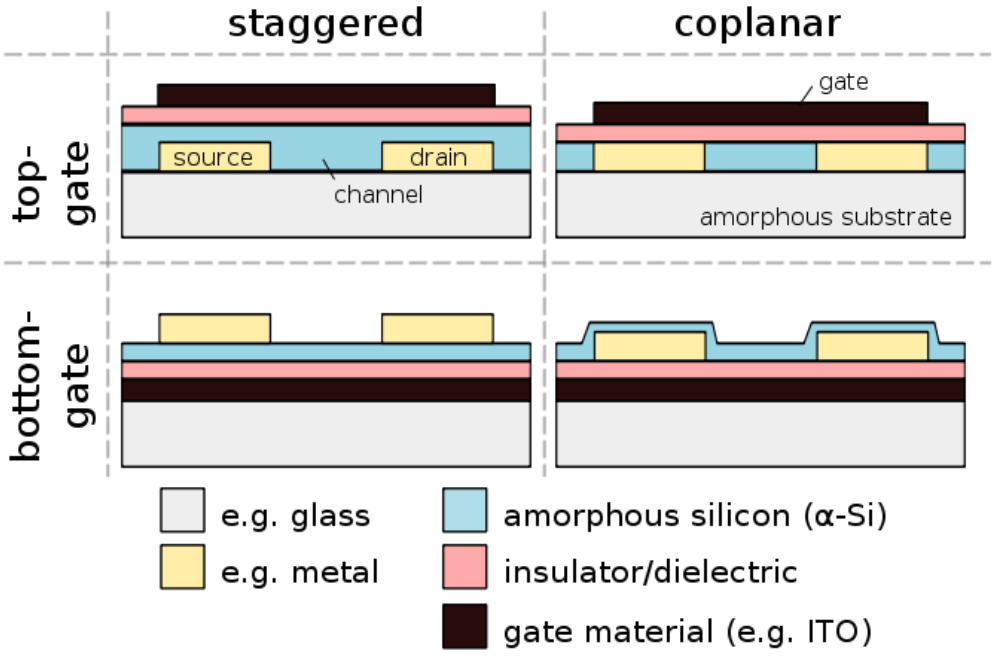

Figure 2. 1. Four common TFT architectures.

Based on the switching mechanism, there are two major operation modes; 1) enhancement and 2) depletion mode. Enhancement mode TFT allows current flow only when a certain amount of gate bias is applied to the device. Therefore, the device should exhibit no current when gate bias is 0 V. While, depletion mode TFT is turned on at zero gate bias. For n-type channel, applying negative gate bias induces charge carrier depletion in the channel, which leads to turn it off. **Figure 2.2** describes schematic energy band diagram under n-type enhancement mode operation.

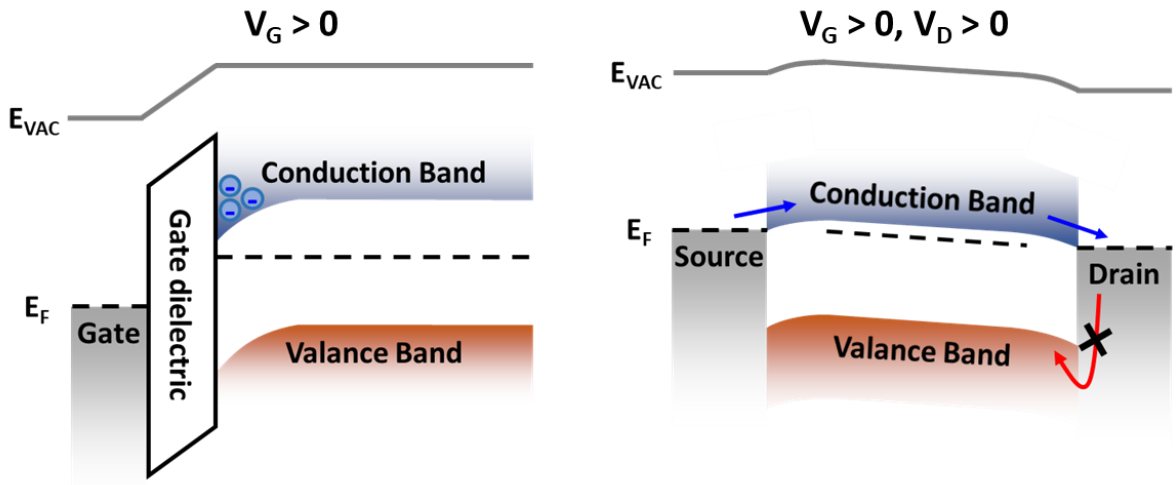

Figure 2. 2. Schematic band diagram of n-type TFTs for operation in enhancement mode.

From now on, it is assumed that all junctions in the device form Ohomic contact and no charge trapping occurs during the operation for simplicity. When gate bias (V_G) > 0, band banding occurs at the semiconductor/dielectric interface. It leads to electrons accumulation at the interface due to fermi level close to conduction band (CB) of the semiconductor. Then charge carriers are ready to flow in the channel (left image in **Figure 2.2**). The flow of accumulated charge carriers (drain current, I_D) is guided by drain voltage (V_D) (right image in **Figure 2.2**).

It is obvious that charge density along the channel is uniform at V_D = 0 V. Applying V_D alters charge density distribution across the channel. For a V_D > 0 in n-type TFT, the induced charge density at a position x is:

$$q_{\mathrm{ind}}(x) = n(x)ed = C_{ox}\left(V_G - V_T - V(x)\right) \tag{2-1}$$

where n is the electron concentration, e is the elemental charge, d is the channel thickness, C_{ox} is capacitance density of dielectric, and $V(x)$ is the effective voltage at x. Because our interest is mobile charges, fixed charges in the depletion region was neglected in the Eq. (2-1). When drain voltage is large enough ($V_D \approx V_G - V_T$, the saturation condition) for electron concentration to be 0 near drain ($n(L)$ = 0), we say that the channel is *pinched off*. Further increase in V_D leads I_D to be saturated approximately

to the value at pinch-off. Carrier concentrations in the device under various bias conditions are shown in **Figure 2.3**.

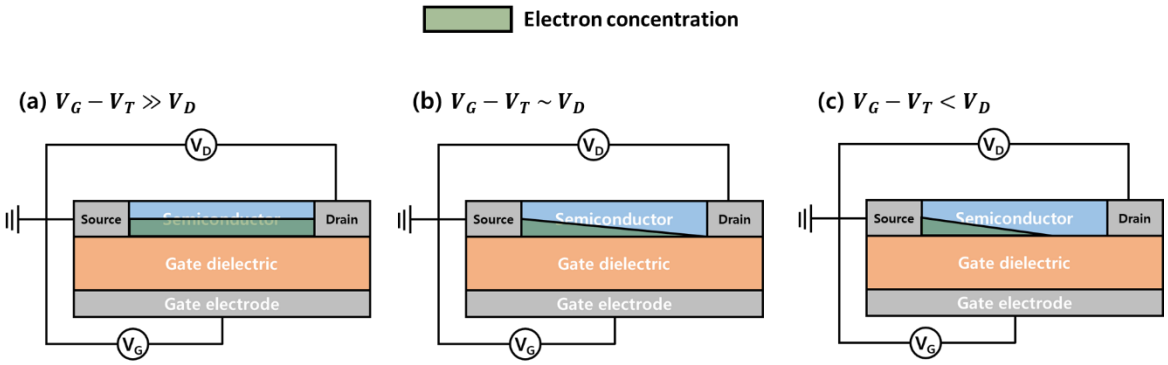

Figure 2. 3. Schematic illustration of carrier concentration along the channel.

V_T is the threshold voltage, which is the least amount of voltage to induce charge carriers in the channel. It is affected by the amount of deep level traps, nonideal metal-semiconductor junctions in the devices. The latter forces to use energy for band-bending from charge depletion to accumulation for enhancement mode operation. The case becomes opposite when the device works in depletion mode (band-bending from charge accumulation to depletion).

2.2 Figures of merit of thin film transistors

TFT devices are commonly characterized in two types of current – voltage (I–V) characteristics; I_D–V_D under constant V_G, called output curve and I_D–V_G under constant V_D, called transfer curve. Typical output and transfer curves of n-type TFT are shown in **Figure 2.4**.

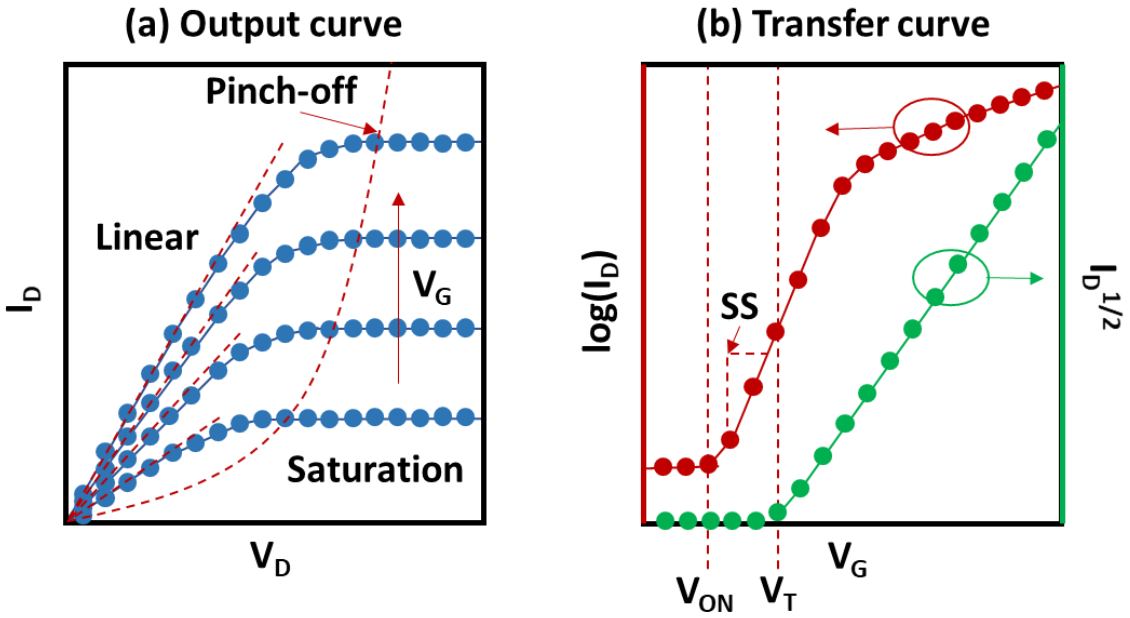

Figure 2. 4. I-V characteristics of n-type TFT. (a) I_D–V_D curve or output curve and (b) I_D–V_G or transfer curve.

Output curve exhibits two distinct regions, where linear I_D–V_D response is shown in low V_D and I_D starts to be saturated after the channel is *pinched off*. Increasing V_G accumulates more charges in the channel resulting in I_D increase. Transfer curve includes important figures of merit for TFT such as V_T, subthreshold swing (SS), I_{ON}/I_{OFF} ratio, and carrier mobility (μ, or called field-effect mobility, differ from bulk mobility). SS (decades/mV in unit) represents how fast the device switches ON and OFF. I_{ON}/I_{OFF} shows how much the difference between ON state current and OFF state current is. High I_{ON}/I_{OFF} ratio is achieved in high-performance low-leakage device.

These I–V relations can be derived quantitively by using Ohm's law:

$$V_D = I_D R = I_D \left(\frac{L}{\sigma W d}\right) \tag{2-2}$$

where R is the resistance of the channel, σ is the conductivity, and L and W is the length and width of the channel, respectively.

Thus, I_D can be written as

$$I_{\mathrm{D}} = \frac{W}{L}\sigma dV_{\mathrm{D}} = \frac{W}{L}(ne\mu)dV_{\mathrm{D}} = \frac{W}{L}ned\mu V_{\mathrm{D}} \tag{2-3}$$

where μ is the carrier mobility in the channel, not bulk mobility. The definition of the conductivity was used for the second equality. It is noteworthy that Eq. (2-3) is only valid when V_{D} is constant along the channel, which is not the case here. When V_{D} is applied across the channel, two position (x)-dependent variables, $n(x)$ and $V(x)$ should be taken into account. At position x in the channel, we can generalize Eq. (2-3) as

$$I_{\mathrm{D}}dx = W(n(x)ed)\mu dV(x) = \mathrm{W}C_{ox}\big(V_{\mathrm{G}} - V_{\mathrm{T}} - V(x)\big)\mu dV(x) \tag{2-4}$$

Second equality is acquired by substituting Eq. (2-1) for *n(x)ed*. Integrating from source to drain,

$$\int_0^L I_{\mathrm{D}}dx = WC_{ox}\mu\int_0^{V_{\mathrm{D}}}\big(V_{\mathrm{G}} - V_{\mathrm{T}} - V(x)\big)dV(x)$$

$$I_{\mathrm{D}} = \frac{W}{L}C_{ox}\mu\left[(V_{\mathrm{G}} - V_{\mathrm{T}})V_{\mathrm{D}} - \frac{V_{\mathrm{D}}^2}{2}\right] \tag{2-5}$$

Eq. (2-5) is the key equation describing the relation between I_{D} and V_{G} & V_{D} in TFT.

The charge carrier mobility (cm^2/V s) is the quantity that how fast charge carriers can move (cm/s) under an electric field (V/cm) along the channel. It can be calculated in both linear and saturation region. For the purpose of calculating the linear mobility, μ_{lin}, (where $V_{\mathrm{G}} - V_{\mathrm{T}} \gg V_{\mathrm{D}}$), it is convenient to define two quantities, called the transconductance (g_{m}) and conductance (g_{d}).

$$g_d = \frac{\partial I_{\mathrm{D}}}{\partial V_{\mathrm{D}}}\Big|_{V_{\mathrm{G}}} = \frac{W}{L}C_{ox}\mu_{lin}(V_{\mathrm{G}} - V_{\mathrm{T}})$$

$$g_m = \frac{\partial I_{\mathrm{D}}}{\partial V_{\mathrm{G}}}\Big|_{V_{\mathrm{D}}} = \frac{W}{L}C_{ox}\mu_{lin}V_{\mathrm{D}} \tag{2-6}$$

As the transconductance and conductance are constant, voltage and current exhibit linear dependence each other. Differentiating Eq. (2-6) with respect to V_{G} and V_{D}, respectively, we obtain

$$\frac{dg_d}{dV_{\mathrm{G}}} = \frac{dg_m}{dV_{\mathrm{D}}} = \frac{W}{L}C_{ox}\mu_{lin} \tag{2-7}$$

According to Eq. (2-7), the linear mobility represents how fast the slope of the linear region is

changed under the change of V_G or V_D. In practice, the conductance, rather than transconductance, is often used to calculate the linear mobility owing to well-defined linear region in output curve.

The saturation mobility, μ_{sat}, can be calculated from Eq (2-5) with the saturation condition, $V_D = V_G - V_S$.

$$I_{D,sat} = \frac{W}{2L} C_{ox} \mu_{sat} (V_G - V_T)^2 \tag{2-8}$$

μ_{sat} can be easily found by finding the slope of a tangent line in $I^{1/2}$ vs. V_G plot shown in **Figure 2.4**. x-intercept of the line corresponds to V_T. The transconductance in the saturation region can be acquired by differentiating Eq. (2-8) with respect to V_G,

$$g_{m,sat} = \frac{\partial I_{D,sat}}{\partial V_G} = \frac{W}{L} C_{ox} \mu_{sat} (V_G - V_T) \tag{2-9}$$

Now, we revisit subthreshold swing, *SS*. The value of SS can be easily obtained by finding how much voltage is required to increase I_D by an order in the subthreshold region of the transfer curve. Subthreshold region is typically assigned to the region where the device is being operated below V_T.

Apparently, low *SS* is preferred for TFT proving its fast ON and OFF switching ability. High *SS* can be attributed to the presence of traps at the dielectric/semiconductor interface. The subthreshold swing is generally expressed as

$$SS = \ln(10) \frac{kT}{q} \left(\frac{C_{ox} + C_D}{C_{ox}} \right) \tag{2-10}$$

where C_D is the capacitance of the depletion layer. For ideal case, $C_{ox} \rightarrow \infty$, the minimum possible value of *SS* is ~ 60 mV/dec.

2.3 Working principle of thin film solar cells

Solar cells are energy-harvesting devices that directly convert photons, which is mainly from sun, to electrons. When the device is exposed to solar irradiation (or other light sources), electrons in ground state are excited to higher energy states. The excited electrons supply potential difference (voltage) in a material and the phenomenon is called the photovoltaic effect. Subsequently, the device extracts electrons out of the device generating photocurrent. Because each thin film solar cell exhibits its own unique device operation, I am focusing on organic solar cell (OSC) that is one of the most promising thin film solar cells and most frequently used as device applications in the following chapters. Schematic device architectures of OSCs are shown in **Figure 2.5.**

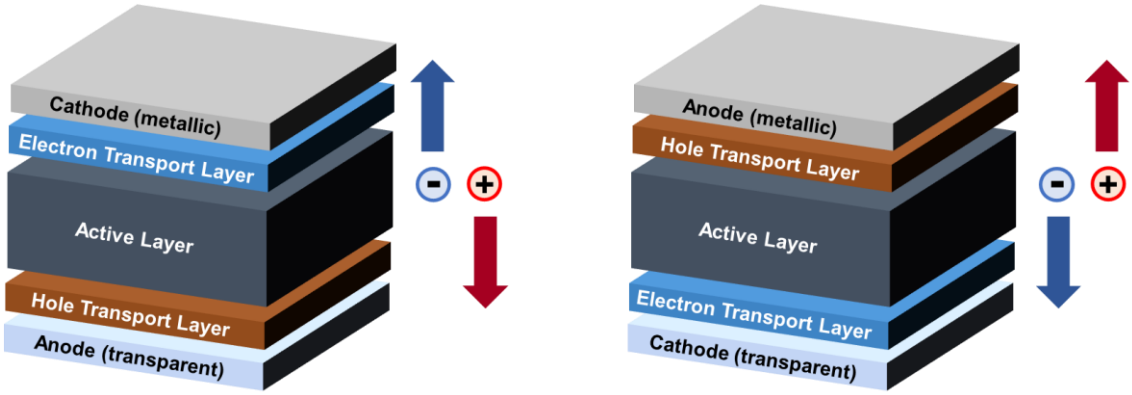

Figure 2. 5. Two possible devices structures of OSCs. The structure shown in the left of the figure is called conventional structure and the structure in the right is called inverted structure. It depends on the direction of the charge flow in the device.

OSC operation can be summarized as

1. Light absorption and exciton generation.
2. Exciton diffusion
3. Exciton dissociation and charge transfer
4. carrier transport to the electrodes.
5. Charge carrier (electron and hole) collection by the electrodes.

OSC uses very thin active layer ~ 100 nm for light absorption. Although absorption coefficient of organic materials used in active layer exhibit > 10^5 cm^{-1},[20] 100 nm is not enough to fully absorb incident light especially in wavelengths near absorption onset. Intuitively, increasing the thickness can be an effective approach to enhance light absorption. But the limitation to the thickness exists in organic materials due to the low charge carrier lifetime that causes recombination of the carriers before reaching to the electrode. Alternate method to increase light absorption with limited thickness

is confining high intensity electric field to the active layer. OSC utilizes incoming light and light coming back to the front by back reflective electrode. Because the device comprises a series of thin films, which have different refractive indices, *n*, electric fields are localized in each layer by constructive or destructive interference of two plane waves (transmitted and reflected light at each interface). **Figure 2.6** represents localized electric field in the active layer with various wavelengths in the device.

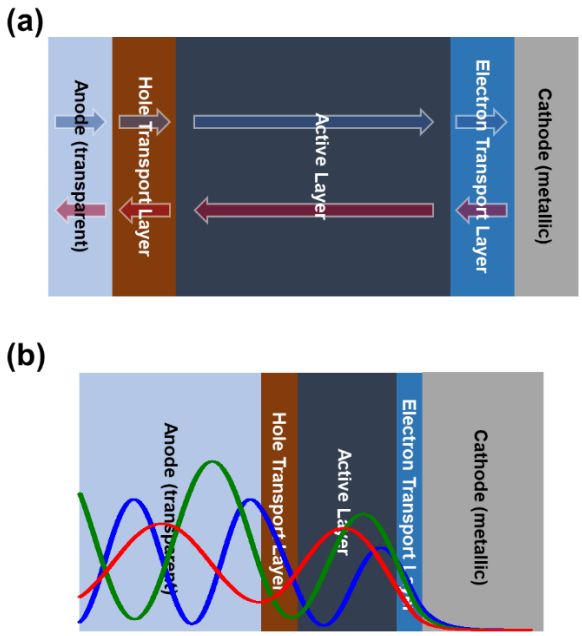

Figure 2. 6. Electric field distribution inside the device. (a) Schematic illustration of transmitted (blue arrows) and reflected waves (red arrows) at each interface and (b) real field distribution *E(x)* in the device. Blue, green, and red lines correspond to 400, 500, and 600 nm wavelengths, respectively.

Electric field intensity in the active layer can be maximized by careful selection of buffer layers with the desired thickness. The intensity of wavy electric field starts to decrease in the active layer due to its high extinction coefficient, *k*. The information of spatial distribution of electric field intensity, $|E(x)|$ can be used to calculate time averaged energy dissipation rate of the field, $Q_\lambda(x)$ at a wavelength, λ as a function of *x*:

$$Q_\lambda(x) = \frac{1}{2} c\epsilon_0 \alpha(\lambda) n(\lambda) |E_\lambda(x)|^2 \tag{2-11}$$

where *c* is the speed of light, ϵ_0 is vacuum permittivity, and α is absorption coefficient. Absorption coefficient can be easily obtained by using a simple relation with *k*:

$$\alpha(\lambda) = \frac{4\pi k}{\lambda} \tag{2-12}$$

Dividing Eq. (2-11) by the energy, photoexcited electron generation rate at a wavelength as a function of x can be obtained:

$$G_\lambda(x) = \frac{Q_\lambda(x)\lambda}{hc} \tag{2-13}$$

where h is Plank constant. Integrating Eq. (2-13) by x across the active layer give us the generation rate inside the active layer as a function of λ.

Photoexcited electrons from the highest occupied molecular orbital (HOMO) to the lowest unoccupied molecular orbital (LUMO) are electrically bound by positively charged electron hole. As the bound electrons exhibit distinct behavior from conduction electrons or free electrons, the electron-hole pair with lattice distortion is considered as a quasiparticle, called exciton. Its size is affected how strongly excitons are coupled with surrounding lattice distortion. The size of the exciton is defined to the exciton Bohr radius.

Inorganic semiconductors generally exhibit high dielectric constants. In order words, the electric field can easily distort or polarize the lattice of the materials. Consequently, the screening of the electric field between electrons and holes results in photo-induced excitons exhibiting low exciton binding energy, on the order of 10 meV. The excitons are called Wannier-Mott excitons or Wannier excitons, in short. Unlike inorganic semiconductor, organic based semiconductors exhibit low dielectric constants. Because of weak screening of the electric field by organic materials, the excitons have high binding energy on the order of 1 eV. This type of the exciton is called Frenkel exciton. **Figure 2.7** compares Frenkel and Wannier excitons.

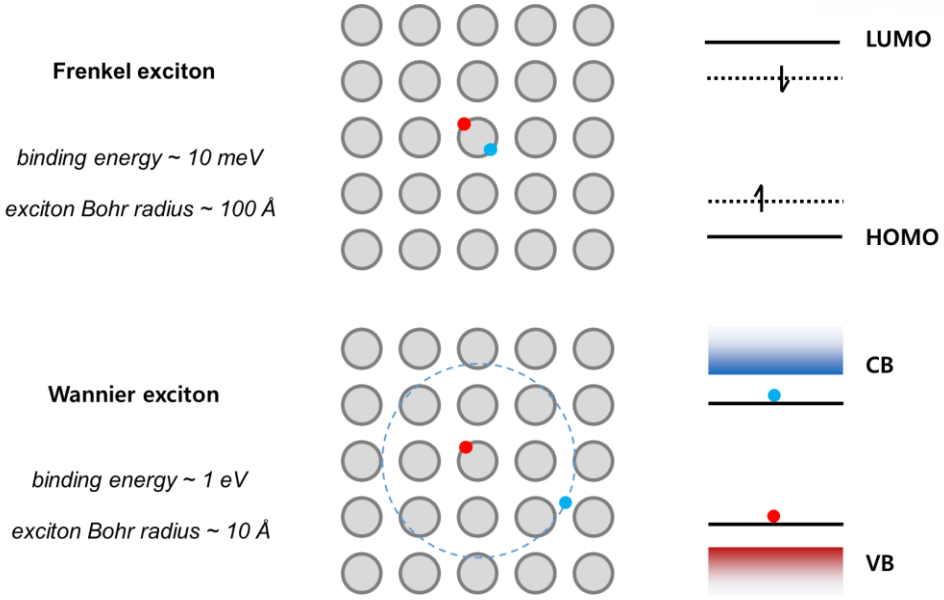

Figure 2. 7. Schematic pictures of Frenkel and Wannier excitons.

As mentioned above, Frenkel exciton requires a few eV to dissociation strongly bound excitons. In organic solar cell, the energy is supplied by the HOMO and LUMO offset between electron donor and acceptor, which electron donor have orbitals at higher energy than acceptor for the spontaneous electron transfer from donor to acceptor. For polymer-fullerene based active layer, the required energy offset is known to be ~ 0.3 eV. Recently, a few papers have reported that the energy offset less than 0.3 eV or even no energy offset is required to accomplish efficient exciton dissociation in polymer-nonfullerene system.[21-23] In traditional bilayer structure, where electron donor and acceptors are stacked in series, exciton diffusion to the electron donor/acceptor interfaces is required for exciton dissociation. However, the excitons are electrical neutral, which is not affected by internal electric field, and their diffusion length, L is limited to ~ 50 Å because of short lifetime of the excitons in organic materials. L can be obtained using the relation:

$$L = \sqrt{D\tau} \tag{2-13}$$

where D is the exciton diffusivity and τ is exciton lifetime. Hence, exciton diffusion efficiency, μ_{ED} is a limiting factor for photocurrent generation of OSCs. Bulk heterojunction is an excellent solution to solve this problem. The idea is that the bulk mixture of donor and acceptor have significantly enlarged interfacial area between two materials compared to bilayer structure. Ideal morphology of bulk heterojunction leads μ_{ED} to be ~ 100%. The difference between bilayer structure and bulk heterojunction is shown in **Figure 2.8.**

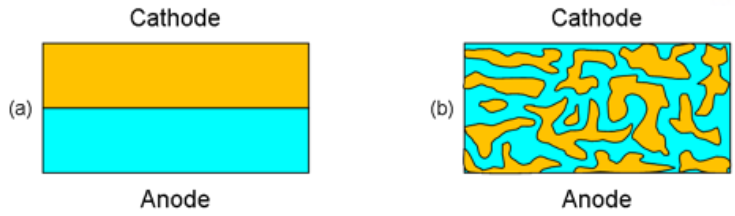

Figure 2. 8. Schematic illustration of (a) bilayer and (b) bulk heterojunction of the active layer. Cyan and yellow colors represent donors and acceptors, respectively.

At short-circuit condition (V = 0), work function difference between two electrodes induces built-in field in the device and the field drives the flow of charge carrier to the desired electrode. Carrier transport in organic materials is described by quantum mechanical electron hopping. Because of the strong localization of the electrons in organic semiconductors, the electrons have to be hopped from one to the other to overcome the local potential. This process is quite inefficient compared to the case of inorganic materials and results in significantly low charge carrier mobility.

Finally, the charge carriers are collected by the electrodes. The charge carriers escaped from the active layers are selectively transported to the electrode by buffer layers: hole and electron transport layer. Charge collection efficiency, μ_{CC} is determined by interfacial trap density at the buffer layer/electrode interface and the quality of junction. Large work function difference between two layers will form Schottky barrier, which hinders efficient charge collection to the electrode and causes recombination loss.

2.4 Figures of merit of thin film solar cells

The vast amount of solar energy ~ 4×10^{20} J is poured on earth in every second and solar cell directly convert irradiated photons to electrons. When the sunlight passes through the atmosphere, a part of solar spectrum is absorbed by water vapor and ozone and even scattered by dusts and aerosols in air. The attenuated solar spectrum by the atmosphere is defined to airmass (AM). The airmass is numbered by considering the zenith angle of light incidence on the ground. e.g. light incident at 45° above the ground corresponds to 1.5, which is the value of sec45°. For universal characterization of the solar cells fabricated anywhere in the world, the standard airmass, AM1.5G, is widely applied to the solar simulator. Total power density of AM 1.5G solar spectrum is ~1000 W/m^2. Left image of **Figure 2.9** compares the irradiance of AM 1.5G with AM 0 corresponding to solar spectrum outside the earth atmosphere. Huge attenuation at ~750 nm in the AM 1.5G spectrum is due to O_2 absorption and several holes after 900 nm are mainly attributed to the absorption by H_2O molecules. The photon flux density of AM 1.5G can be calculated by dividing solar irradiance by the photon energy at each wavelength. The photon flux density is shown in the right image of **Figure 2.9**.

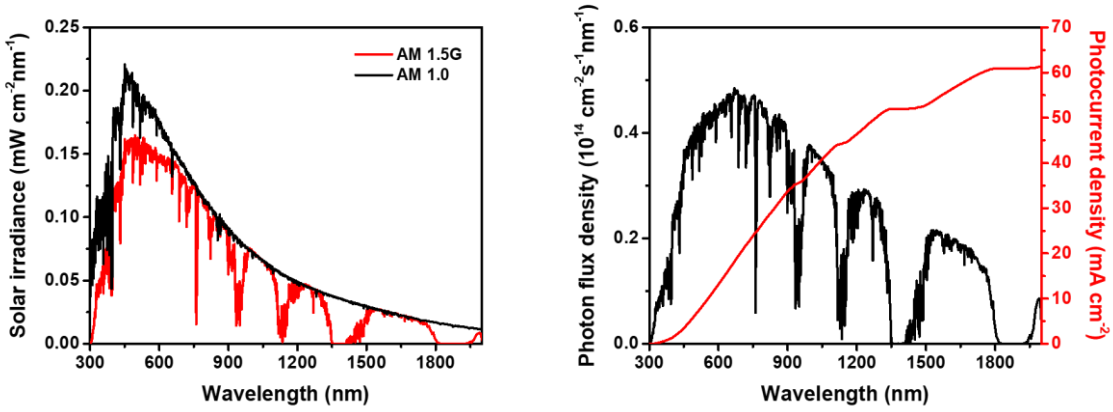

Figure 2. 9. Solar irradiance of AM1.5G and AM 1.0. Photon flux density of AM 1.5G and maximum photocurrent density of the device absorbing light up to corresponding wavelength are shown in the right of the figure.

Optical bandgap, E_g of the active layer determines the absorption range of incident light to the solar cell. The longest wavelength the active layer can deal with can be calculated by using simple relation between photon energy and wavelength.

$$\lambda_{max} = \frac{hc}{E_g} \tag{2-14}$$

Then we can calculate the maximum photocurrent density of the ideal solar cell that absorbs all the photons with the wavelengths in E_g:

$$J_{ph} = q\int_0^{\lambda_{max}} \frac{d\phi}{d\lambda} d\lambda \tag{2-15}$$

where $d\phi/d\lambda$ is the photon flux density. The calculated photocurrent density is shown as red curve in the right image of **Figure 2.9**.

J–V characteristics of the solar cell can be expressed using the modified diode equation:

$$J = J_s\left[\exp\left(\frac{q(V-JR_sA)}{nkT}\right) - 1\right] + \frac{V-JR_sA}{R_{sh}A} - J_{ph} \tag{2-16}$$

where J_s is the saturation current of the diode, n is the ideality factor, k is the Boltzmann constant, A is the device area, R_s is series resistance, and R_{sh} is shunt resistance. Its equivalent electric circuit is shown in **Figure 2.10**. Two resistors in the circuit causes parasitic loss during the operation of the device.

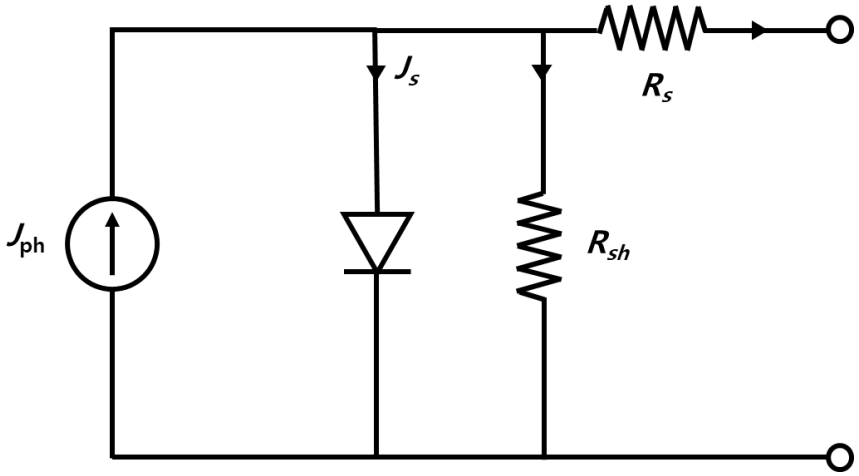

Figure 2. 10. Equivalent circuit of a solar cell

An ideal solar cell has n close to 1, 0 of R_s, and infinite R_{sh}. These conditions reduce Eq. (2-16) to be:

$$J = J_s\left[\exp\left(\frac{qV}{kT}\right) - 1\right] - J_{ph} \tag{2-17}$$

which is a typical diode equation with an additional term, $-J_{ph}$. Ideal J_s exhibits exponential dependence on E_g: $J_s \sim \exp(-E_g)$. Short-circuit current density, J_{SC} ($V = 0$) is equal to J_{ph} in the ideal case and open circuit voltage, V_{OC} is obtained by putting $J = 0$ to Eq. (2-17).

$$V_{OC} = \frac{kT}{q}\ln\left(\frac{J_{ph}}{J_s} + 1\right) \tag{2-18}$$

Output power density of the device can be calculated by multiplying V to Eq. (2-17).

$$P_{\text{out}} = JV = J_s V\left[\exp\left(\frac{qV}{kT}\right) - 1\right] - J_{ph}V \tag{2-19}$$

Maximum output power density, P_m is achieved when $dP_{out}/dV = 0$:

$$\frac{dP_{\text{out}}}{dV} = \frac{d(JV)}{dV} = \frac{dJ}{dV}V + J = 0 \tag{2-20}$$

Substituting Eq. (2-17) for J of dJ/dV in Eq. (2-20) gives the current density at maximum power point (mpp), J_m:

$$J_m = -J_s\beta V_m \exp(\beta V_m) \tag{2-21}$$

where β is kT/q. The voltage at mpp, V_m can be obtained by substituting Eq. (2-21) for J in Eq. (2-17):

$$-J_S\beta V_m \exp(\beta V_m) = J_s\left[\exp\left(\frac{qV_m}{kT}\right) - 1\right] - J_{ph}$$

$$V_m = \frac{1}{\beta}\ln\left[\frac{(J_{ph}/J_s)+1}{1+\beta V_m}\right] = V_{\text{OC}} - \frac{1}{\beta}\ln(1+\beta V_m) \tag{2-22}$$

The power conversion efficiency (PCE) is the ratio of P_m to the incident power density, P_{in}.

$$\eta = \frac{|P_m|}{P_{in}} = \frac{|I_m V_m|}{P_{in}} = \frac{J_s\beta V_m^2 \exp(\beta V_m)}{P_{in}} \tag{2-23}$$

(-) sign of P_m from J_m was removed in Eq. (2-23) because the sign indicates the power is generated from the device. Positive sign of P_{in} in denominator means that the power is absorbed by the device. For the efficiency calculation, the sign of each power is physically meaningless.

J-V characteristics of solar cell under illumination is shown in **Figure 2.11**.

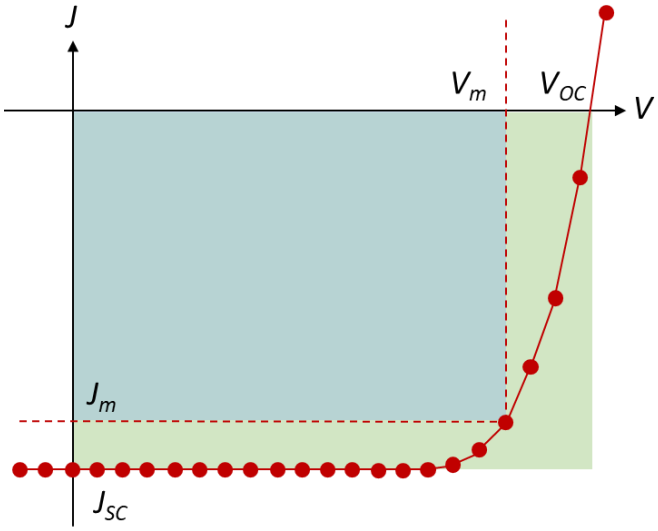

Figure 2. 11. *J-V* characteristics of solar cell under illumination.

Here, a new figure of merit, fill factor, *FF* is introduced. *FF* is a geometrical parameter measuring the degree of areal occupation of blue square ($V_m \times I_m$) in green square ($V_{OC} \times J_{SC}$). It cannot reach to 100% even in ideal solar cell because of the exponential dependence of *J-V* characteristics. PCE, then can be expressed using V_{OC}, J_{SC}, and *FF*:

$$\eta = \frac{|P_m|}{P_{in}} = \frac{|V_m I_m|}{P_{in}} = \frac{V_{OC} J_{SC} FF}{P_{in}} \tag{2-24}$$

Eq. (2-24) addresses the consideration on theoretical maximum efficiency of solar cell. V_{OC} decreases with smaller E_g because of increased J_s, but J_{SC} increases as we discussed in **Figure 2.9** and Eq. (2-14, 15). Because of this trade-off, it is reported that theoretical maximum efficiency of 30.6% can be achieved at 1.32 eV of E_g. The values can exhibit some discrepancy depending on the studies. The theoretical efficiency limit is called Schokley-Queisser limit.

In nonideal solar cell, *FF* is hugely affected by two parasitic resistances, R_s and R_{sh}:

$$FF(R_s, R_{sh}) = FF(0, \infty)\left[\left(1 - \frac{J_{SC} R_s}{V_{OC}}\right) - \left(\frac{V_{OC}}{J_{SC} R_{sh}}\right)\right] \tag{2-25}$$

Another useful figure of merit for solar cell characterization is quantum efficiency. The simplest quantum efficiency of solar cell is photon to electron conversion efficiency. It is called the external quantum efficiency (EQE) or incident photon to electron conversion efficiency (IPCE). An example of EQE spectrum is shown in **Figure 2.12**.

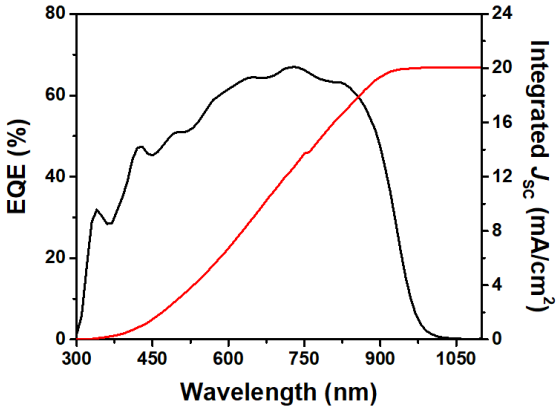

Figure 2. 12. An example of external quantum efficiency and integrated J_{SC} of solar cell.

J_{SC} of the device can be estimated from EQE spectrum using the following equation:

$$J_{SC} = \frac{e\lambda}{hc} \int EQE(\lambda) F(\lambda) d\lambda \tag{2-26}$$

where $F(\lambda)$ is solar irradiance. As J_{SC} measured in *J-V* characteristics is significantly altered by the small deviation of the distance between light source (solar simulator) and the device, EQE is useful to cross-check the measured J_{SC}. It should be noticed, however, that the estimated J_{SC} from EQE is only valid when the device exhibits linear dependence of J_{SC} on light intensity.

Internal quantum efficiency, IQE is the ratio of the number of absorbed photons by active layer to the number of incident photons. Because IQE excludes photons absorbed by the other layers in solar cell, it can be useful when you want to demonstrate the quality of the device; how efficiently photoexcited electrons are extracted out of the device. Despite its usefulness, however, the practical difficulty of measuring light absorption by active layer makes researchers hard to estimate the exact IQE of the device.[24]

CHAPTER 3. Implementation of Low-Power Electronic Devices Using Solution-Processed Tantalum Pentoxide Dielectric

The content of this chapter is published in *Advanced Functional Materials* **28**, 1704215 (2018)

3.1 Research background

Over the past few decades, field effect transistors (FETs) have been utilized as an essential component in electronic devices due to their high input impedance, low power consumption, and the reduced complexity of fabrication compared to bipolar junction transistors.[25] Although most FET research has focused on the transport layer to improve device performance and versatility,[26-28] dielectric materials have also led to significantly improved performance. Among various dielectric materials, silicon nitride and silicon oxide layers have been widely adopted as insulating dielectric layers in FET devices fabricated on Si wafers owing to their superior electrical insulating properties and ease of growth on the wafer.[29-30] However, in order to reach a desirable drain current in FETs using silicon oxide or nitride dielectrics, which have low dielectric constants (κ), high gate voltages (typically on the order of 40–100 V in cases of the devices with the channel formed via solution-processing) must be applied, resulting in significant power consumption.

These high voltage requirements conflict with output data signals for standard digital display formats (such as digital visual interface (DVI) and high definition multimedia interface (HDMI)) as well as outputs for graphic-processing units and most integrated circuits, which all generally produce output signals with voltages less than 5 V. Thus, in order for existing solution-processed FET technologies to integrate with existing display drivers or other logic elements, a substantial signal amplification stage is necessary. Or, if such solution-processed FETs are to operate independently, stable power supplies at potentials of ≈100 V are necessary. Although the low cost and flexibility of solution-processed FETs makes them very attractive for application in low-cost, disposable and hand-held devices, their power supply requirements currently make them totally impractical for these purposes.

One simple approach to reduce the gate voltage requirements is to make the dielectric layer thinner. Decreasing the dielectric thickness, however, causes serious problems as it may drastically increase charge carrier leakage into the transport layer via quantum tunneling effects[31-32] and change the dielectric and electronic behavior of SiO_2 layers as they become very thin.[31-33] Consequently, the incorporation of high-κ dielectrics is inevitable in order to achieve both high capacitance density and low leakage current in FET devices. Recent results have demonstrated the possibility that HfO_2[34-35] and

ZrO_2[36-37] can be utilized as dielectric layers with high-κ values in FETs. Tantalum, like it's neighboring elements Hf and Zr, forms oxides with high-κ values[38] and is used extensively in capacitor devices, however, has not been explored as extensively in FETs. Although conventional methods for metal oxides, such as metal organic chemical vapor deposition,[39] atomic layer deposition,[40] and sputtering,[41] guarantee high crystallinity and good electrical properties, they are cost- and time-inefficient and may only be applied to limited-area targets. Furthermore, high vacuums of less than 10^{-7} Torr or high temperatures over 500 °C are necessary to grow films with reasonable thickness via these techniques. Therefore, it is of great interest to develop efficient and low-cost processing methods for high-κ dielectric layers exhibiting comparable performance to conventional methods.

One probable candidate for simple and low-cost processing of the inorganic layer is solution-processing. The potential of solution-processing in electronic devices has been vindicated via high efficiency solar cells[42] and light emitting devices[43] prepared by solution-processing which show comparable performance with devices fabricated via conventional processes. Several research teams have reported solution-processed high-κ dielectric layers to replace conventional deposition processes.[44-47] However, most approaches require complex synthetic schemes, the addition of a variety of extraneous chemicals,[45] photocuring,[44] high temperature annealing,[47] and additional low-κ layer deposition[46]to exhibit high performance electronic devices.

Here, we demonstrate a simple and environmentally friendly processing strategy to fabricate amorphous Ta_2O_5 dielectric layers via solution-processing followed by mild thermal annealing at 200 °C. We also confirm that this synthetic scheme is applicable for HfO_2 and ZrO_2 dielectric layer formation as well. Without additional treatment, the prepared dielectric layers show κ values of 13.9, 22.4, and 26.9 for HfO_2, ZrO_2, and Ta_2O_5, respectively. We investigated the versatility of the fabricated dielectric layers by applying them in FET devices using a variety of transport materials including inorganic CdS (n-type), organic poly(3-hexylthiophene) (P3HT; p-type), and phenyl-C_{61}-butyric acid methyl ester (PCBM; n-type) channel FETs. Among four types of dielectric layers, including SiO_2 as a reference dielectric, Ta_2O_5 based FETs showed the highest carrier mobility in all types of FETs. In particular, inorganic CdS channel FETs deposited on Ta_2O_5 dielectric films showed carrier mobilities of 2.97 $cm^2 V^{-1} s^{-1}$, which is 83% higher than the mobility of the device fabricated on SiO_2 gate dielectric (1.62 $cm^2 V^{-1} s^{-1}$), as well as dramatically reduced threshold voltage (V_{th}) 1.00 V, which are promising results for low-power electronic devices. (18.4 V of V_{th} in SiO_2 based CdS FET.) To the best of our knowledge, this is the first demonstration of high mobility FETs using a low-temperature, solution-processed Ta_2O_5 gate dielectric with significant reduction in operating voltage.

3.2 Experimental details

Preparation of Precursor Solution and Film Formation

Hafnium (IV) isopropoxide isopropanol adduct or zirconium (IV) isopropoxide isopropanol complex or tantalum (V) ethoxide were dissolved in 2-methoxyethanol to make HfO_2, ZrO_2, Ta_2O_5 precursor solutions, respectively. Concentrations were varied from 50 to 200 mg mL^{-1} to achieve the desired thickness of the dielectric film. The solutions were placed on a hot plate at 80 °C for 30 min. Zirconium isopropoxide solutions with concentrations greater than 100 mg mL^{-1} were saturated in 2-methoxyethanol and some undissolved powders settled to the bottom. Prior to film coating, the solutions were filtered through 0.2 μm PTFE syringe filters into precleaned glass vials. 40 μL of the precursor solutions were dispensed onto spinning substrates at 3000 rpm. These processes were performed in an N_2 environment. Finally, the samples were carried out of the N_2 glovebox and annealed at 200 °C in ambient air.

Fabrication of Capacitors

Prepatterned ITO coated glass substrates were sequentially cleaned in an ultrasonicator using detergent, deionized water, acetone, and isopropyl alcohol. The substrates were dried in a vacuum oven at 100 °C overnight. Cleaned ITO substrates were further cleaned by UV-ozone treatment to remove carbon residue and reduce the hydrophobicity of the substrates. Dielectric thin films were coated using the method described above. This process was repeated until the desired film thickness was achieved (3–4 times). The last annealing step was carried out for 1 h for the complete removal of organic residues.

Fabrication of FETs

The device configuration of FETs was BG-TC structure using heavily doped Si substrates as gate and Ag (top electrodes) as drain and source contacts. The substrates of Si and Si/SiO_2 (200 nm, thermally grown) were sequentially cleaned in an ultrasonicator using acetone and isopropyl alcohol, then dried in an oven at 100 °C overnight. High-κ dielectrics layers (HfO_2, ZrO_2, and Ta_2O_5) were coated in the same manner as the capacitors. The CdS layer used in this work was formed by the following procedures; cadmium tert-nonanethiolate (CdTNT) which was synthesized from cadmium acetate and tert-nonanethiol,[28] was dissolved in chloroform (CF) with concentration of 7 mg mL^{-1} in an N_2 filled glovebox. After fully dissolved, the solution was filtered through a 0.45 μm PTFE syringe filter into a precleaned vial. The solution was spin-coated on each substrate, then the substrates were annealed at 300 °C for 30 min. P3HT was dissolved in chlorobenzene with a concentration of 8 mg mL^{-1} and PCBM was dissolved in CF with concentration of 12 mg mL^{-1}. Then the solutions were spin-coated on each substrate. After coating the transport layers, the substrates were brought into a high vacuum chamber ($<10^{-6}$ Torr) and Ag (50 nm) was deposited by thermal evaporation process with shadow masks.

Channel lengths and widths were 50 and 3950 μm, respectively. Electrical characterization was performed using a Keithley semiconductor parametric analyzer (Keithley 4200-SCS). All measurement procedures were carried out in the N_2 filled glovebox.

Material Characterization: AFM height and phase images were obtained using a Veeco Multimode AFM microscope in a tapping mode. XRD patterns were collected using high power XRD instrument a D/MAX2500V/PC (40 kV, 100 mA, Cu anode) with a graphite monochromator and a scintillation counter. The instrument was operated from 20° to 80° with a step size of 0.02° (2θ). XPS measurements were conducted using a ESCALAB 250XI from Thermo Fisher Scientific. Al Ka was used as X-ray source with 900 μm spot size and all spectra were averaged over 5 scans. Scanned regions for each element were chosen from the instrument's database. UV−vis spectrometry was performed using a Varian Carry 5000 spectrophotometer in the range 180–600 nm with 1 nm resolution. To prevent parasitic absorption of UV light by glass, quartz substrates were used for UV–vis absorption measurements. HREELS was conducted using a JEM-2100F instrument. Direct bandgaps were deduced by fitting the data with the equation $y = A + B * (E - E_g)^{1/2}$. Except for UV–vis absorption measurements, all of the characterizations were performed using samples with same structure used in the FET and capacitor devices.

3.3 Results and discussion

Figure 3.1 summarizes the formation process of the dielectric layer via solution-processing.

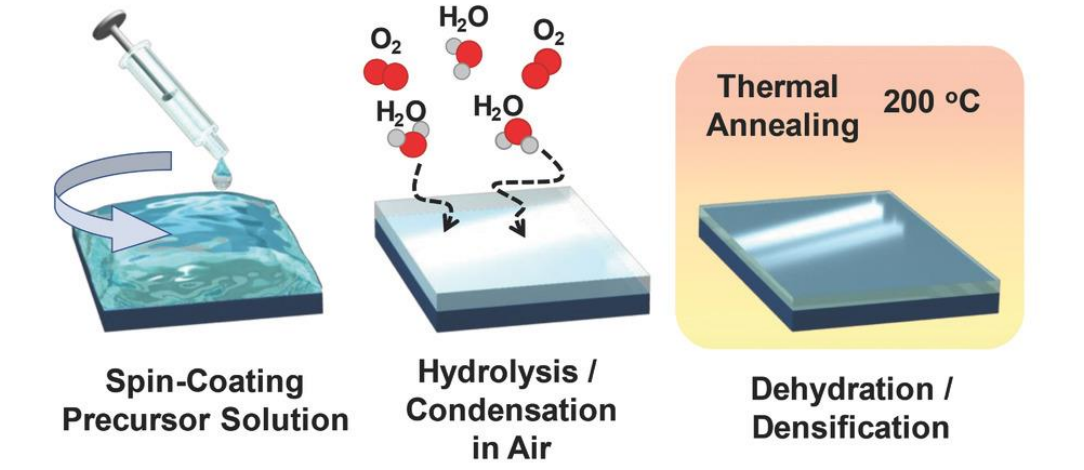

1. Precursor solution – "**Ligand exchange**" *inert*

$$Ta(OEt)_5 + 5HOCH_2CH_2OCH_3 \rightarrow Ta(OCH_2CH_2OCH_3)_5 + 5EtOH$$
$$(Hf, Zr)(OiPr)_4 + 4HOCH_2CH_2OCH_3 \rightarrow (Hf, Zr)(OCH_2CH_2OCH_3)_4 + 4iPrOH$$

2. Thin film– "**Hydrolysis**" *ambient*

$$M(OCH_2CH_2OCH_3)_n + nH_2O \rightarrow M(OH)_n + n(HOCH_2CH_2OCH_3)$$
$$M = Hf, Zr, \text{and } Ta$$
$$M(OH)_n \rightarrow MO_{n/2} + n/2\ H_2O$$

Figure 3. 1. Schematic diagrams for the preparation of precursor and the dielectric layer formation.

Precursor solutions of the dielectrics were prepared dissolving metal alkoxides in 2-methoxyethanol. The solutions were heated to 80 °C for 30 min to accelerate ligand exchange from isopropoxide (denoted by OiPr in **Figure 3.1**) in the case of Hf and Zr or ethoxide (denoted by OEt) in the case of Ta to 2-methoxyethoxide. This exchange step is critical, as the metal isopropoxide and ethoxide salts lead to rough films with poor optical and electrical qualities. After heating in 2-methoxyethanol, the solutions were spin-coated on top of precleaned substrates under an inert atmosphere. The films were then annealed in ambient air. The exposure of the samples to moisture in air hydrolyses the metal alkoxide ligand bonds into metal hydroxides and generates alcohols (2-methoxyethanol) as byproducts.[48] Thermal annealing was necessary for residual solvent evaporation, complete decomposition, and densification of the films. The spincoating and annealing processes were repeated until the desired thickness of the dielectric layers was acquired. This method successfully produced ultrasmooth and

amorphous metal oxide dielectric layers for all three metals, which will be shown later.

UV–vis absorption spectra of HfO_2, ZrO_2, and Ta_2O_5 are shown in **Figure 3.2**. To identify the nature of optical transition for the processed dielectrics, figures were plotted as Tauc plot of $(\alpha h\nu)^2$ versus $h\nu$ and $(\alpha h\nu)^{1/2}$ versus $h\nu$ to model direct and indirect electronic transitions, respectively, while plots of α versus wavelength provide information about the optical density of the materials.

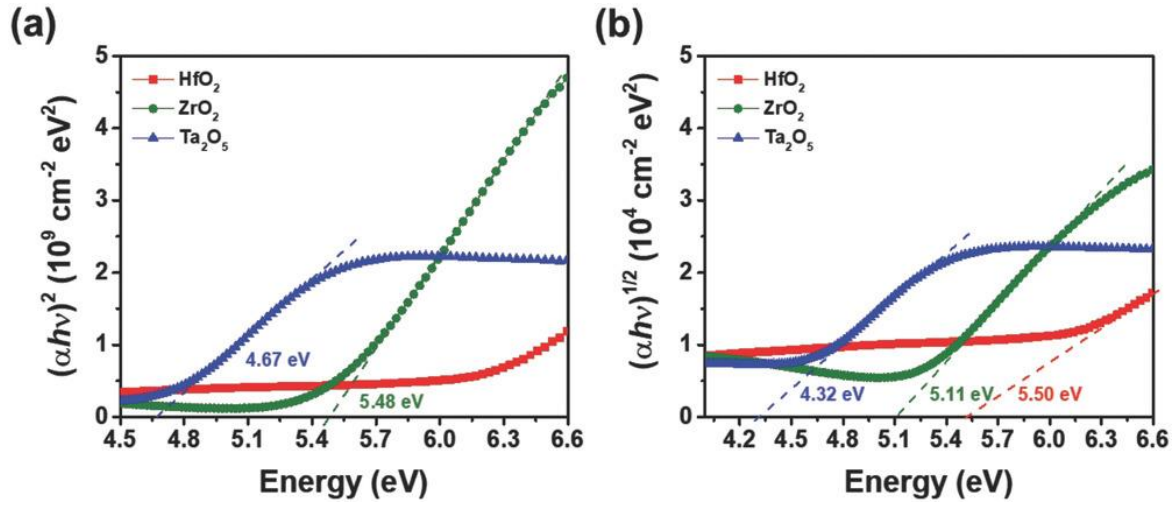

Figure 3. 2. Tauc plots for high-κ dielectrics showing a) direct transition, and b) indirect transitions.

Optical bandgaps of the dielectrics were analyzed via both direct and indirect transitions by finding the x-intercepts of extrapolated tangent lines in their Tauc plots. In **Figure 3.2a**, Ta_2O_5 shows the narrowest direct bandgap among the dielectrics of 4.67 eV, but was wide enough to act as an electrical insulator. ZrO_2 exhibited a direct bandgap of 5.48 eV, which is 0.8 eV wider than the bandgap of Ta_2O_5. We were unable to precisely determine the direct bandgap for HfO_2 as its absorption onset occurred near 180 nm, which is near the detection limit for typical UV–vis spectrometers. Yet, it is apparent that HfO_2 possesses the widest bandgap among three dielectrics. **Figure 3.2b** shows the indirect transitions of the three dielectrics. In common with the direct transition, the widest bandgap was observed for HfO_2 (5.50 eV) followed by ZrO_2 (5.11 eV) and Ta_2O_5 (4.32 eV).

In order to reduce the uncertainty of the electronic transitions of HfO_2 estimated from UV–vis spectrometry, high resolution electron energy loss spectroscopy (HREELS) measurements were carried out. From the data shown in **Figure 3.3**, we confirm that HfO_2 exhibits a direct electronic transition with a bandgap of 5.89 eV.

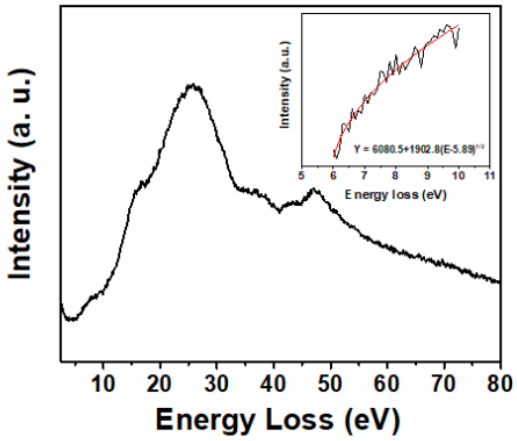

Figure 3. 3. HREELS spectrum of an HfO_2 dielectric layer. Inset: curve fitted using the relation $A+B(E-E_g)^{1/2}$ for direct electronic transitions. A = 6080.5, B = 1902.8, and Eg = 5.89.

Surface morphology and roughness of the high-κ dielectrics were investigated by atomic force microscopy (AFM) as shown in **Figure 3.4**. All the three dielectrics have smooth surface morphology and extremely low root-mean-square roughness of 0.15, 0.18, and 0.18 nm for HfO_2, ZrO_2, and Ta_2O_5, respectively. These smooth surface morphologies facilitate efficient charge transport under FET operation by avoiding charge carrier trapping.

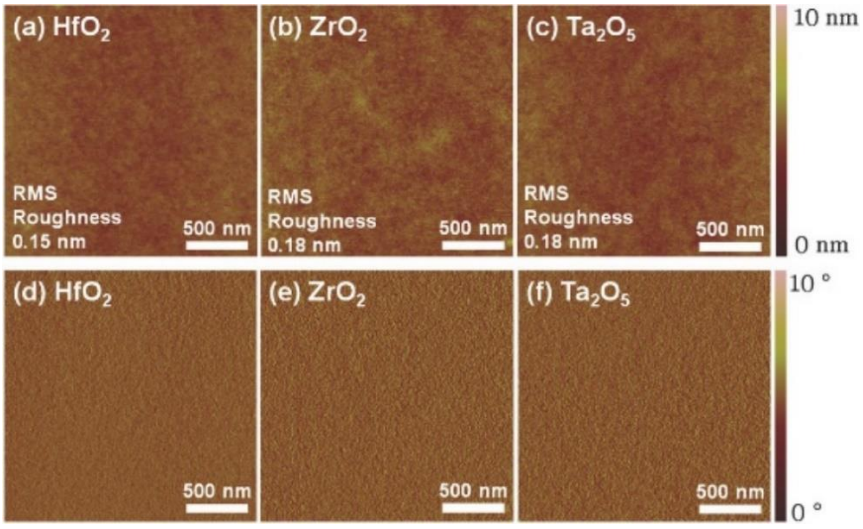

Figure 3. 4. AFM topographic and phase images for a,d) HfO_2, b,e) ZrO_2, and c,f) Ta_2O_5, respectively.

The oxidation states of the metal cations in the dielectric layers were investigated via X-ray photoelectron spectra (XPS, see **Figure 3.5**). In **Figure 3.5a**, the peaks at 16.8 and 18.4 eV of the HfO_2 films correspond to Hf $4f_{7/2}$ and Hf $4f_{5/2}$ transitions. **Figure 3.5d** exhibits two peaks at 182 and 184.4 eV, corresponding to Zr $3d_{5/2}$ and Zr $3d_{3/2}$ electrons. Similarly, sharp spin-orbit doublet peaks for Ta element observed at 26.7 and 28.7 eV correspond to Ta $4f_{7/2}$ and Ta $4f_{5/2}$, respectively, in **Figure 3.5g** (Supporting Information). These results are consistent with a +4 oxidation state for Hf,[49-50] + 4 for Zr,[51-52] and +5 for Ta.[53] An O1s peak around 530 eV and distinct shoulder around 531 eV corresponding to surface hydroxyl groups were observed for HfO_2 and ZrO_2 dielectrics (see, **Figures 3.5b,e**), but the shoulder was not observed in the spectrum for Ta_2O_5 (**Figure 3.5h**). These results confirm the chemical compositions of the dielectric layers to be HfO_2, ZrO_2, and Ta_2O_5. In addition to identifying the bonding states of different elements, XPS can be used to estimate the relative composition of materials. Specifically, the ratio of metal to oxygen was measured to be 1:2.57 for HfO_2, 1:2.15 for ZrO_2, and 2:5.59 for Ta_2O_5, respectively. Negligible residual carbon peaks were observed in all samples even after averaging 5 scans to reduce signal to noise ratio (**Figure 3.5c,f,i**), indicating that the organic solvents and alkoxide ligands used to process the films had thoroughly hydrolyzed and evaporated from the film surface.

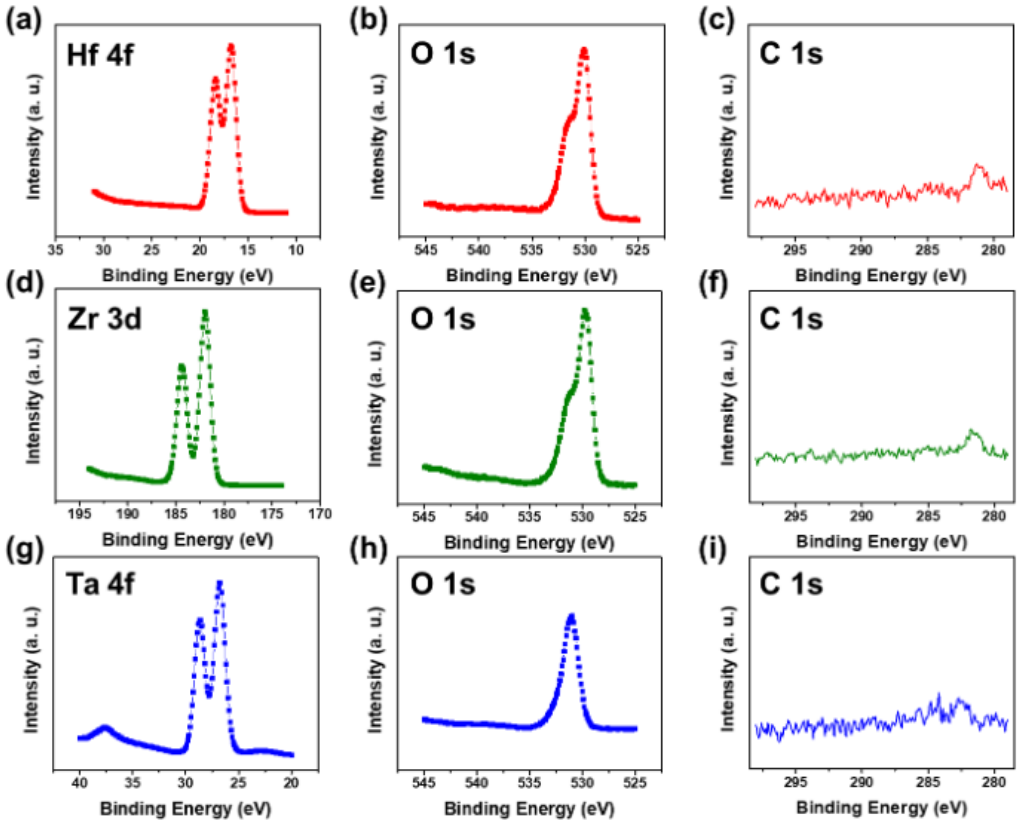

Figure 3. 5. XPS spectra for (a, b, c) HfO_2, (d, e, f) ZrO_2, and (g, h, i) Ta_2O_5 dielectrics.

Further investigation of the dielectric layers via X-ray diffraction (XRD) (**Figure 3.6**) reveals their crystal structures to be amorphous in nature. No distinct, sharp peaks were observed for any of the three dielectric films and all three films exhibited a broad, amorphous fingerprint in the range of 2θ – 20 to 40° in all the XRD spectra collected for the dielectrics.

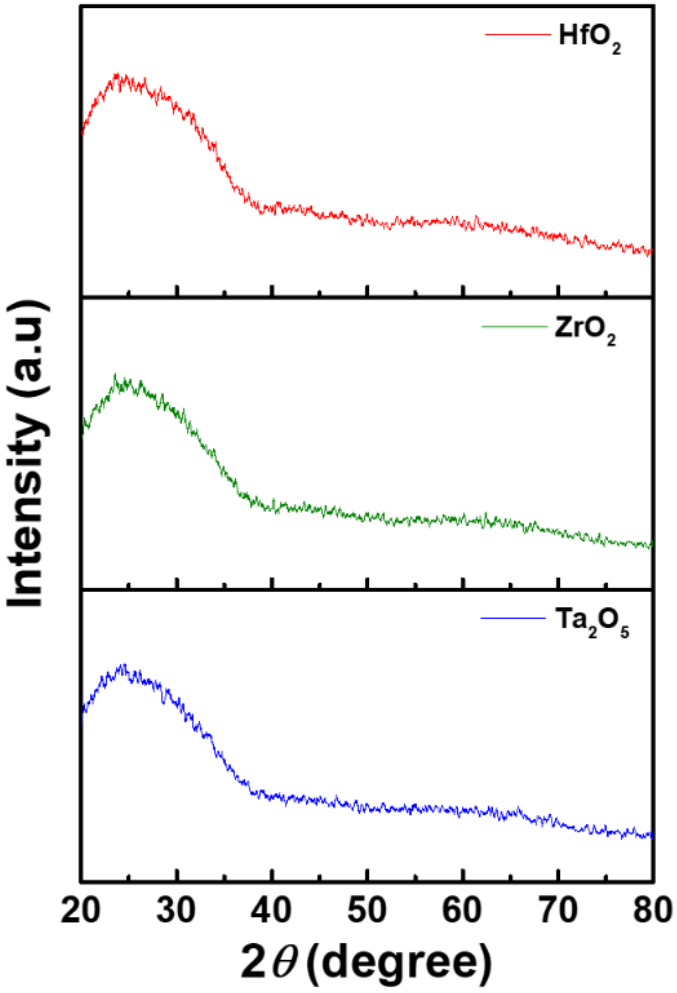

Figure 3. 6. XRD patterns for HfO_2, ZrO_2, and Ta_2O_5 dielectrics.

In order to characterize electrical properties of the three dielectrics, planar capacitors were fabricated by sandwiching the dielectric films between indium tin oxide (ITO) and Ag electrodes. Measured current density versus voltage (*J–V*) characteristics for the capacitors are shown in **Figure 3.7a**.

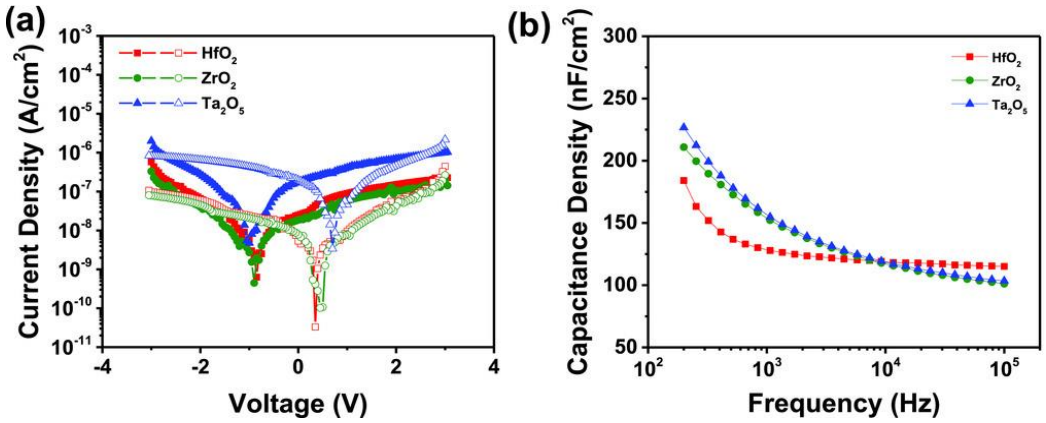

Figure 3. 7. a) Current density vs. voltage and b) capacitance density vs. frequency of the device with high-κ dielectrics annealed at 200 °C. In (a), filled symbol represents the forward scan from −3 to 3 V and empty symbol represents the reverse scan from 3 to −3 V.

Thicknesses of the dielectric layers were carefully optimized to get uniform and thick layers by controlling the concentration of the precursor solution, spin-rate, and the number of coats. Measured current densities for all dielectrics were ≈10^{-7} A cm^{-2} for applied biases from −3 to 3 V. Notably, HfO_2 and ZrO_2 capacitors showed one order lower current density than Ta_2O_5 devices. Asymmetric *J–V* hysteresis was observed for all the capacitors, which may be attributed to charge carrier trapping at the metal/dielectric interface or polarization of the amorphous dielectrics during the charging and discharging process and is commonly observed in high-κ dielectric materials. Capacitance densities were measured to be 119.09, 117.88, 119.39 nF cm^{-2} at 10 kHz for HfO_2, ZrO_2, Ta_2O_5 dielectrics, respectively, as shown in **Figure 3.7b**. These similar capacitance densities allow all three materials to facilitate channel control via modulated gate bias in FET devices with a similar operating range, as will be shown later. Breakdown voltages were measured by applying external bias until the dielectrics lost their insulating properties and exhibited significant current leaking. Each dielectric, prepared using conditions optimized for FET devices, started to break down at 8.82 ± 2.28, 4.92 ± 0.41, and 8.57 ± 1.89 V for HfO_2, ZrO_2, and Ta_2O_5, respectively. It should be noted that the breakdown voltage is not a figure of merit which is independent on the thickness of the layer.[54] Nonetheless, the dielectric films were all of comparable thickness to standard SiO_2 dielectrics used in FET devices (on the order of ≈100–200 nm) and were stable throughout the operating voltage range of ±3 V.

Film thickness information for each dielectric layer was measured via cross-sectional scanning electron microscope images (**Figure 3.8**); averaged thicknesses of for each dielectric film were 103.6,

168.5, and 199.3 nm, respectively, with corresponding dielectric constants of 13.9, 22.4, and 26.9 for HfO_2, ZrO_2, and Ta_2O_5, respectively. Interestingly, the dielectric constants of ZrO_2 and Ta_2O_5 are comparable with values measured from their crystalline counterparts.[55-56]

Figure 3. 8. SEM images of high-κ dielectrics prepared under optimized conditions. (Left: HfO_2, Middle: ZrO_2, Right: Ta_2O_5).

To evaluate the performance of the dielectric films in low operating voltage FETs, we fabricated FETs with a bottom-gate top-contact (BG-TC) structure, using solution-processed CdS films as n-type transport layers which have previously been reported to have good electron transport properties in FETs.[28] Since SiO_2 has low dielectric constant of 3.9, high operating voltages of at least over 40 V are needed to switch on FETs, which is not suitable for low-power electronic devices. Our solution-processed high-κ dielectrics, however, were successful in producing FET devices with an effective operating range of ±3 V for gate and drain biases; more than an order of magnitude lower than the SiO_2 reference dielectric. Furthermore, to the best of our knowledge, this is the first report to demonstrate high-performance FETs using a solution-based Ta_2O_5 dielectric layer.

Transfer and output characteristics of CdS FETs with high-κ dielectrics and SiO_2 are shown in **Figure 3.9** and detailed charge transport parameters are described in **Table 3.1**. In order to focus on the effect of dielectric materials on the transistor characteristics, no special processing procedures (such as exposure to air, multiple annealing steps, etc.) were used and the mobilities were consistent other reported mobility values (≈0.1–9 $cm^2\ V^{-1}\ s^{-1}$) for solution deposited CdS FETs.[57-62]

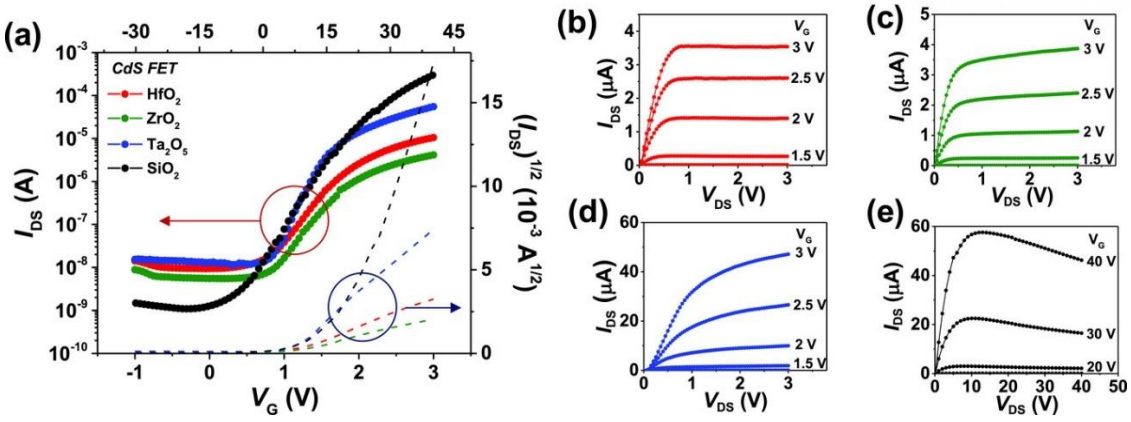

Figure 3. 9. Electrical characteristics of CdS FETs with high-κ dielectrics and SiO_2 dielectric as a reference device. a) Transfer curves for CdS FETs with different dielectrics. Gate voltage was swept from −1 to 3 V for high-κ dielectrics and −30 to 40 V for SiO_2. b–e) Output curves for CdS FETs with HfO_2, ZrO_2, Ta_2O_5, and SiO_2 dielectrics, respectively.

Table 3. 1. Summary of charge transport characteristics for CdS, P3HT, and PCBM FETs

Transport layer	Dielectric	μ[a)] [cm^2 V^{-1} s^{-1}]	I_{on}/I_{off} [×10^3]	V_{th} [V]
CdS (n-type)	HfO_2	1.02 (0.63 ± 0.21)	1.09 (0.78 ± 0.32)	1.17 (1.01 ± 0.13)
	ZrO_2	0.38 (0.22 ± 0.09)	0.75 (0.50 ± 0.28)	1.03 (0.98 ± 0.04)
	Ta_2O_5	2.97 (2.13 ± 0.76)	4.65 (2.53 ± 2.02)	1.00 (0.98 ± 0.02)
	SiO_2	1.62 (1.18 ± 0.44)	272 (243 ± 293)	18.4 (15.2 ± 3.2)
Transport layer	**Dielectric**	**μ[a)] [×10^{-3} cm^2 V^{-1} s^{-1}]**	**I_{on}/I_{off} [×10^3]**	**V_{th} [V]**
P3HT (p-type)	HfO_2	1.48 (0.79 ± 0.56)	0.53 (0.31 ± 0.23)	-0.89 (-0.43 ± 0.46)
	ZrO_2	1.92 (1.82 ± 0.34)	2.59 (1.67 ± 0.92)	-0.98 (-0.93 ± 0.06)
	Ta_2O_5	2.05 (1.92 ± 0.12)	3.23 (4.54 ± 0.13)	0.07 (-0.02 ± 0.09)
	SiO_2	1.27 (1.11 ± 0.13)	31.7 (34.1 ± 2.38)	-11.6 (-13.7 ± 2.1)
PCBM (n-type)	HfO_2	1.09 (0.99 ± 0.09)	0.62 (0.46 ± 0.15)	0.99 (0.98 ± 0.07)
	ZrO_2	2.36 (2.16 ± 0.47)	1.34 (1.40 ± 0.63)	1.29 (1.34 ± 0.17)
	Ta_2O_5	8.69 (6.85 ± 1.86)	1.28 (1.56 ± 0.84)	1.34 (1.39 ± 0.04)
	SiO_2	4.89 (3.15 ± 0.98)	8.34 (8.25 ± 0.09)	10.6 (14.8 ± 4.15)

[a)]Average values measured for 10 devices are stated in parenthesis

In the case of SiO_2 as a reference device, the electron mobility (μ_e) was calculated to be 1.62 $cm^2 V^{-1} s^{-1}$ at 40 V drain–source voltage (V_{DS}). For the high-κ dielectrics, μ_e was calculated to be 1.02, 0.38, and 2.97 $cm^2 V^{-1} s^{-1}$ for HfO_2, ZrO_2, and Ta_2O_5 at 3 V of $V_{DS,}$ respectively. All the high-κ dielectrics showed comparable electron mobility to SiO_2, and especially Ta_2O_5 showed the best FET transfer properties among the dielectrics (83% improvement in the mobility). The measured mobilities and currents through a transport material in FET devices are strongly affected by the properties of the gate dielectric[63-64] and the increased mobility measured on the Ta_2O_5 dielectric suggests that the Ta_2O_5/CdS interface may be more homogenous or possess fewer electron traps than the other dielectrics. Off-current (I_{off}) values of high-κ dielectric based FETs were measured as 9.62, 5.50, and 11.8 nA for HfO_2, ZrO_2, and Ta_2O_5, respectively. These low I_{off} values correlated with the leakage currents observed in the capacitors as discussed previously in **Figure 3.7a**. Threshold voltage (V_{th}) is an important metric associated with low operating voltages and quantifies the advantages of using high-κ dielectrics. Compared to 18.4 V of V_{th} in SiO_2, the threshold voltages were observed to be more than an order of magnitude lower at 1.17, 1.03, and 1.00 V for HfO_2, ZrO_2, and Ta_2O_5, respectively.

In order to prepare compact and dense dielectric layers and investigate the effect of film thickness on device characteristics, we varied the number of coats, the concentrations of precursor solutions from 150 to 95 mg mL^{-1} and annealing temperature from 200 to 300 °C. Using less than three coats led to a high rate of device failure, while more than 3 coats led to generally decreased source–drain current and increased threshold voltage. Thinner dielectric films could be prepared by reducing the solution concentration. As shown in **Figure 3.10**, the performance of devices using 3 coats of solutions at 95 mg mL^{-1} concentration was degraded, with higher I_{off} and lower I_{on}/I_{off}, compared to optimized devices (**Figure 3.9a**). This result can be attributed to current leakage through the thinner dielectric leading to increased I_{off}.

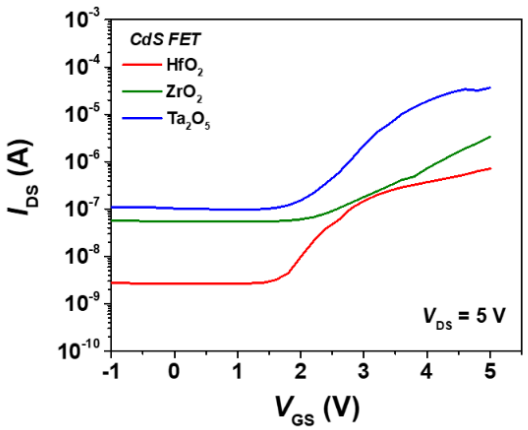

Figure 3. 10. Transfer curves for CdS FETs fabricated by following experimental conditions; 95 mg/ml of precursor solution concentration, and the films were annealed at 300 °C.

The hysteresis of CdS transistors is shown in **Figure 3.11**. Devices using HfO_2 and ZrO_2 dielectrics showed negligible hysteresis, while devices with Ta_2O_5 dielectrics showed very low hysteresis with less than 500 mV offset between forward and reverse scans.

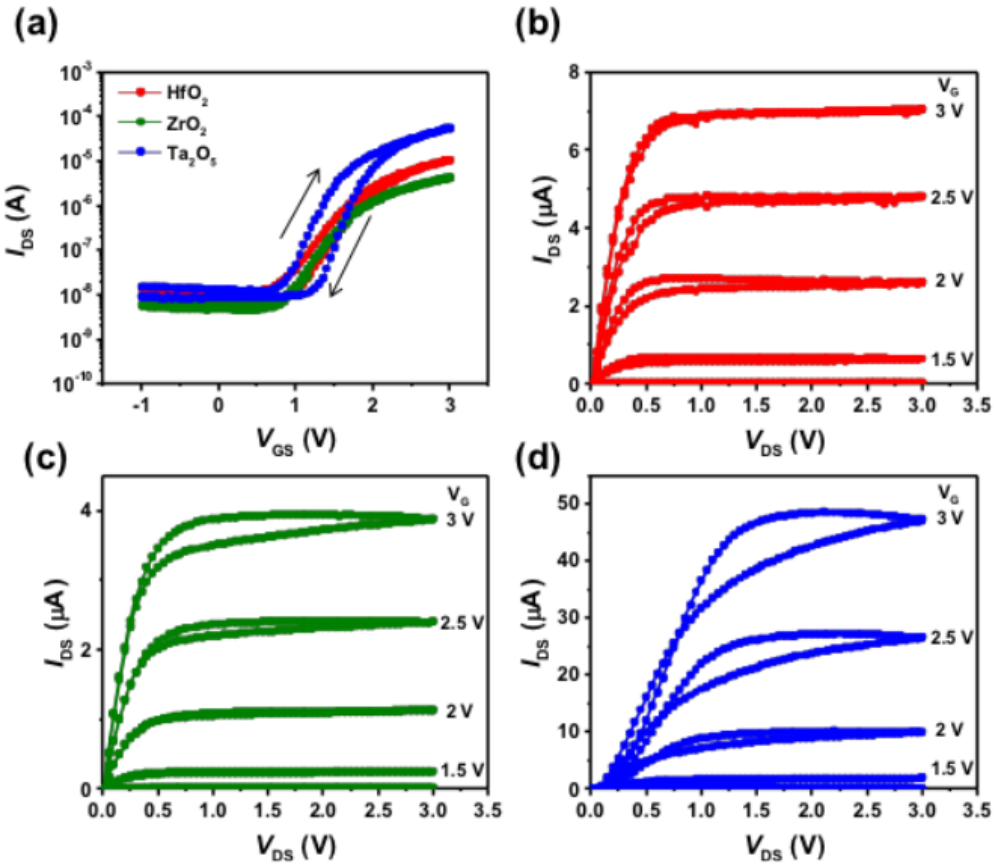

Figure 3. 11. Hysteresis behavior of (a) transfer and (b-d) output curves for CdS FETs.

To investigate applicability of the dielectric films in p-channel operation as well as with organic materials, we prepared organic FETs (OFETs) using the high-κ dielectrics. We used P3HT as a p-type channel material and PCBM as a n-type channel material; these transport materials are well studied and generally representative of organic semiconductors.[65] Again, in order to focus on the influence of dielectrics on FET characteristics, unadulterated P3HT and PCBM films were used without any special processing procedures to enhance their performance, leading to mobilities consistent with previous reports for these transport materials.[27, 66] Transfer characteristics and detailed charge transport properties for P3HT and PCBM FETs are shown in **Figure 3.12** and **Table 3.1**, respectively, and output characteristics are presented in **Figure 3.13**. In the case of P3HT FETs, the hole mobility (μ_h) through the channel was calculated to be 1.48×10^{-3}, 1.92×10^{-3}, and 2.05×10^{-3} $cm^2\ V^{-1}\ s^{-1}$ for HfO_2, ZrO_2, and Ta_2O_5 dielectrics, respectively, at a V_{DS} bias of −3 V. For PCBM FETs, μ_e through the channel was calculated to be 1.09×10^{-3}, 2.36×10^{-3}, and 8.69×10^{-3} $cm^2\ V^{-1}\ s^{-1}$ for HfO_2, ZrO_2, and Ta_2O_5,

respectively, at a V_{DS} bias of 3 V. Like previous CdS FET results, all the high-κ dielectrics shows comparable charge transport ability to SiO_2 ($\mu_h = 1.27 \times 10^{-3}$ and $\mu_e = 4.89 \times 10^{-3}$ cm^2 V^{-1} s^{-1} for P3HT and PCBM FETs, respectively). Ta_2O_5 especially leads to more efficient hole (61% higher) and electron (78% higher) transport through the channel compared to HfO_2, ZrO_2, and SiO_2 dielectrics in both p- or n-type OFETs. Threshold voltages were also dramatically reduced to near 1 V in all of the OFET devices with high-κ dielectrics.

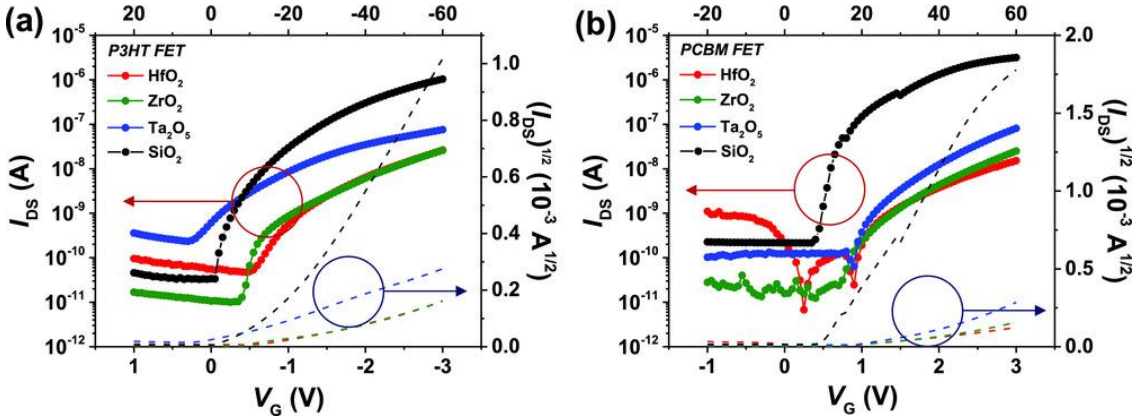

Figure 3. 12. Electrical characteristics of OFETs with high-κ dielectrics and SiO_2 dielectric as a reference device. a) Transfer curves for P3HT FETs with different dielectrics. b) Transfer curves for PCBM FETs with different dielectrics. Gate voltage was swept from −1 to 3 V for high-κ dielectrics and −20 to 60 V for SiO_2.

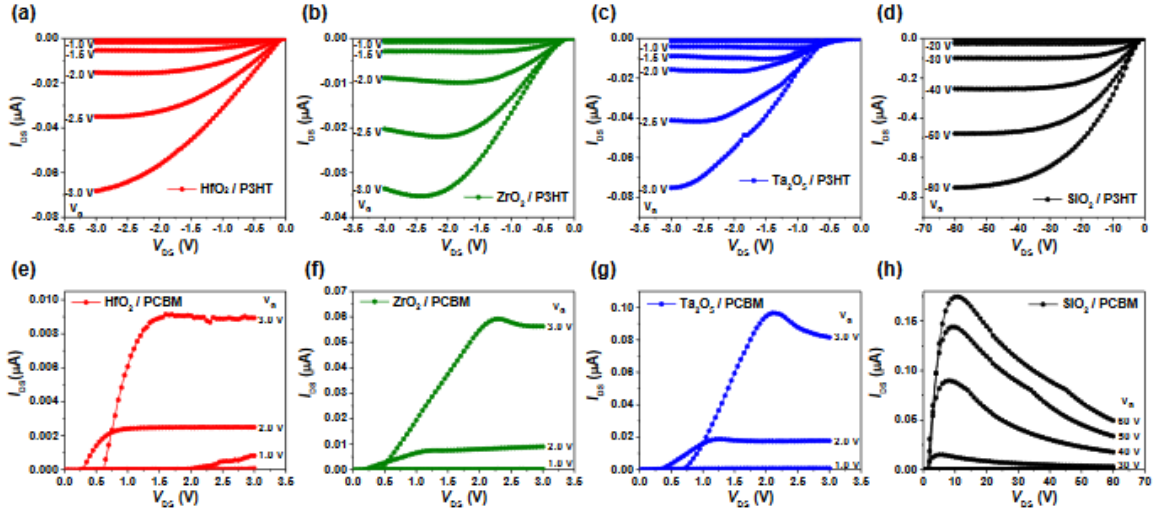

Figure 3. 13. Output characteristics of OFETs using HfO_2 (a, e), ZrO_2 (b, f) and Ta_2O_5 (c, g) high-κ dielectrics compared to devices using a SiO_2 dielectric (d, h) as a reference. (a-d) P3HT devices. (e-h) PCBM devices.

Gate leakage currents for CdS devices with three dielectrics are shown in **Figure 3.14**. The measured I_{off} trends for all the FETs followed the leakage current results observed in both the capacitor devices and FET devices (excluding the case of HfO_2). HfO_2 showed notably increased gate leakage currents in

FET measurements compared to those measured in capacitor devices. During CdS FET fabrication, a CdS layer was formed on the dielectric layers involving a 300 °C annealing step; the increased leakage current in CdS FETs with HfO_2 dielectrics might be due to instability of the HfO_2 layer at 300 °C when in contact with CdS.

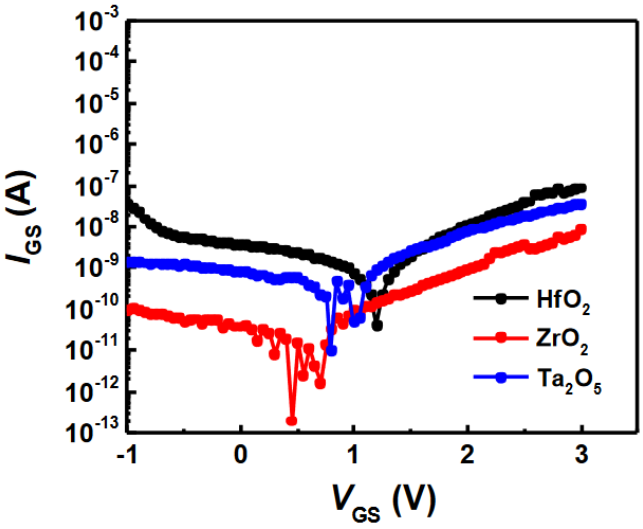

Figure 3. 14. Gate leakage current of CdS FETs using HfO_2, ZrO_2, and Ta_2O_5 high-κ dielectrics.

We measured transient drain current under constant drain and gate potential in CdS FETs using three different dielectrics (**Figure 3.15**). We observed that the measured drain currents decreased over time before saturating at a constant value after about 30 min. We attribute the decreases in current in the first 5 min to the filling of shallow electron traps at the interface between transport and dielectric layers.[67]

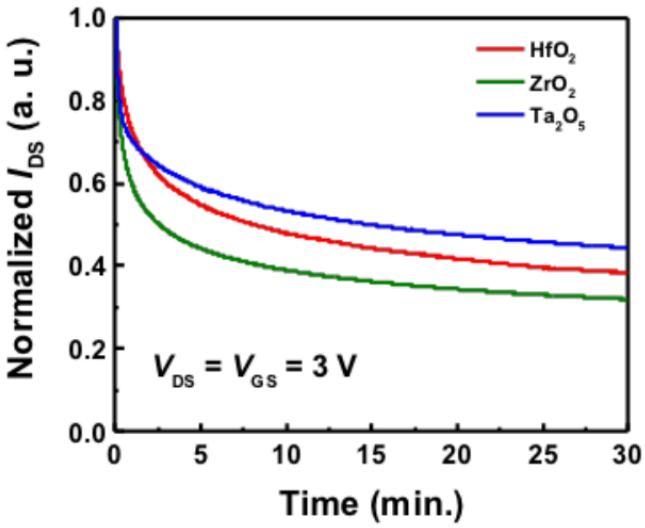

Figure 3. 15. Transient drain current response of CdS FETs with different dielectrics.

Because the same transport material was used (CdS) in all the devices, the trap density is solely dependent on the dielectric layer. Ta_2O_5 exhibited the lowest current decay and we infer that it possessed the lowest density of traps among the three dielectrics. From the measured transfer and output curves shown in **Figures 3.12** and **3.13**, the Ta_2O_5 dielectrics led to superior performance in electron transport among three dielectrics, although all of dielectric showed comparable performance in hole transport. We attribute this to low electron trap density of Ta_2O_5 dielectric compared to other dielectrics, and similar hole trap density for all three dielectric types. In summary, all of these results suggest that the three high-κ dielectrics functioned well as both p- and n-type FETs under low bias conditions, with measured mobilities for a variety of transport materials being comparable to those observed with SiO_2.

3.4 Conclusion

In conclusion, we have developed a universal, facile, and innocuous solution-processing method for depositing high-κ Ta_2O_5 dielectric films for application in a wide variety of FET devices. We also confirmed that this processing scheme is applicable to HfO_2 and ZrO_2 high-κ dielectrics as well, and confirmed that Ta_2O_5 dielectrics consistently yielded the highest performance compared to the other metal oxides. All the high-κ dielectric layers were simply prepared by spin coating solutions of metal alkoxide precursors in 2-methoxyethanol, followed by mild thermal annealing at 200 °C. The prepared dielectric layers showed κ values of 13.9, 22.4, and 26.9 for HfO_2, ZrO_2, and Ta_2O_5, respectively. In addition, after processing optimization, low leakage current densities around 10^{-7} A cm^{-2} were observed in planar capacitors within a bias range of ±3 V. All three high-κ dielectrics including HfO_2, ZrO_2, and Ta_2O_5, were successfully applied in low operating voltage inorganic (n-type) and organic (p- and n-type) FETs. All of the high-κ dielectrics showed comparable charge carrier mobilities to SiO_2 at a dramatically reduced operating range of ±3 V gate bias. In particular, Ta_2O_5 based FETs consistently showed the highest mobility among the four types of dielectric layers. In inorganic CdS FETs with Ta_2O_5 gate dielectric, the electron mobility was measured to be 2.97 cm^2 V^{-1} s^{-1}, which is 83% higher value compare to SiO_2 based FET (1.62 cm^2 V^{-1} s^{-1}). To the best of our knowledge, this is the first demonstration of FET applications utilizing solution-processed Ta_2O_5 as gate dielectrics with outstanding device performance. This work introduces a simple and nontoxic fabrication strategy for preparing Ta_2O_5 dielectric films and demonstrates their potential for use in a wide variety of low operating voltage electronic devices.

CHAPTER 4. Solution-Processed CdS Transistors with High Electron Mobility

The content of this chapter is published in *RSC Advances* **4**, 3153 (2014)

4.1 Research background

The rapid development and large demand for consumer electronics ranging from flat-panel televisions to mobile devices has spurred a great interest in routes to achieve high-performance field effect transistors (FETs) using low-cost materials, flexible substrates and novel processing techniques. In this regard, routes to fabricate FETs via solution processing techniques have attracted a great deal of academic and commercial interest, as solution-processed devices are amenable to mass-production techniques such as ink-jet printing and roll-to-roll processing; strategies have been developed to process both inorganic[68] and organic semiconductor materials in these ways.[12, 69] Solution-processed organic FETs have developed rapidly and show good performance, however, mobilities of conjugated organic materials still lag behind inorganic materials. Graphene based devices[70] as well as solution-processed inorganic nanoparticles (NPs)[71-72] and nanosheets[73] have emerged as routes to easily prepare FETs under mild temperatures and pressures, with excellent results, demonstrating that the investigation of novel processing procedures for FETs can be fruitful.

Cadmium sulfide (CdS) shows great potential as a versatile semiconductor that can be deposited in a number of ways. FETs have been prepared from CdS by thermal evaporation, yielding charge carrier mobilities (μ) of $\sim$50 $cm^2\ V^{-1}\ s^{-1}$,[74] using chemical bath deposition to yield μ in the range of 0.1 to 9 $cm^2\ V^{-1}\ s^{-1}$,[57-62] and up to 350 $cm^2\ V^{-1}\ s^{-1}$ by chemical vapor deposition,[75] however, these methods are expensive and/or laborious compared to methods such as spin-coating, doctor blading, screen printing or ink-jet printing. Encouraging results have been obtained via the processing of CdS FETs from CdS or CdS/CdSe core–shell NP solutions, yielding μ of up to 30 $cm^2\ V^{-1}\ s^{-1}$.[59, 76-77] However, the operation of FETs does not rely on quantum confinement within nanostructures and carrier transport between NPs may be limited by tunneling barriers between individual NPs,[78] thus, it is of interest to explore routes to obtain bulk CdS via solution processing routes.

The deposition of bulk chalcogenide films directly from solution (i.e. spin-coating or doctor blading) is not well known due to the insolubility of chalcogenide semiconductors. Some chalcogenides may be processed using hydrazine, which has remarkable solvating effects on many chalcogenides, however, the toxicity and reactivity of hydrazine leave a need for a more conventional solvent to process

chalcogenides. Additionally, films processed with hydrazine must be annealed at 400 °C in order to ensure conversion of the solvated material to the pure chalcogenide, in order to obtain the best semiconducting properties.[79] In one report, CdS FETs were prepared by the thermal decomposition of a molecular precursor, yielding bulk CdS with a μ of up to 48 $cm^2 V^{-1} s^{-1}$,[80] substantiating this route as an effective way to obtain semiconducting CdS films.

Here, we report the preparation of high-mobility CdS films suitable for use in FETs via spin-coating and thermal annealing of cadmium thiolates. Cadmium thiolates have previously been employed as routes to obtaining CdS via photodecomposition or thermal decomposition, yielding suspensions or composites of NPs or nanostructures in various media.[81-85] In one case, solar cells were prepared via the thermal decomposition of a Cd thiolate/conjugated polymer mixture, however, little photocurrent generation was observed and current voltage characteristics of the devices were not reported.[86] The preparation of FET devices via the thermal decomposition of solution processed cadmium thiolates currently remains unexplored. This approach shows particular promise in the realm of organic–inorganic hybrid devices, as the inorganic film may be deposited using techniques compatible with organic semiconductors while the preparation of the thiolate precursors is exceedingly simple.

4.2 Experimental details

CdTNT Synthesis

Cadmium oxide (Aldrich, 99.99%, 115 mg), tert-nonyl mercaptan, (Aldrich, >97%, 400 μL) and 10 mL of chloroform are placed in a tightly-capped 20 mL vial and magnetically stirred at 50 ℃ until the brown CdO has dissolved and a viscous, translucent solution is obtained (this typically takes 3-8 weeks). The solution is diluted to 20 mL with additional chloroform, passed through a 0.45 μm PTFE syringe filter and precipitated directly into 200 mL of well-stirred ethanol. The supernatant liquid is decanted and the solid is rinsed with additional ethanol, then dried under a stream of argon. The material is sensitive to UV light.

CdTDT Synthesis

The same procedure employed for CdTNT is used to prepare CdTDT, with the exception that 100 mg of cadmium oxide are used, and tert-dodecyl mercaptan, (Aldrich, >98.5%, 400 μL) is used instead of tert-nonyl mercaptan.

CdTNT Synthesis (II)

Cadmium acetate (Aldrich, 99.995%, 200 mg), tert-nonyl mercaptan, (Aldrich, >97%, 1 mL) and 10 mL of chloroform are placed in a tightly-capped 20 mL vial and magnetically stirred at 50 ℃ overnight yielding a transparent solution. The solution is diluted to 20 mL with additional chloroform, passed through a 0.45 μm PTFE syringe filter and precipitated directly into 200 mL of well-stirred ethanol. The supernatant liquid is decanted and the solid is rinsed with additional ethanol (50 mL), then immersed in a 2% solution of tert-nonyl mercaptan in ethanol for 1 hour. Again, the supernatant liquid is decanted and the solid is rinsed with additional ethanol (3 x 50 mL) then dried under a stream of argon.

Materials characterization

XPS and UPS spectra were collected for CdS films on substrates consisting of silicon with a 40 nm layer of thermally evaporated Au. A UV-vis absorption spectrum was collected from a CdS film prepared by spincoating a CdTNT film on a glass substrate and annealing at 300 ℃ for 30 min in a nitrogen atmosphere. X-ray diffraction was performed on CdS films prepared from thiolates in order to characterize their crystal structure. Single layers did not yield a strong enough signal to identify. Thus, 8 layers were prepared on a silicon substrate using CdTNT precursor.

FET Fabrication and Characterization.

Silicon substrates with a 200 nm oxide layer (Silicon Prime Wafer) were cleaned by scrubbing in a detergent solution, sonicating in a detergent solution (10 min), sonicating in DI water (2 x 10 min) and

sonicating in isopropanol (10 min), then blown dry with compressed nitrogen. The substrates were kept in a closed petri dish in an oven at 100 °C until used. CdTNT or CdTDT were dissolved in chloroform in a nitrogen filled glovebox at concentrations of 8 mg/mL or 15 mg/mL, respectively. The solutions were passed through a 0.45 μm PTFE syringe filter (with some difficulty) and kept in pre-cleaned vials. The solutions were spin-coated by rapidly dispensing 40 μL at a time (using a micropipette) onto pre-cleaned Si/SiO_2 substrates which were already spinning at 1500 rpm. The viscous nature of the solution and low boiling point of chloroform require that the solution be dispensed quickly, before the material on tip of the pipette becomes gelatinous, which tends to result in blemishes in the spincoated film. The films were then annealed on a hotplate under a nitrogen atmosphere at 300 °C for 30 min. A digital image of CdS films prepared on glass substrates is included as a reference showing good quality CdS films free of visible blemishes. If two or more layers were deposited, the first layer(s) were annealed at 300 °C for 5 min, while the final layer was annealed at 300 °C for 30 min. Source and drain contacts were deposited by thermally evaporating Ag slugs (Alfa Aesar, 99.99%) at a pressure of ~ 10^{-6} Torr through shadow masks to yield devices having a channel length of 50 μm and a length to width ratio of 48. Devices were tested using a probe station equipped with a Keithley 4200 semiconductor characterization system under a nitrogen atmosphere.

Solar Cell Fabrication and Characterization

Solar cells were prepared beginning with indium tin oxide (ITO) substrates which were cleaned by scrubbing in a detergent solution, followed by sonication in in a detergent solution (10 minutes), dionized water (10 minutes, twice) and isopropanol (10 minutes). A zinc oxide layer was deposited on top of the ITO substrate in an adaptation of a previously described procedure by spincoating (at 3000 rpm) and annealing (at 110 °C) a filtered precusur solution consisting of 300 μL of diethyl zinc solution (5 wt% in toluene) and 600 μL of anhydrous tetrahydrofuran. CdS layers were prepared as described above, using CdTNT and a single annealing step at 300 °C for 1 minute. PTB7 layers were deposited by spincoating a 10 mg/mL solution in chlorobenzene at 1200 rpm. Devices were completed by thermally evaporating MoO_3/Au electrodes (5 nm / 80 nm) under a vacuum of 10^{-6} Torr through a shadow mask yielding devices with an active area of 13 mm^2. Current density – voltage characteristics were characterized under simulated AM 1.5G solar radiation using a Xenon arc lamp equipped with a KG5 optical filter and calibrated at 100 mW/cm^2 intensity using an NREL certified standard silicon photodiode. External quantum efficiency (EQE) measurements were obtained using a PV measurements OE system equipped with a Xenon arc lamp where monochromated light was chopped at a frequency of 100 Hz and photocurrent response detected with a lock-in amplifier and compared to a reference silicon photodiode.

4.3 Results and discussion

The thiolate precursors used in this study are prepared simply from cadmium oxide (or acetate) and long, tertiary alkyl chain thiolates (**Figure 4.1a**). The use of these starting materials ensures the absence of extraneous elements (i.e. alkali metals, halides, nitrogen bases) which might later contaminate and interfere with the electronic properties of the CdS end product. The reaction between cadmium oxide and the thiols is simple and economical, however, it requires several weeks to complete while the reaction between cadmium acetate and the thiols proceeds overnight. Tertiary alkyl thiols are chosen as tertiary alkyl cadmium thiolates have previously been shown to decompose cleanly to form CdS upon heating at moderate temperatures in the range of 250 to 300 °C.[87-88] Although short alkyl chain cadmium thiolates are insoluble, the use of tertiary dodecyl and tertiary nonylthiols yields soluble cadmium thiolate precursors. After a mixture of cadmium oxide (or acetate), tertiary alkyl thiol and chloroform have magnetically stirred until the solid has dissolved, the mixture is passed through a 0.45 μm PTFE syringe filter to remove undissolved solids and precipitated into ethanol, washed with ethanol, then dried under a stream of argon. The isolated cadmium thiolate can then be dissolved in chloroform and spin-coated onto substrates just as a conjugated polymer or conjugated small molecule film might be processed, and subsequently annealed, as illustrated schematically in **Figure 4.1b**, to obtain CdS films.

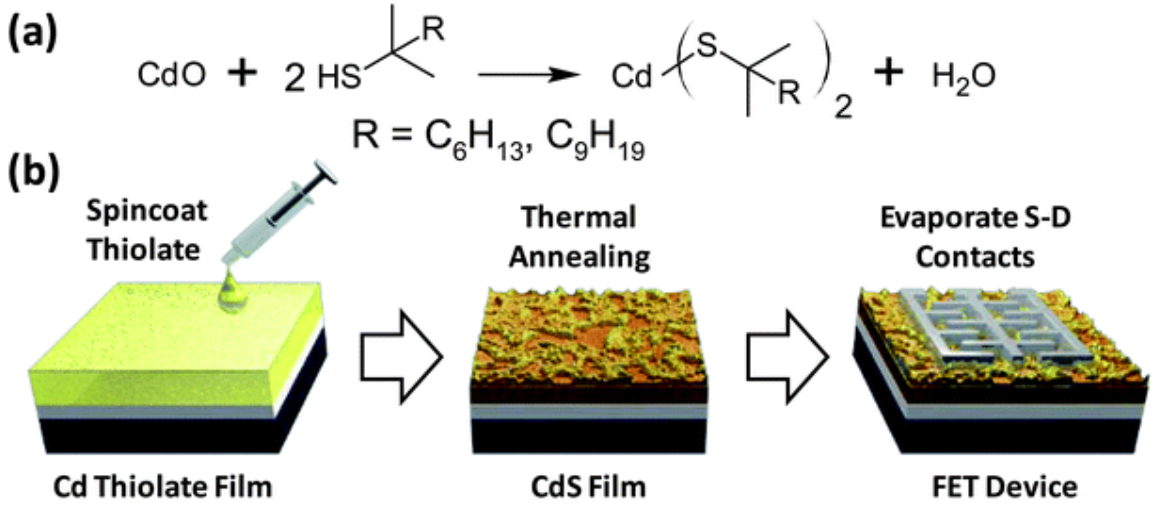

Figure 4. 1. Schematic diagrams. (a) Synthetic scheme for thiolate preparation and (b) illustration of device processing procedure for preparing FETs from the soluble thiolates.

Thermogravimeteric analysis (TGA) of the cadmium tert-nonanethiolate (CdTNT) (**Figure 4.2a**) shows that the powdered material rapidly decomposes in the range of 224 to 239 °C to 38.6% of its original mass, ultimately reaching 37.6% of its original mass by 400 °C, while cadmium tert-dodecanethiolate (CdTDT) (**Figure 4.2b**) decomposes in the range of 224 to 241 °C to 30.5% of its original mass, ultimately reaching 29.5% of its original mass by 400 °C, consistent with the conversion

of the thiolate to CdS and consistent with the reported decomposition of other cadmium thiolates.[61] Although TGA indicates that CdTNT and CdTDT powders decompose to CdS at temperatures near 240 ℃, a hotplate setting of 300 °C was used to consistently decompose spin-coated films of CdTNT and CdTDT and yield CdS films on silicon or glass substrates. A hotplate setting of 250 ℃ was not adequate to reliably decompose the film, likely because the top surface of the film is in contact with an ambient nitrogen atmosphere may be at a marginally lower temperature than the temperature measured by the hotplate. X-ray photoelectron spectroscopy (XPS) spectra of CdS films prepared from CdTNT and CdTDT on Si/Au substrates are consistent with the presence of CdS (**Figure 4.2c**)

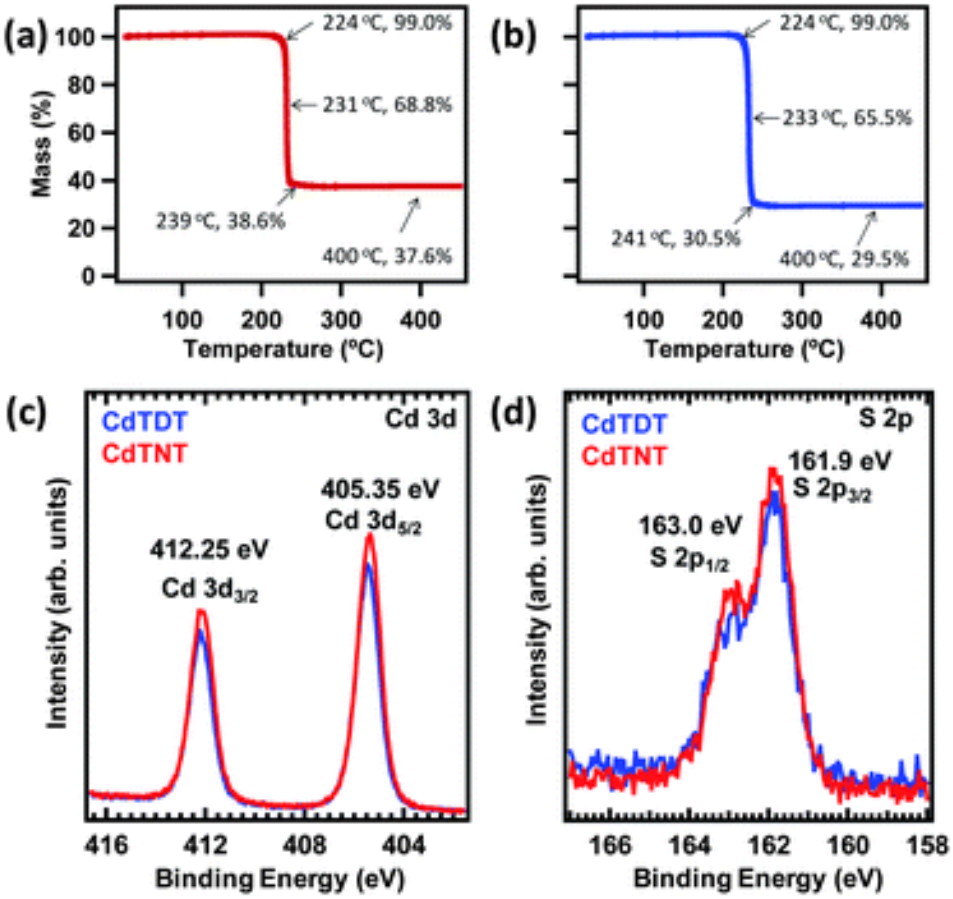

Figure 4. 2. Characterization. TGA plots of (a) CdTNT and (b) CdTDT**.** X-ray photoelectron (c) Cd 3d and (d) S 2p spectra of CdS films.

Detailed XPS plots of the Au, Cd, and S signals are shown in Figure 4.3. A close-up of the Au 4f region (Fig. S1a) reveals that some Au signal is still apparent after depositing the CdS layer, indicating that the films do not completely cover the Au surface or are very thin in places (less than ~30 nm thick). A close-up of the Cd 3d region (Figure 4.3b) reveals binding energies of 412.25 and 405.35 eV for cadmium 3d3/2 and 3d5/2 orbitals, respectively, consistent with Cd-S bonding. A close-up of the S 2p region (Figure 4.3c) reveals binding energies of 163.0 and 161.9 eV for sulfur 2p1/2 and 2p3/2 orbitals,

respectively, consistent with the presence of a metal sulfide. Very little difference is apparent in the XPS spectra of films prepared from either CdTNT or CdTDT.

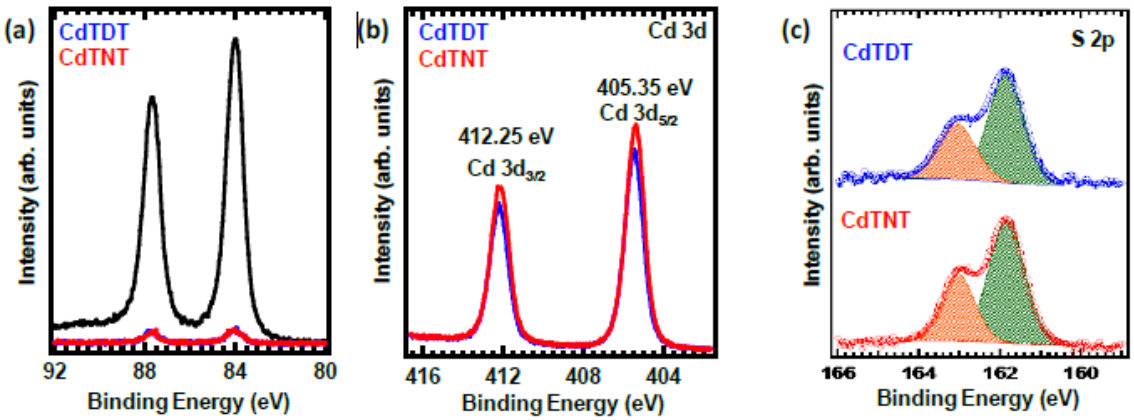

Figure 4. 3. XPS spectra. a) Close-up of Au 4f region of XPS spectra. b) Close-up of Cd 3d region of spectra. c) Close-up of S 2p region of spectra.

A UV-vis absorption spectrum was collected from a CdS film prepared by spincoating a CdTNT film on a glass substrate and annealing at 300 ℃ for 30 min in a nitrogen atmosphere. In **Figure 4.4**, it shows absorption spectrum having an onset of 524 nm and an optical bandgap of 2.37 eV, close to the reported optical bandgap (2.38 eV) for thermally evaporated bulk CdS films using a substrate temperature of 300 °C.

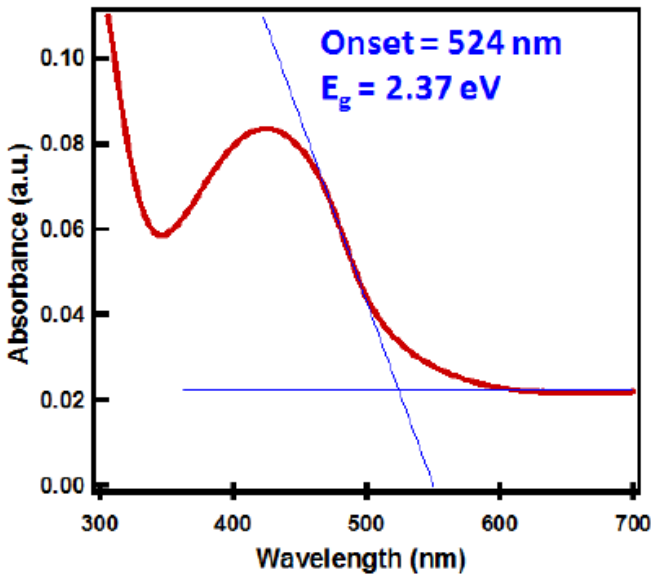

Figure 4. 4. UV-vis absorption spectrum of CdS film prepared by annealing a spin-coated CdTNT at 300 ℃ for 30 min.

UPS spectra were collected from the same CdS films in the same way that XPS samples were prepared. **Figure 4.5** indicate a high binding energy cutoff of 16.41 +/- 0.05 eV for films prepared from either CdTNT or CdTDT. Subtracting this energy from the photon energy (21.22 eV) yields a workfunction of 4.81 +/- 0.05 eV. The low binding energy onset region may be used to calculate the valence band energy, however, the onset is very gradual making it difficult to accurately determine the energy of the band edge. The valence band energy was estimated from the low binding energy onset and determined to be ~6.65 eV for CdS prepared from both CdTNT and CdTDT. Subtracting the optical band gap from the valence band energy yields an approximation of the conduction band energy (~4.3 eV).

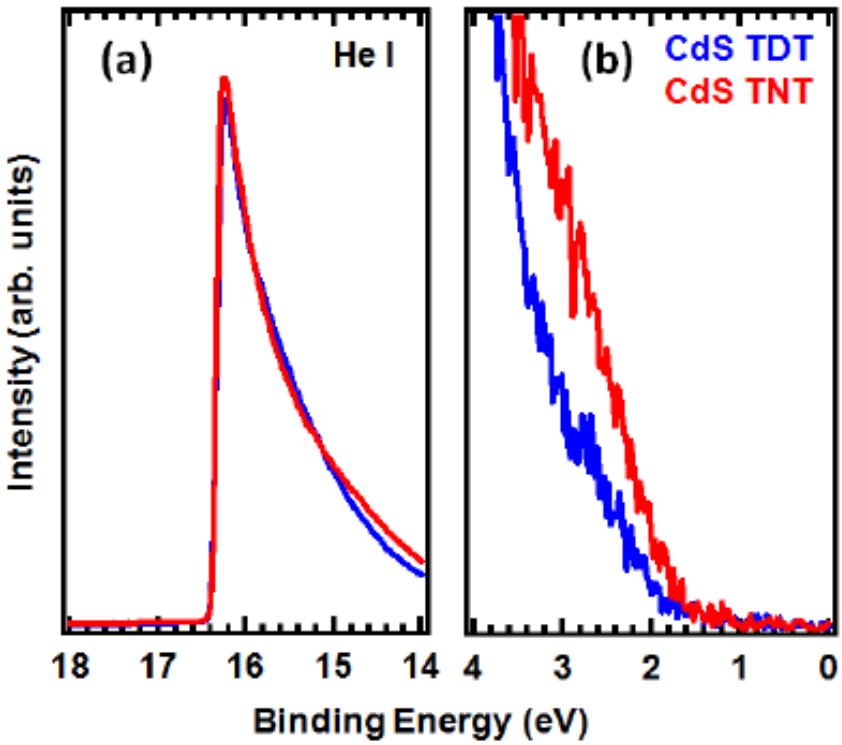

Figure 4. 5. Ultraviolet photoelectron spectra of CdS films prepared from CdTNT and CdTDT. a) Secondary edgy region used to determine work function. b) Low binding energy onset region used to determine valence band energy.

X-ray diffractograms were collected for films prepared on Si substrates (**Figure 4.6**). Although the intensity of the spectra are low due to the films being very thin, the diffraction peaks fit the pattern expected for the Greenokite phase, while Debye-Sherrer analysis of the (110) peak indicate a crystal grain size of approximately 7.0 nm.

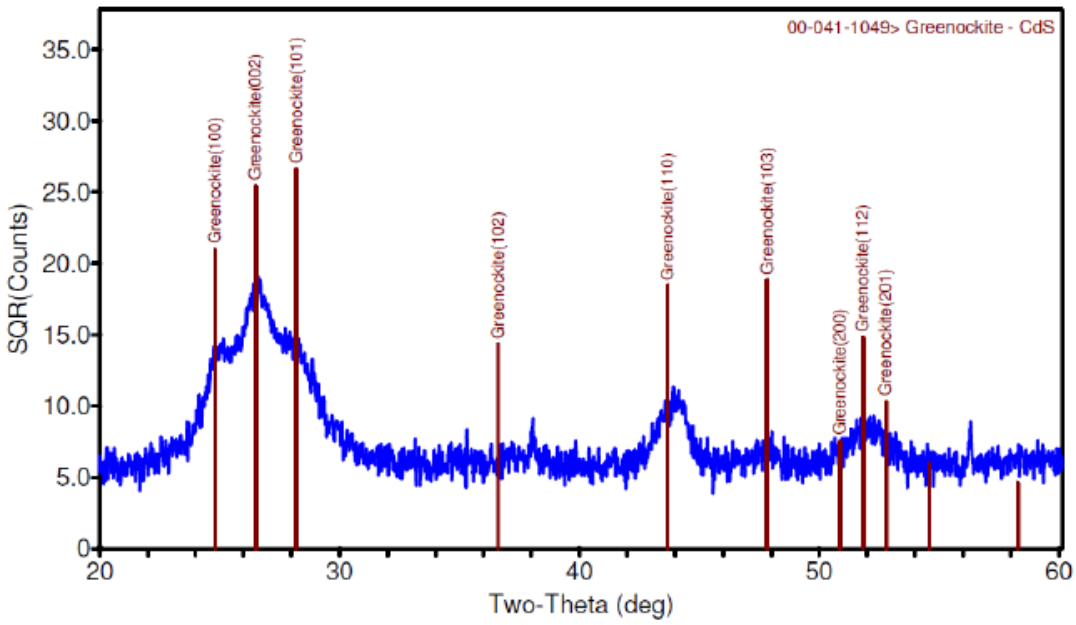

Figure 4. 6. X-ray diffractogram of CdS film prepared by sequentially spincoating CdTNT and annealing at 300 ℃ for 5 min. seven times, followed by a final layer of spincoated CdTNT and annealing at 300 ℃ for 30 min.

Atomic force microscope (AFM) images of the films before and after annealing are shown in **Figure 4.7**. The films of CdTNT and CdTDT are relatively smooth with root–mean–square (RMS) roughness values of 1.1 and 0.6 nm, respectively. After annealing the thiolate films at 300 °C, the films become much rougher (RMS roughness of 21.7 and 14.4 nm for CdS prepared from CdTNT and CdTDT, respectively). The average thickness of CdS features is 39 nm for CdTNT and 28 nm for CdTDT. Multiple layers may be deposited by repeating the spin-coating and annealing steps in order to obtain thicker films. The films are rough compared to typical organic semiconductors, however, the roughness is comparable to that of CdS films prepared by chemical bath deposition (9 to 13 nm),30 which are commonly used as window layers in chalcogenide solar cells. The roughness does not adversely affect their FET behavior (discussed later). Nonetheless, we observed that smoother CdS films could be prepared by exposing the spincoated thiolate film to sulfur vapor at a considerably lower temperature (160 °C) by annealing in a 10 cm Petri dish containing a small amount of elemental sulfur powder (50 mg).

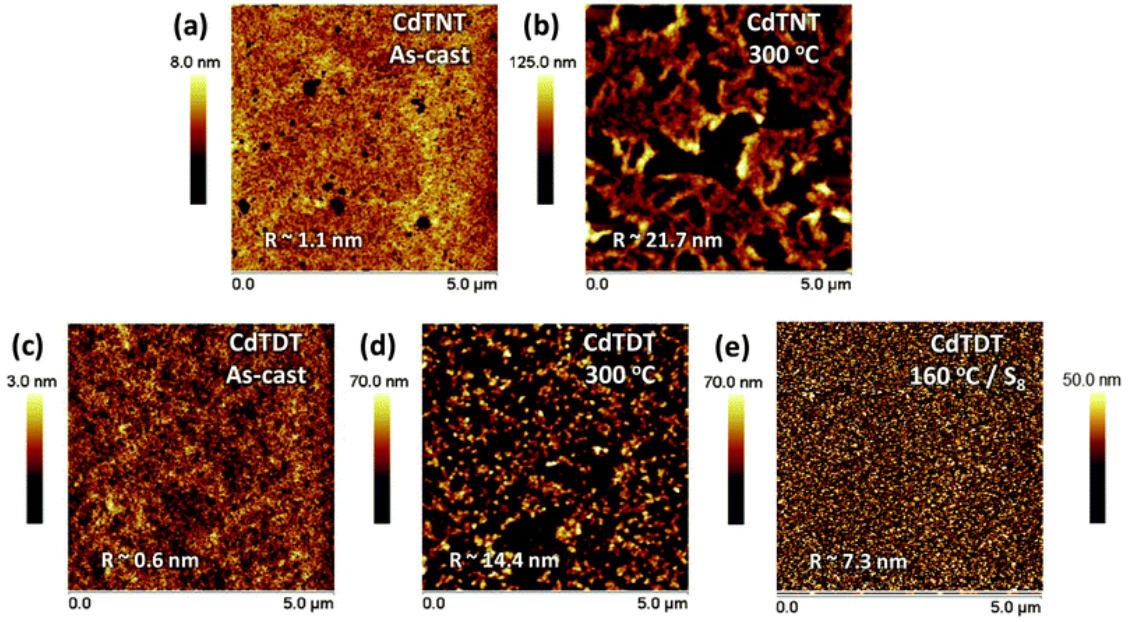

Figure 4. 7. AFM images. (a) Pristine CdTNT film spin-coated from chloroform (8 mg mL^{-1} at 1500 rpm). (b) CdS film after annealing CdTNT at 300 °C for 30 min. (c) Pristine CdTDT film spin-coated from chloroform (15 mg mL^{-1} at 1500 rpm). (d) CdS film after annealing CdTDT at 300 °C for 30 min. (e) CdS film after annealing CdTDT at 160 °C for 15 min in the presence of elemental sulfur.

FETs were fabricated by depositing CdS films as described above onto silicon substrates with a 200 nm oxide layer, followed by thermal evaporation of Ag source and drain contacts. Immediately after fabrication, transfer curves exhibit n-type behavior with large leakage currents as shown in **Figure 4.8**. The device characteristics change dramatically after exposure to air for 1 hour. The off-current is reduced dramatically after air exposure; however, the overall current through the device also drops by several orders of magnitude and significant hysteresis is apparent. This increase in resistivity is consistent with effects of oxygen adsorption on thin CdS films previously observed by Bube, et al.[89] and the observed depletion of electron density in CdS nanobelt devices upon exposure to oxygen.[90] These undesirable effects can be resolved by one final annealing step at 300 °C in a nitrogen atmosphere, leading to devices with reduced leakage currents and generally good performance.

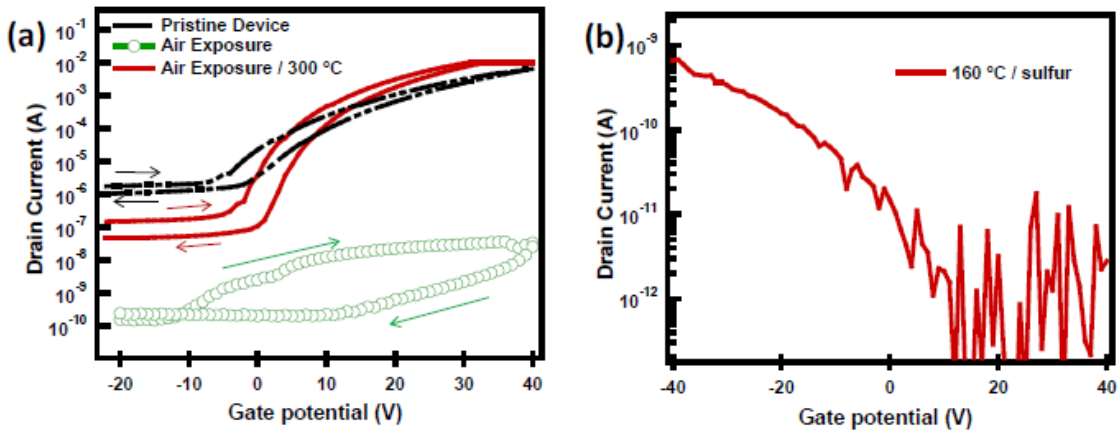

Figure 4. 8. Transfer curve of CdS devices. a) Comparison of pristine CdTNT devices after annealing at 300 °C to devices exposed to air (1 hr.) and devices after air exposure and additional annealing for 30 min. at 300 °C in nitrogen. b) Device prepared by annealing a CdTDT film in the presence of elemental sulfur at 160 °C for 15 min.

Output and transfer curves of these devices are shown in **Figure 4.9**. CdTNT leads to slightly higher μ than CdTDT, where μ (average of 8 devices) and on/off ratios are 41 ± 16 $cm^2\ V^{-1}\ s^{-1}$ and $>10^5$ and 21 ± 9 $cm^2\ V^{-1}\ s^{-1}$ and $\sim 10^6$ for devices prepared from CdTNT and CdTDT, respectively. The highest mobilities observed were 61 and 36 $cm^2\ V^{-1}\ s^{-1}$ for CdTNT and CdTDT, respectively. The larger, interconnected domains observed in the morphology of CdS films prepared from CdTNT seem to result in greater overall mobility. Although AFM images and high-resolution XPS spectra (**Figure 4.3** and **4.7**) indicate that the films may not completely cover the substrate surface, attempts to increase surface coverage by depositing multiple layers of CdS did not lead to a significant increase in mobility if the precursor solution was at least 8 mg mL^{-1} in the case of CdTNT and 15 mg mL^{-1} in the case of CdTDT.

Films prepared using lower concentrations lead to poor coverage and lower mobilities which can be improved with multiple coats, however, casting multiple coats has the undesirable effect of increasing the leakage current, leading to lower on/off ratios. Thus, we find that single layers are preferable to

multiple layers for FET fabrication. Interestingly, FETs prepared from the smoother CdS films using CdTDT annealed at 160 °C in the presence of sulfur show weakly p-type behavior (**Figure 4.8b**).

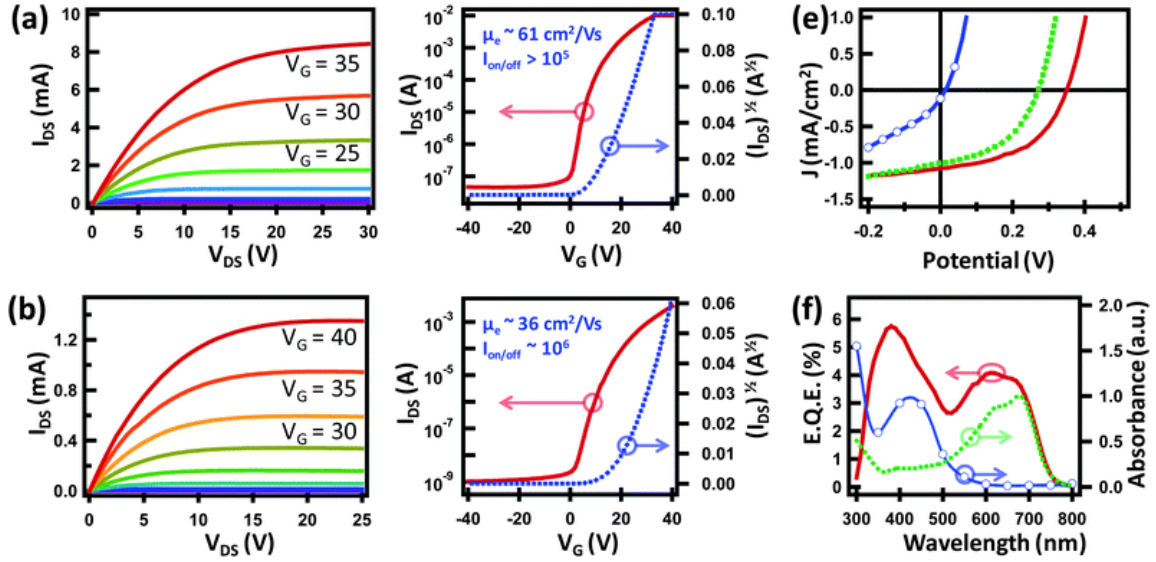

Figure 4. 9. FET and solar cell device characteristics. (a) and (b) Output curves for CdS devices prepared from CdTNT and CdTDT, respectively. (c) and (d) Transfer curves for CdS devices prepared from CdTNT and CdTDT, respectively. (e) *J–V* characteristics of ITO/PTB7/MoO_3/Au (blue trace with circles) ITO/CdS/PTB7/MoO_3/Au (dotted green trace) and ITO/ZnO/CdS/PTB7/MoO_3/Au (red trace) devices. (f) External quantum efficiency of ITO/ZnO/CdS/PTB7/MoO_3/Au device (red trace) compared to the absorption spectra of the CdS film (dotted green trace) and PTB7(blue trace with circles).

A brief investigation of film and device stability was carried out. CdS films were prepared from CdTNT as usual following the optimized procedure described in the main text and stored in air for 1 week, followed by annealing in nitrogen and electrode evaporation. These devices exhibited mobilities of 35 cm^2/Vs, similar to control devices. Devices were aged in a glovebox (with O_2 content <20 ppm) for 1 week. A small decrease in current and mobility was observed from 30 cm2/Vs (pristine) to 18 cm^2/Vs (week old). After annealing at 300 °C for 20 min in nitrogen, the performance was largely recovered and the devices exhibited a mobility of 34 cm^2/Vs; slightly higher than the original mobility, though the overall current was slightly lower and the threshold voltage increased from 8 V to 14 V. These curves are plotted in **Figure 4.10a**. To investigate the air stability of the finished FETs, completed devices were also aged in air for 1 week, then brought into a nitrogen filled glovebox and annealed at 300 °C for 20 min. The overall change was very similar to that observed for the devices aged in nitrogen, where the currents decreased slightly and the threshold voltage increased slightly. The original mobility was 45 cm^2/Vs and the mobility after aging in air for 1 week and annealing in nitrogen was 41 cm^2/Vs. These curves are plotted in **Figure 4.10b**.

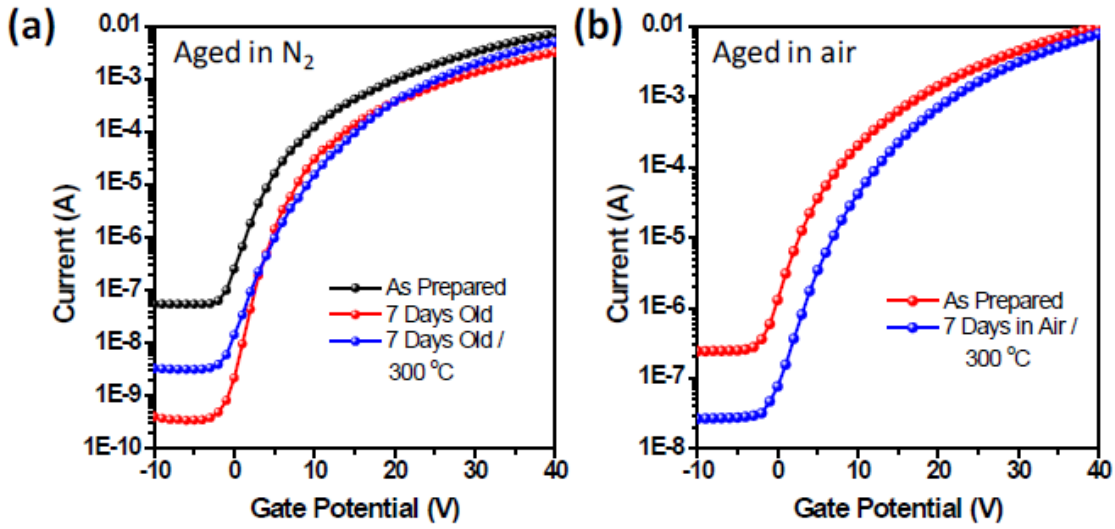

Figure 4. 10. Transfer curve of CdS devices. a) Comparison of pristine CdTNT based devices after storing in nitrogen for 1 week and subsequently annealing. b) Comparison of pristine CdTNT based devices after storing in air for 1 week and annealing.

In order to evaluate the applicability of the CdS films to other device types, hybrid solar cells were prepared using the CdS films as electron accepting layers in combination with the conjugated polymer poly[[4,8-bis[(2-ethylhexyl)oxy]benzo[1,2-b:4,5-b′]dithiophene-2,6-diyl][3-fluoro-2-[(2-ethylhexyl)carbonyl]thieno[3,4]thiophenediyl]] (PTB7).[91] Devices were prepared using the architecture ITO/CdS/PTB7/MoO_3/Au and compared to devices without any CdS layer (ITO/PTB7/MoO_3/Au) as well as devices with a ZnO layer[92] (ITO/ZnO/CdS/PTB7/MoO_3/Au). Current density–voltage (J–V) characteristics are reported in **Figure 4.9e** while the external quantum efficiency (EQE) of the ITO/ZnO/CdS/PTB7/MoO3/Au device is reported in **Figure 4.9f**, along with the absorption spectra of the CdS and PTB7 layers. The short-circuit current (J_{SC}) in the device is found to increase dramatically from 0.12 to 0.92 mA cm^{-2} upon insertion of the CdS layer while the open circuit voltage (V_{OC}) increases from 0.014 V to 0.228 V. The V_{OC} of the device can be further improved to 0.350 V by incorporating a ZnO layer between the ITO and CdS layers, yielding a device which produces a JSC of 1.07 mA cm^{-2}, a fill factor of 49% and a power conversion efficiency of 0.2%. The device including a ZnO layer without CdS was found to produce very little photocurrent (J_{SC} ~ 0.01 mA cm^{-2}). The EQE produced by the ITO/ZnO/CdS/PTB7/MoO_3/Au architecture shows significant photocurrent from both the CdS layer (which absorbs strongly in the 300 to 500 nm region) and the PTB7 layer (which absorbs strongly in the 550 to 700 nm region), demonstrating the ability of the CdS to function as both an electron accepting and hole donating material.

4.4 Conclusion

In conclusion, we demonstrate a convenient route to obtain CdS films having good electron mobilities by spin-coating and thermally annealing cadmium thiolate molecules. Although the annealing temperature is somewhat higher than typical for organic semiconductors, the processing procedure is otherwise quite similar to procedures used to prepare organic FETs. The synthetic procedure, however, is considerably simpler than procedures used for typical organic semiconductors (such as Suzuki or Stille couplings) and does not involve the intermediary synthesis of nanoparticles; the thiolate is prepared by simply stirring CdO with an alkyl thiol and can be subsequently processed like an organic semiconductor. We envision that CdS films prepared in this way may be applicable to a wider range of semiconducting devices, including hybrid organic/inorganic devices. Future work will explore the applicability of this technique to other chalcogenide semiconductors and the identification of thiolates which decompose at lower temperatures.

CHAPTER 5. Environmentally-Benign, Non-Polar Inks for Solution-Processed Chalcopyrite Solar Cells

The content of this chapter is published in *Scientific Reports* **6**, 36608 (2016)

5.1 Research background

Since their discovery, solar cells have been recognized as an appealing energy source due to the abundance of solar energy, their simplicity and lack of moving parts and their ability to generate power in remote locations. Although the practical use of solar modules in the past has been confined to niche applications (where their high cost could be justified), the aggregate amount of energy produced by solar modules has increased by more than one thousand times over the past 20 years and power generation from photovoltaics now constitutes approximately 1% of global electrical energy production.[93] As other energy sources become increasingly scarce and the burning of fossil fuels is curbed to mitigate climate change[94], the impetus to produce energy from sunlight continues to grow stronger every year. The large scale production of solar energy requires the deployment of solar cells over large surface areas, which is economically problematic due to the relatively high cost per area to manufacture photovoltaic modules. Thus, finding low-cost materials and strategies to fabricate solar cells constitutes an immensely important scientific challenge facing our generation.

Recent years have witnessed the development many new types of solar technologies which can be deposited like inks by low cost solution coating techniques including organic bulk heterojunction (BHJ) solar cells[95], dye-sensitized solar cells (DSSC)[96], colloidal quantum dot (CQD) solar cells[97] and perovskite solar cells[42]. Although the power conversion efficiencies (PCEs) of these technologies have developed rapidly to approach those of their inorganic counterparts, their stabilities and reliabilities remain unresolved.

Another route to accomplish the same goals as BHJ, DSSC, CQD and perovskite approaches is to develop strategies to prepare more traditional inorganic solar cells by solution processing methods. $CuInS_2$[98] and related $Cu(In,Ga)Se_2$ materials have been shown to yield PCEs of over 20%[99-100] , as high as any solar cell based on BHJ, DSSC, CQD or perovskite materials, while the long-term stability of these modules has already been established. Although these chalcogenide materials are generally insoluble, it has been demonstrated that using appropriate chemistry, soluble precursor compounds can be prepared and processed like inks[79, 101]. For instance, Mitzi and co-workers have shown that $Cu(In,Ga)Se_2$ cells can be fabricated by processing films from solutions of hydrazinium metal selenides (using hydrazine as a solvent) followed by thermal annealing and selenization of the precursor films[102].

Although this has proven to be an effective method to prepare $Cu(In,Ga)Se_2$ type solar cells, hydrazine is a toxic, corrosive and chemically reactive solvent. Alternatively, $Cu(In,Ga)Se_2$ nanoparticles (NPs) can be synthesized and deposited by solution processing[103-105]. However, these NP based devices typically lead to low PCEs without a subsequent high temperature selenization step.

The ultimate goal of researching solution-processed solar cells is to enable the manufacture solar cells on a large scale using industrial printing equipment. In the context of large-scale printing operations, inks based on non-toxic and non-polar solvents offer the best performance due to their low reactivity, low surface tension, good wettability, evaporation rates and ability to form smooth and uniform films. Thus, the ability to process solar cells using non-toxic, non-polar solvents offers the best compatibility with industrial-scale printing equipment.

There are few examples of $CuInS_2$ or $Cu(In,Ga)Se_2$ solar cells being deposited from precursors using common organic solvents[106-110]. Until now, these works have utilized metal xanthate precursors which must be prepared using carbon disulfide, which poses health and reactivity problems like hydrazine. Metal xanthates additionally possess undesirable reactivity; they are very sensitive to pH and yield an ill-defined a mixture of reactive products when they decompose. Other works[111-112] have utilized mixtures of metal halides and thiourea instead of single molecule precursors, however, it is unclear what happens to the halide anions or thiourea decomposition products after the metal sulfides are formed. Thus, molecular precursors which decompose by a well-defined reaction to yield well-defined products have until now not been demonstrated.

In this contribution, we have used a rational, organo-chemical approach to design metal complexes which are soluble in non-toxic, non-polar solvents and decompose thermally to yield pure metal sulfide films. The t-butoxy carbonyl (TBOC) group was used as a model and starting point in the design of these complexes; the TBOC moiety is well-known to decompose quantitatively via SN_1 or E_1 mechanisms at elevated temperatures to yield volatile iso-butene and CO_2 byproducts.[113] The thermally-labile TBOC moiety has been successfully exploited as a solubilizing group to solution-process organic semiconductor films which become crystalline and insoluble after heating, allowing high-mobility, multilayer films to be processed[114-116]. In this work, we have extended this concept to solution-process insoluble, inorganic metal sulfide films. We show that tertiary-alkyl metal thiolates (TAMTs) decompose analogously to the TBOC group to yield volatile alkyl sulfides and insoluble metal sulfide films which are free from organic residue.

We show that $CuInS_2$ and $Cu(In,Ga)S_2$ films can be readily prepared by annealing TAMT films which are deposited from solutions in common organic solvents, as illustrated in **Figure 5.1**.

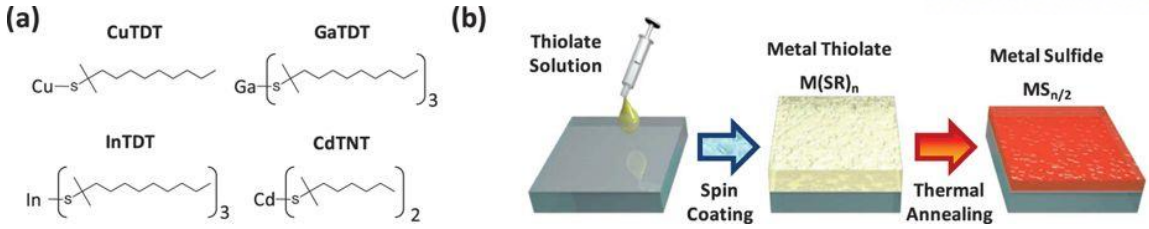

Figure 5. 1. Schematic diagrams including (a) TAMT precursor molecules used to prepare sulfide films and (b) processing strategy.

Films with a range of compositions can be prepared by adjusting the ratio of each TAMT (Cu, In, and Ga) in order to achieve a range of band gaps and allowing detailed control of the energy band structure. These films can be deposited on conductive transparent indium tin oxide (ITO) substrates, with appropriate electrodes, in order to produce photovoltaic devices (**Figure 5.2**). By grading the bandgap of the active layer, it is possible to create a band structure which drives photoexcited electrons from the absorbing layer to the p-n junction.

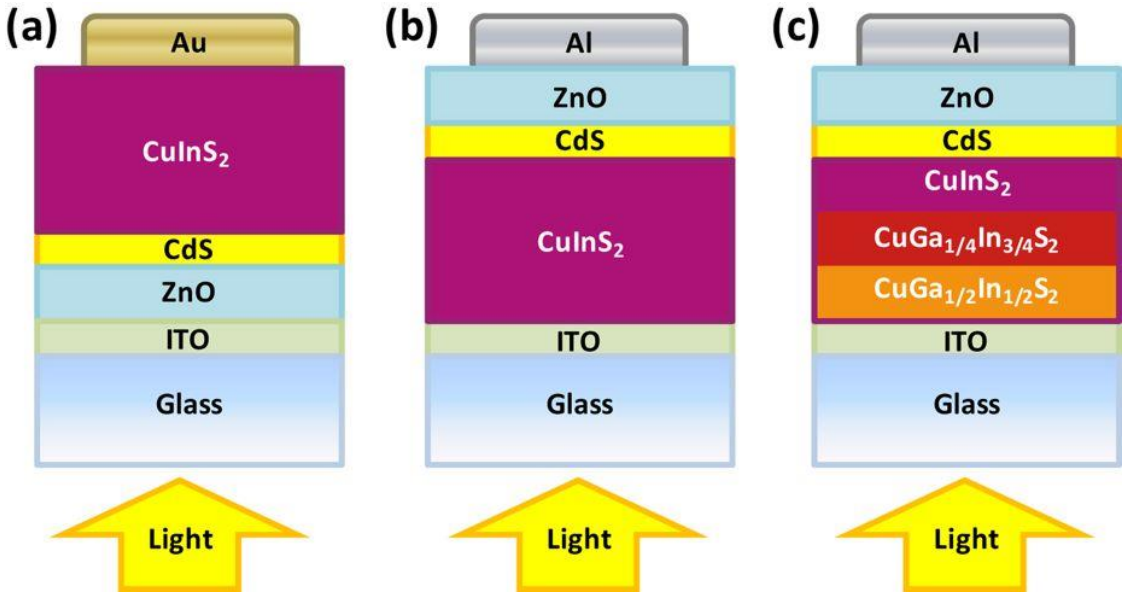

Figure 5. 2. Schematic diagrams of architectures used for (a) n-type substrates, (b) p-type substrates and (c) p-type substrates using an active layer with a graded band-gap.

This report marks the first of its kind to utilize rationally designed $CuInS_2$ precursors which thermally decompose via a well-understood reaction. The complexes yield volatile by-products with low reactivity (dialkyl sulfides) and metal sulfide films which are free of organic residue. The simple reagents used, coupled with the straightforward synthesis and processing of the materials make this approach well-suited for large scale solar cell production.

5.2 Experimental details

Material Synthesis

Copper t-dodecanethiolate (CuTDT): Copper (II) acetate monohydrate (1.00 g, 5.00 mmol) was dissolved in a mixture of 12 mL ethanol and 12 mL water yielding a deep blue solution. A small amount of solid did not dissolve. t-dodecanethiol (2.78 mL, 11.8 mmol) was separately dissolved in 8 mL of ethanol. The two solutions were combined in a large vial and shaken for 15 minutes, during which time the liquid phase changed from blue to green to hazy yellow, indicating a reduction of Cu (II) to Cu (I), while the remaining copper acetate dissolved. The mixture was centrifuged at 2000 rpm for 5 minutes and a thick oily phase separated to the bottom. The supernatant liquid was discarded and the oily phase was washed several times with anhydrous methanol. The viscous material was transferred to a Schlenk flask and dried under vacuum overnight.

Indium t-dodecanethiolate (InTDT): In a nitrogen-filled glovebox, indium isopropoxide (0.584 g, 2.0 mmol) was weighed into a 10 mL vial and dissolved in 4 mL of anhydrous THF. T-dodecanethiol (1.55 mL, 6.6 mmol) was added to the solution and shaken vigorously. The mixture was allowed to stand at room temperature for 2 hr. before being filtered through a 0.45 micron PTFE syringe filter into a Schlenk flask. The solvent and excess thiol were removed under vacuum and the resulting viscous clear material was dried under vacuum overnight.

Gallium t-dodecanethiolate (GaTDT): The same procedure as used for InTDT was used, with the exception that gallium isopropoxide (0.494 g, 2.0 mmol) was used instead in place of indium isopropoxide.

Cadmium t-nonanethiolate (CdTNT): was prepared from cadmium acetate and t-nonanethiol following the procedure in **Chapter 4.2**.

Film Processing

Unless otherwise noted, films were prepared by dissolving metal TAMTs in THF at a concentration of 100 mg/mL, filtering the solution through a 0.45 μm PTFE filter and spin casting at 1500 rpm. Films were then annealed on digital hotplates, in a nitrogen filed glovebox at temperatures in the range of 200–400 ℃ for 10 minutes to facilitate conversion of the TAMTs to sulfide films.

Film characterization

TGA traces of each sample were collected using a TGA instrument, Q500. To collect each trace, ~20 mg samples were put in aluminium pans and the temperature was raised from 25 to 450 ℃ at 5 ℃/min. XRD patterns were collected using an X-ray diffractometer D/MAX2500V/PC (Rigaku, Japan). Powder samples for TGA and XRD were prepared through annealing of TAMT complexes at 300 ˚C in a vial under vacuum. Gas chromatography-mass spectrometry (GC-MS) spectra were

gathered using Bruker 450-GC & 320-MS. For the measurement, samples were prepared as described in the main text. UV-vis spectrometry was performed using a Varian Carry 5000 spectrophotometer in the range 300 to 1200 nm with 1 nm resolution. AFM images were collected using a Veeco Multimode microscope with 300 kHz silicon tips operating in tapping mode. SEM images were gathered using NanoSEM 230, FEI. For Raman measurements, sample was prepared by heating an equimolar mixture of Cu and In thiolates to 300 °C under vacuum and collecting the volatile byproducts using a liquid nitrogen trap and dissolving this material in chloroform. Raman spectra were additionally collected for $CuInS_2$ film samples prepared as described in the text. Raman spectra were measured using 532 nm excitation wavelength with a WITec alpha300R confocal Raman microscope. Laser beam power was 1 mW and the collected spectra were integrated 10 times.

UPS/XPS Measurements

50 nm thick gold films were deposited on pre-cleaned Si substrates with a thin native oxide. Solutions were spin cast onto the gold films using the same procedures used to fabricate devices, as described in the text and device fabrication sections. UPS and XPS experiments were carried out using a Thermo Fisher Scientific ESCALAB 250XI which was maintained at a base pressure of 1.0×10^{-9} Torr. UPS measurements were carried out using a He I ($h\nu = 21.2$ eV) source while XPS measurements were performed using a monochromated Al-Kα X-ray source. UPS and XPS spectra were collected for films annealed at both 300 and 400 ℃, but did not show significant differences.

Device fabrication and testing

Glass/ITO substrates were cleaned with detergent, then ultra-sonicated in acetone and isopropanol and subsequently dried in an oven overnight at 100 ℃. Metal sulfide films were processed from solutions of each TAMT in THF as described above. In the case of CdS, a solution of CdTNT in chloroform (6 mg/mL) was used. ZnO films were deposited by diluting 200 µL of a solution of diethyl zinc in toluene (Aldrich, 15 wt%) with 400 µL of anhydrous THF, filtering the diluted solution through a 0.45 um PTFE filter and spin coating this solution in air at 3000 rpm, followed by annealing in air at 110 ℃ for 10 min. Completed devices were pumped down in vacuum ($<10^{-6}$ torr; 1 torr ~133 Pa), and 100 nm thick Al electrodes or 80 nm thick Au electrodes were deposited on top of the active layer by thermal evaporation. *J-V* measurements were carried out using a Keithley 2635A source measurement unit with the solar cells inside a nitrogen filled glove box using a high quality optical fiber to guide the light from a Xenon arc lamp to the devices. An aperture with an area of 13 mm^2 defined the active area of the devices. The *J-V* were measured under AM 1.5G illumination at 100 $mWcm^{-2}$ calibrated with a Si photodiode (PV Measurements, Inc.) which was standardized at the National Renewable Energy Laboratory in Golden, Colorado (US). Reported *J-V* curves represent the best devices for each condition

tested. EQE measurements were conducted in ambient air using an EQE system (Model QEX7) by PV measurements Inc. (Boulder, Colorado). Spectral mismatch factors between the simulator and AM1.5G spectrum were found to be 10% or less.

5.3 Results and discussion

The TAMT materials were conveniently synthesized by reacting metal alkoxides or acetates with tertiary alkane thiols as shown in **Figure 5.3**.

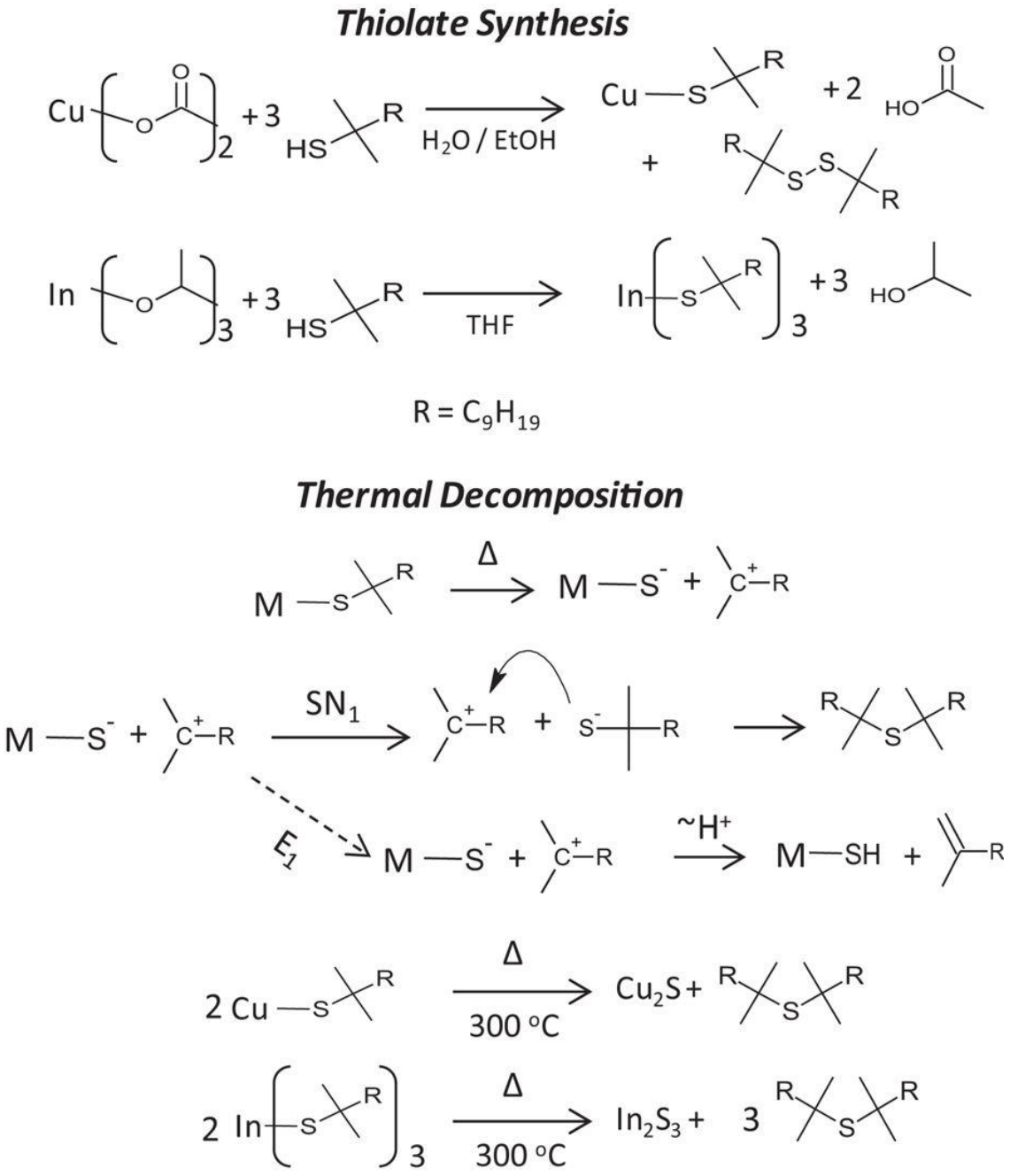

Figure 5. 3. Synthesis of metal thiolates and their thermal decomposition to metal sulfides.

In the case of copper t-dodecanethiolate (CuTDT), Cu(II) acetate reacted with 2 equivalents of t-dodecanethiol, undergoing a reduction/oxidation reaction with simultaneous anion displacement to afford the Cu(I) thiolate, with acetic acid and t-dodecyl disulfide as byproducts. Ga and In isopropoxides

were found to readily react with t-dodecanethiol; isopropoxide is a strong base which is quickly neutralized by proton transfer from t-dodecanethiol (a weak acid) to yield Ga and In t-dodecanethiolates (GaTDT and InTDT) and isopropanol. The isolated TAMTs were found to be insoluble in polar solvents including water and methanol, but exhibited excellent solubility in non-polar solvents and solvents with intermediate polarity including hexane, toluene, chloroform and tetrahydrofuran (THF). The TAMTs were found to be stable for months at room temperature in the absence of light, but decomposed rapidly to metal sulfides upon heating to moderate temperatures.

In order to quantify the thermal decomposition of the precursors into metal sulfides, thermogravimetric analysis (TGA) was performed. **Figure 5.4** shows TGA traces of each thiolate complex as well as a 1:1 molar mixture of CuTDT and InTDT. CuTDT begins to decompose at 160.4 ℃ (95.7% of original weight) and rapidly loses mass to 32.4% of its original weight during an increase of 9.1 ℃. InTDT decomposes to 27.1% of its original weight in the range of 121.9 ℃ to 133 ℃, while GaTDT steadily decomposes to 17.3% of its original weight starting at 78.7 ℃ and ending at 129.4 ℃ (a range of 50.7 °C).

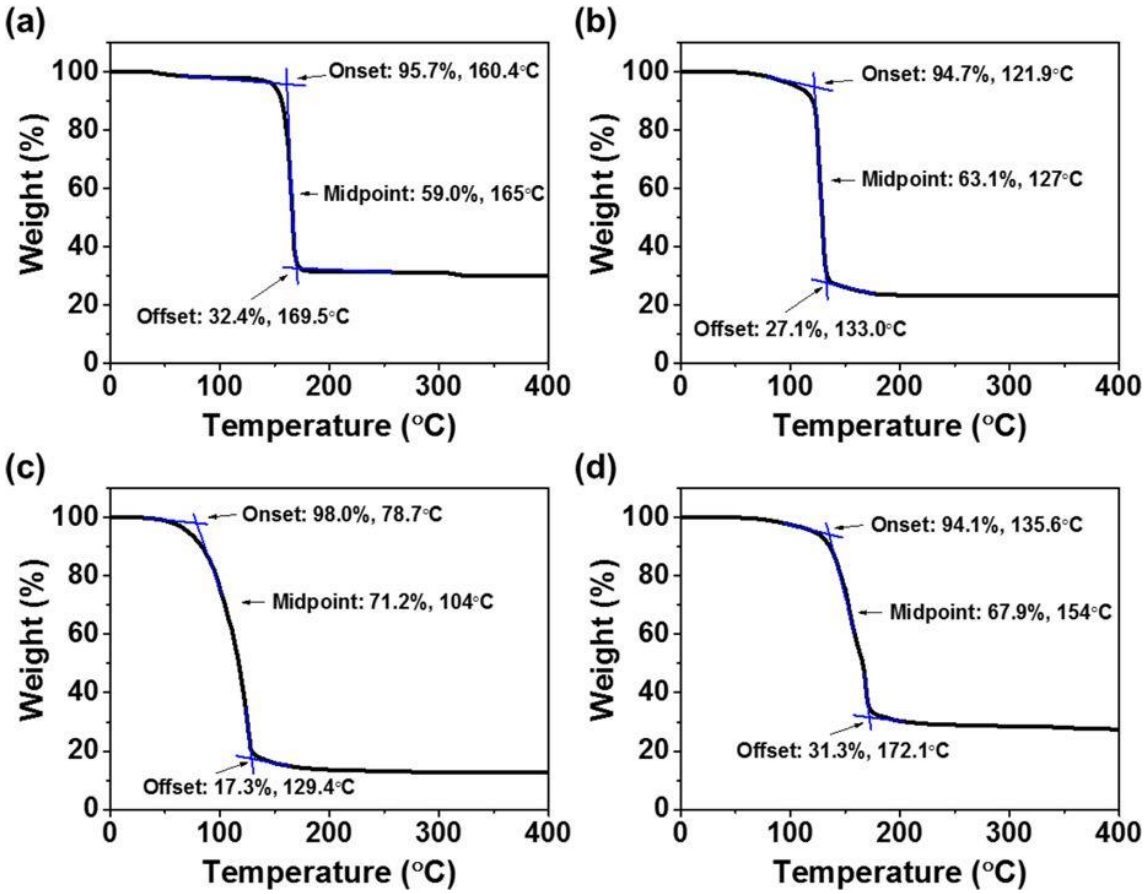

Figure 5. 4. TGA plots of (a) CuTDT, (b) InTDT, (c) GaTDT, and (d) a CuTDT and InTDT 1:1 molar mixture, respectively.

The 1:1 molar mixture of CuTDT and InTDT converts to the metal sulfide phase somewhat more gradually over a range of 46.5 ℃, losing 62.8% of its weight without showing two distinct decomposition steps. The losses in mass are consistent with the thermal decomposition mechanisms outlined in **Figure 5.3**. Although all materials decompose to metal sulfides below 200 ℃, TAMT films were processed at a reference temperature of 300 ℃ throughout this study to ensure complete conversion of the insulating precursors to semiconducting sulfide films. For some experiments, higher annealing temperatures were used as noted in order to achieve better film crystallinity.

In order to confirm the decomposition mechanism and identity of the reaction by-products, we decomposed samples of the complexes by heating to 300 ℃ under vacuum and trapped the volatile decomposition products with a liquid nitrogen trap. The decomposition products were dissolved in chloroform and analyzed by gas chromatography -mass spectrometry (MS, **Figure 5.5**) and Raman spectrometry (**Figure 5.6**).

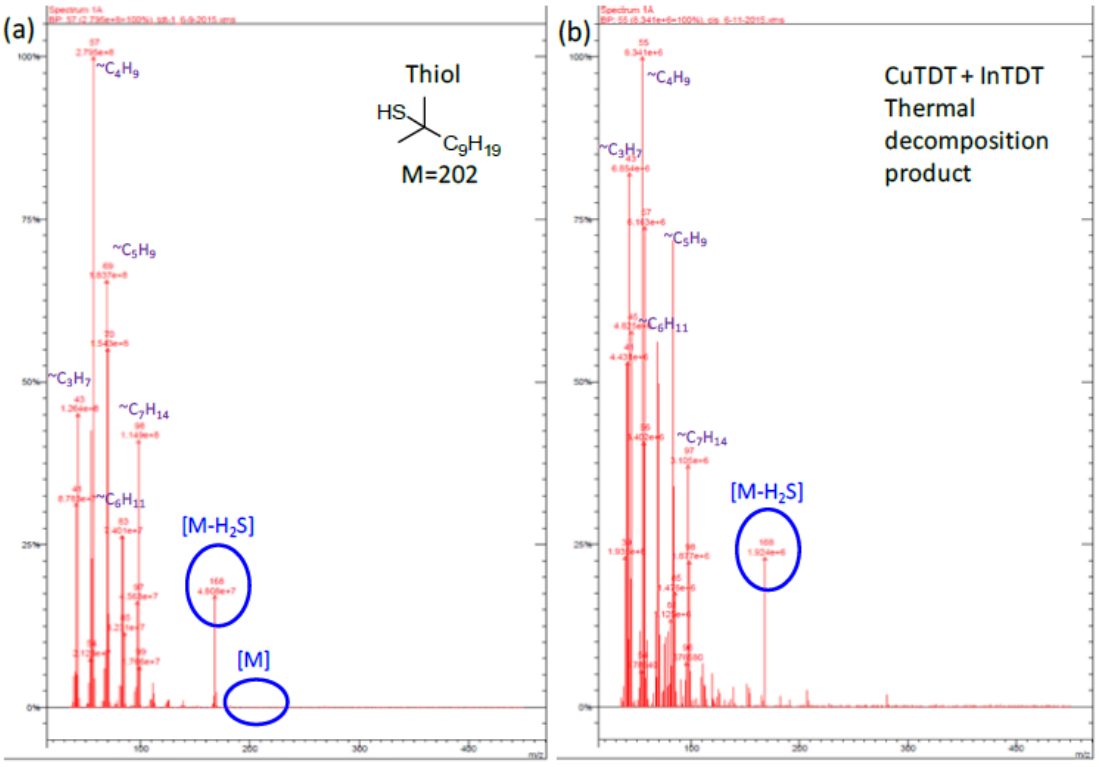

Figure 5. 5. Mass spectra of (a) t-dodecanethiol reference and (b) the volatile decomposition products obtained upon heating a 1:1 molar ratio of CuTDT and InTDT to 300 ℃

A control sample consisting of the thiol starting material was analyzed as a reference, however, no peak corresponding to the MW of the parent thiol (M = 202) was observed in the MS spectrum and the largest MW observed in the thiol spectrum (M = 168) corresponded to the MW of the thiol – H_2S, i.e. the alkene, indicating that the C-S bond of the thiol was completely fragmented during ionization in the

MS instrument. This is consistent with reference MS spectra of t-dodecanthiol (2-methyl-2-undecanethiol) which show no peak at M = 202 corresponding the un-fragmented compound.[117] The decomposition products obtained by heating a mixture of CuTDT and InTDT also showed a highest MW of 168 with spectra which closely resembled the parent thiol. The MS results thus did not distinguish between alkylthiol, alkene or dialkyl sulfide, due to the ease with which the C-S bond is cleaved in the MS instrument, however, were consistent with the presence of any one of these compounds.

Raman spectra of the decomposition products (**Figure 5.6**) clearly showed that no alkene or thiol were present, but showed strong peaks corresponding to C-S vibrations, indicating that the volatile decomposition product consists chiefly of the dialkyl sulfide.

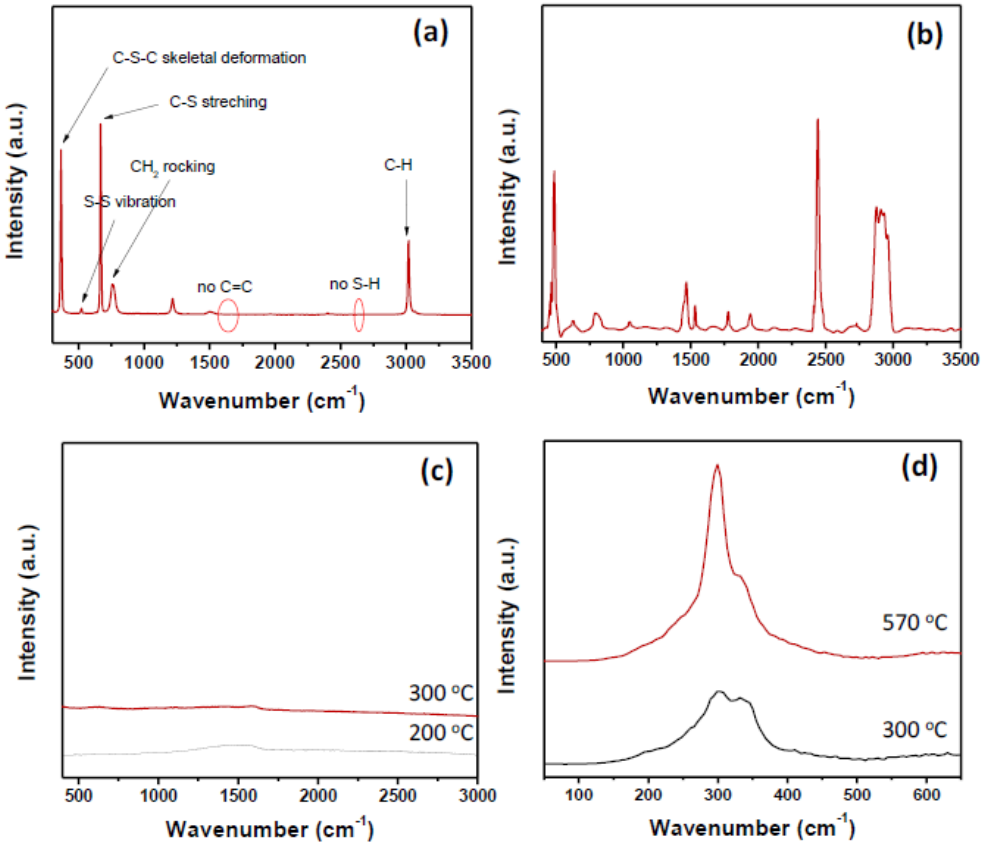

Figure 5. 6. Raman spectra taken from (a) $CuInS_2$ volatile decomposition products dissolved in chloroform, (b) TAMT precursor in chloroform, (c) $CuInS_2$ films processed from TAMTs after annealing at 200 and 300 °C, and (d) Comparison of A_1 vibrational mode of films processed at 300 °C, before and after sintering in a vacuum tube furnace at 570 °C.

This strongly suggests that the decomposition of the TAMT occurs primarily via an SN_1 mechanism as shown in **Figure 5.3**. Although we initially anticipated that the thiolates decomposed via an E_1 mechanism, (dashed arrow, **Figure 5.3**) the SN_1 route is not unexpected given the presence of the

thiolate anions in the films, which are known to be exceptionally strong nucleophiles and apparently react with the carbocation intermediate before proton transfer and elimination of the alkene can occur. The rapid, thermally activated decomposition at lower temperatures than primary or secondary thiolates[88] is also consistent with E_1 or SN_1 processes and further substantiate the decomposition mechanism.

Raman spectra of $CuInS_2$ films prepared by spin coating an equimolar ratio of CuTDT and InTDT and annealing at 200 ℃ and 300 ℃ are also shown in **Figure 5.6**. The spectra of films annealed at 200 or 300 ℃ show no bands in the range of 600–1200 cm^{-1}corresponding to C-S, C-S-C or CH_2 vibrational modes and no sharp peaks in the range of 2400–3000 cm^{-1} corresponding to S-H or C-H vibrations, (**Table 5.1**) indicating that no detectable amounts of organic residue were present after annealing at either 200 or 300 ℃. A plot of the un-annealed precursor is included for reference showing strong C-H stretching signals at ~2800 to 3000 cm^{-1} and several other sharp peaks in the range of 400 to 2500 cm^{-1} which disappear after annealing films at 200 ℃ or more. These results are consistent with the TGA measurements; upon heating the TAMTs, the mass decreases in the range of 120–170 ℃ and reaches a constant value, indicating that the organic constituents have completely volatilized and no organic residue is left at 200 ℃.

Table 5. 1 Raman vibrational mode assignment for 1-Dodecanethiol.[118]

Mode assignment	Wavenumber (cm^{-1})
$\nu(C\text{-}S)_G$	659
$\nu(C\text{-}S)_T$	735
$\nu(C\text{-}C)_T$	1061-1281
$\nu(C\text{-}C)_G$	1083
$\nu_s(CH_2)$	2848-2857
$\nu_s(CH_3)$	2873
$\nu_a(CH_2)$	2882-2891

The presence of $CuInS_2$ was confirmed by examining the region of the Raman spectrum near 300 cm^{-1} (**Figure 5.6**). Phase-pure $CuInS_2$ with the tetragonal chalcopyrite structure exhibits a Raman spectrum dominated by a sharp A_1 signal at 290–292 cm^{-1}.[119-120] A very broad peak at 298 cm^{-1} with a strong shoulder was observed for films annealed at 300 ℃, consistent with the presence of disordered $CuInS_2$. Upon annealing at a higher temperature of 570 ℃ (just below the softening temperature of the

glass substrate), the Raman spectrum becomes much sharper while the relative intensity of the shoulder decreases, indicating that the tetragonal chalcopyrite phase crystallizes and that the crystal quality improves upon annealing at higher temperature. However, it is apparent that the crystallinity of films post-annealed in this way is still inferior to films which are epitaxially grown or sulfurized at high temperatures.

UV-vis absorption spectra of Cu_2S, In_2S_3, and different compositions of $Cu(In,Ga)S_2$ are shown in **Figure 5.7**, while the optical properties are summarized in **Table 5.2**. Cu_2S absorbs light up to 1020 nm optical energy gap (E_g (opt) = 1.22 eV), whereas In_2S_3 exhibits an absorption onset at 550 nm. (E_g (opt) = 2.25 eV). $CuInS_2$ films were prepared by spin coating a mixed TAMT solution with 1:1 molar ratio, the $CuInS_2$ absorption spectra exhibit a clear absorption onset which is distinct from either Cu_2S or In_2S_3. This implies that a distinct $CuInS_2$ phase is formed, as opposed to a mixture of Cu_2S and In_2S phases.

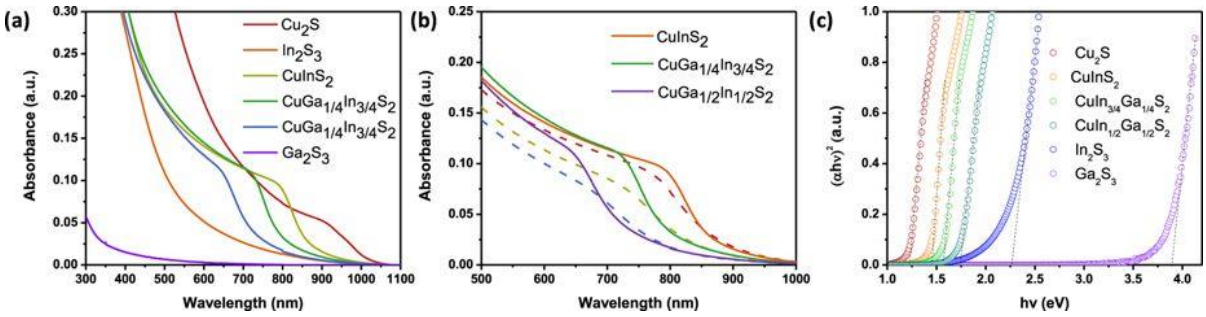

Figure 5. 7. (a) Spectra of all materials annealed at 400 ℃. (b) Zoomed plot of the 500-1000 nm spectral region showing absorption onsets for $Cu(In,Ga)S_2$ materials annealed at 300 (dashed traces) or 400 ℃ (solid lines) (c) Tauc plots showing $(\alpha h\nu)^2$ vs $h\nu$ (for direct optical transitions).

Table 5. 2. Absorption onsets, optical band gaps and band energies of sulfide films.

Materials	λ_{onset} (nm)	E_g(opt) (eV)	E_{VB} (eV)	ϕ (eV)	E_{CB} (eV)
Cu_2S	1020	1.22	4.9	4.9	3.7
In_2S_3	550	2.25	6.4	4.9	4.1
Ga_2S_3	380	3.26	7.4	4.9	4.1
$CuInS_2$	860	1.44	5.4	4.9	4.0
$Cu(In,Ga)S_2$ [In:Ga = 3:1]	800	1.55	5.4	4.9	3.9
$Cu(In,Ga)S_2$ [In:Ga = 2:2]	720	1.72	5.4	4.9	3.8

The presence of a distinct $CuInS_2$ phase after annealing at 400 ℃ and 570 ℃ was confirmed by X-ray diffraction (XRD) (**Figure 5.8**). Diffraction patterns of films annealed at both temperatures fit the tetragonal chalcopyrite phase, however, the diffraction peaks become much narrower at higher temperature. The full width at half maximum of the 112 plane decreased from 3.22 to 1.26 ° upon annealing at 400 and 570 ℃, respectively, indicating that relatively amorphous $CuInS_2$ material initially formed by the decomposition of the thiolates is able to crystallize in the tetragonal chalcopyrite phase when heated sufficiently, consistent with the trends observed in Raman spectra. Films annealed at 200 ℃ or 300 ℃ did not exhibit any significant diffraction pattern, indicating an amorphous structure and low crystallinity in films annealed at lower temperatures.

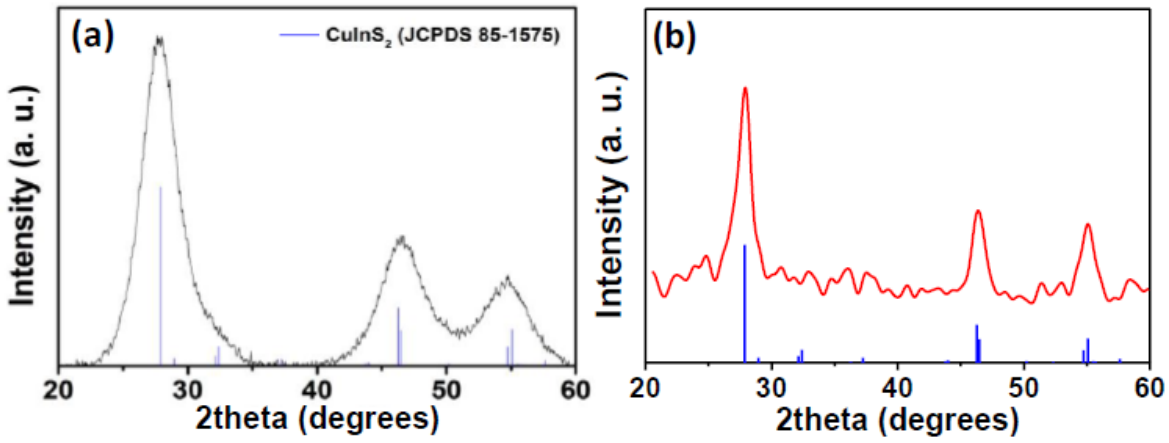

Figure 5. 8. X-ray diffraction patterns of $CuInS_2$ materials. (a) Powder annealed at 400 ℃. (b) Thin film annealed at 570 ℃ under a stream of argon.

As expected, were able to tune the optical bandgap of $CuInS_2$ by adding GaTDT to mixed CuTDT/InTDT solutions. This process leads to a widening of E_g in the $Cu(In,Ga)S_2$ films, as Ga atoms replace In atoms in the structure. A 3:1 molar ratio of In:Ga in $Cu(In,Ga)S_2$ film exhibits a blue-shifted absorption onset by 60 nm, while a 140 nm blue-shift is observed in the film with 1:1 molar ratio of In:Ga. In contrast, pristine Ga_2S_3 films show virtually no absorption of visible light due to the wide bandgap of Ga_2S_3 (3.26 eV). **Figure 5.7b** shows the effect of annealing temperature on the absorption spectra of $Cu(In,Ga)S_2$ films. As we confirmed in TGA, TAMTs could be converted to metal sulfides below 200 ℃. However, films were annealed at 300 or 400 ℃ to encourage crystallization and to obtain suitable absorption data; it is clear that films annealed at 400 ℃ show sharper absorption onsets and higher optical density than films annealed at 300 ℃. For comparison, absorption data were plotted as Tauc plots of $(\alpha h\nu)^{1/2}$ vs $h\nu$ (**Figure 5.9**) and $(\alpha h\nu)^2$ vs $h\nu$ (**Figure 5.7c**) to model indirect and direct optical transitions, respectively. The plots of $(\alpha h\nu)^{1/2}$ vs $h\nu$ indicate similar E_g values as obtained by

fitting absorption onsets. The $(\alpha hv)^2$ plots showed good fits as well, except for In_2S_3, which has been shown to have both direct and indirect optical transitions, causing an indistinct absorption onset which is consistent with previous observations.[121-122]

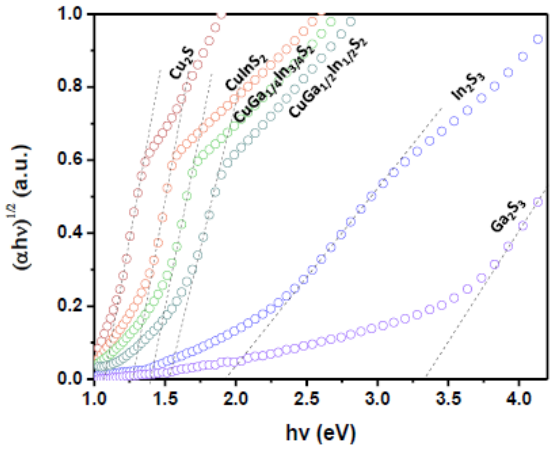

Figure 5. 9. Tauc plots ($(\alpha hv)^{1/2}$ vs hv) for indirect transition of various chalcogenide films annealed at 400 °C

The surface morphology of each film was characterized by atomic force microscopy (AFM). AFM images of Cu_2S, In_2S_3, and $CuInS_2$ are shown in **Figure 5.10**. All films show smooth surfaces with RMS roughness values of 1.1 nm or less.

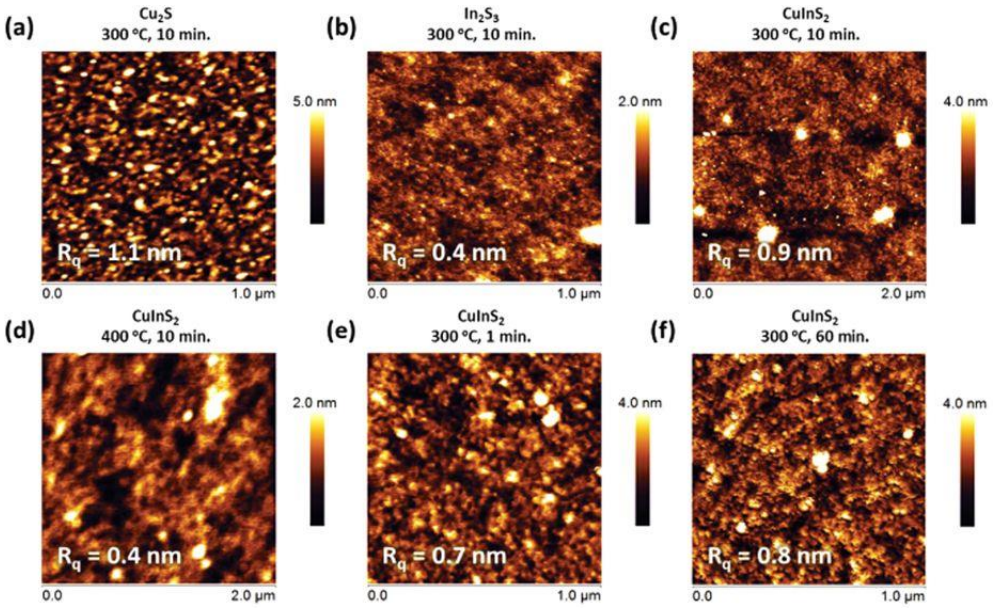

Figure 5. 10. AFM images showing (a) Cu_2S, (b) In_2S_3 and (c) $CuInS_2$ films prepared by annealing the corresponding metal thiolates at 300 °C for 10 minutes. Image (d) shows a $CuInS_2$ film annealed at a higher temperature of 400 °C while images (e) and (f) show films annealed at 300 °C for 1 and 60 minutes, respectively.

Figure 5.10a-c shows the surface morphology of Cu_2S, In_2S_3, and $CuInS_2$, respectively, processed at 300 ℃ for 10 min. Cu_2S exhibits a rougher and irregular morphology compared to In_2S_3 and $CuInS_2$ films, with RMS roughnesses of 1.1, 0.4 and 0.9 nm, respectively. $CuInS_2$ shows intermediate surface features compared to Cu_2S and In_2S_3. In the case of $CuInS_2$ annealed at 400 ℃, (**Figure 5.10d**), the horizontal size of the surface features becomes larger than films annealed at 300 ℃, however, the surface morphology becomes smoother. **Figure 5.10c,e,f** compare how varying the annealing time from 1 to 60 minutes affects morphology. These images suggest that annealing time does not greatly affect to the surface morphology of the films. To confirm the surface morphology of the $CuInS_2$ films, scanning electron micrograph (SEM) images were taken of the surface.

SEM images were collected for cross-sections of $CuInS_2$ films and $CuInS_2$/CdS/ZnO trilayer films prepared on glass/ITO substrates were collected as well. These images are shown in **Figure 5.11**. It can be seen that films are smooth and continuous, and that the $CuInS_2$ films are approximately 80 to 100 nm thick.

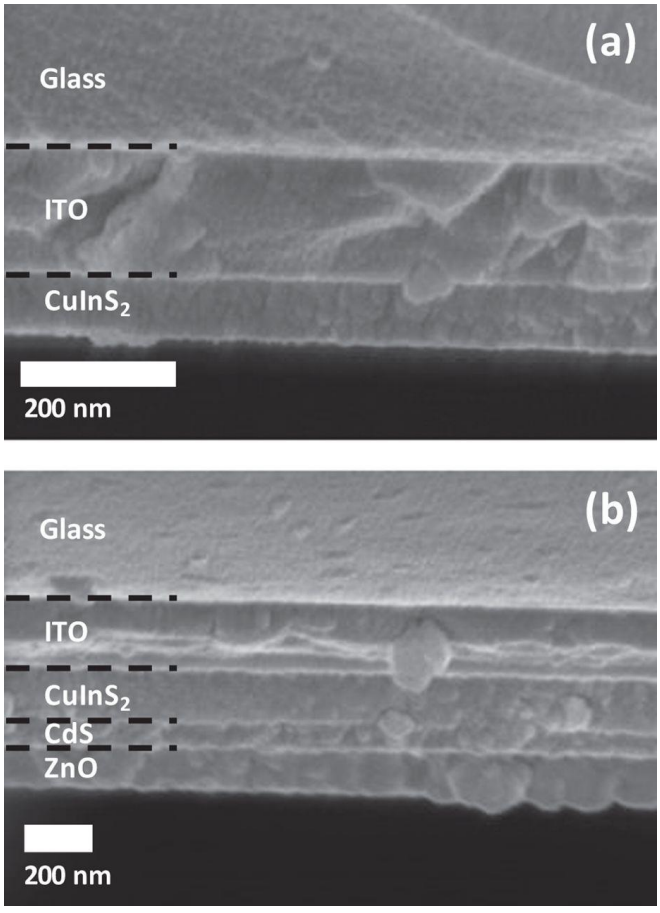

Figure 5. 11. SEM images showing (a) a $CuInS_2$ film deposited on a glass/ITO substrate and (b) a device stack consisting of a $CuInS_2$/CdS/ZnO trilayer structure deposited on a glass/ITO substrate. $CuInS_2$ and CdS layers were annealed at 300 ℃, while ZnO was annealed at 120 ℃.

X-ray photoelectron spectra (XPS) were collected for Cu_2S, In_2S_3 and $CuInS_2$ films (**Figure 5.12**) confirming the presence of Cu in Cu_2S and $CuInS_2$ films and confirming the presence of In in In_2S_3 and $CuInS_2$ films. Sulfur was present in all the films and the binding energies of the peaks were consistent with metal sulfide bonding states in all samples.

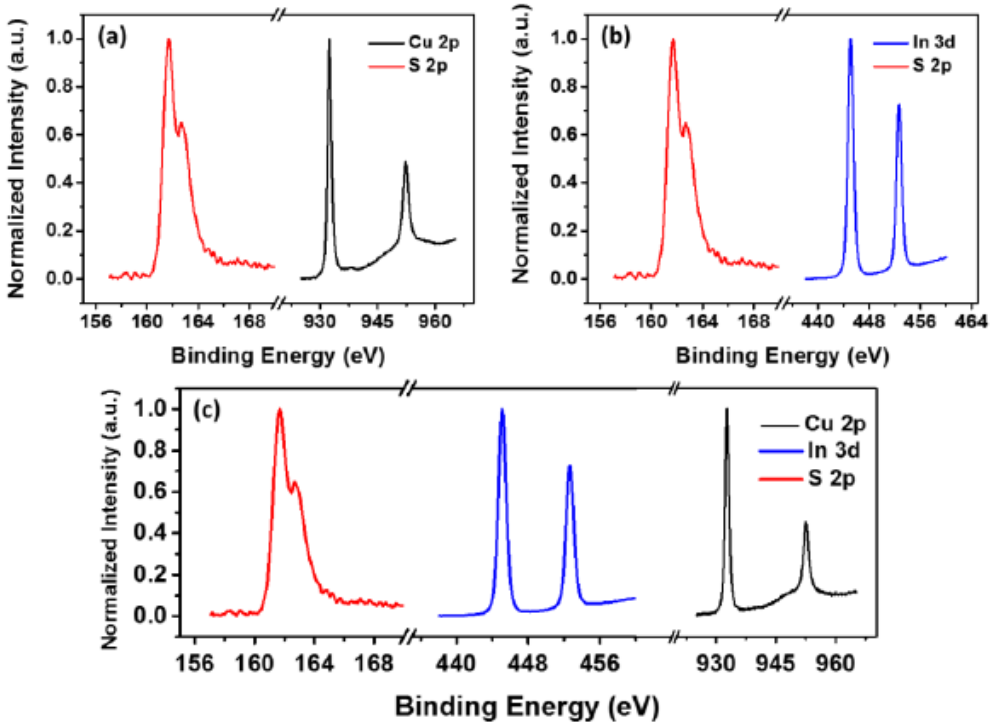

Figure 5. 12. XPS spectra collected for (a) Cu_2S, (b) In_2S_3 and (c) $CuInS_2$ films annealed at 300 ℃.

Ultraviolet photoelectron spectra (UPS) data (**Figure 5.13**) and UV-vis absorption spectra (**Figure 5.7**) were used to construct energy band diagrams as shown in **Figure 5.14**. Work functions (φ) were calculated from the secondary edge onsets (ESE) of each spectrum via the equation $\varphi = 21.2$ eV - ESE. The work functions were found to be 4.9 eV for all of the samples with the composition $Cu(In,Ga)S_2$, compared to 4.8 and 4.2 eV previously reported for CdS and ZnO33. Varying the content of Ga element in $CuInS_2$ film did not affect to the work functions of the materials. Valence band edge energies (E_{VB}) of each layer were obtained from the Fermi edge relative to an Au reference. We completed the energy band diagram deducing the level of the conduction band edge (E_{CB}) of each film from the collected UV-vis absorption data. ZnO and CdS layers showed deep E_{VB}s of 7.2 eV and 6.5 eV, respectively, while three different $Cu(In,Ga)S_2$ films exhibit the same E_{VB} at 5.4 eV. This implies that the different absorption onsets of these films can be ascribed to changes in E_{CB} due to Ga incorporation.

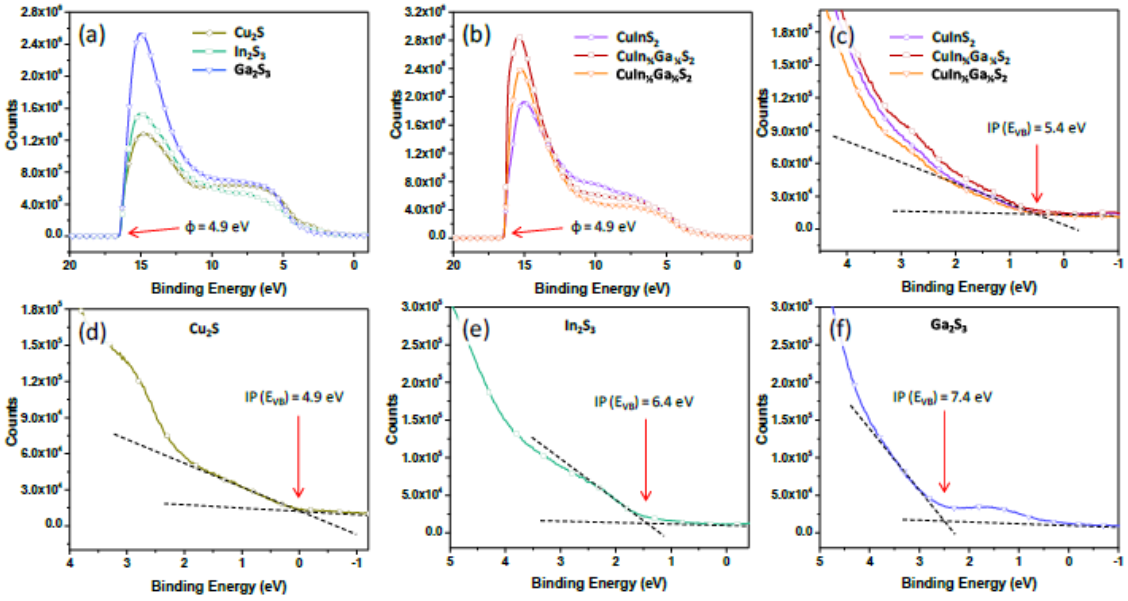

Figure 5. 13. UPS spectra collected on Au substrates with a measured work function of 4.9 eV. (a) Overview of Cu_2S, In_2S_3, and Ga_2S_3 spectra. (b) Overview of $CuInS_2$, $CuIn_{3/4}Ga_{1/4}S_2$ and $CuIn_{1/2}Ga_{1/2}S_2$ spectra. All of the materials show the same work function as the gold substrates (4.9 eV), indicating no vacuum level shift. (c) Close-up of Fermi edge region of $CuInS_2$, $CuIn_{3/4}Ga_{1/4}S_2$ and $CuIn_{1/2}Ga_{1/2}S_2$ films. (d-f) Close-up of Fermi edge regions of Cu_2S, In_2S_3 and Ga_2S_3 films, respectively. Ionization potentials (IPs) were calculated relative to the work function of the Au substrates. All films were annealed at 300 ℃.

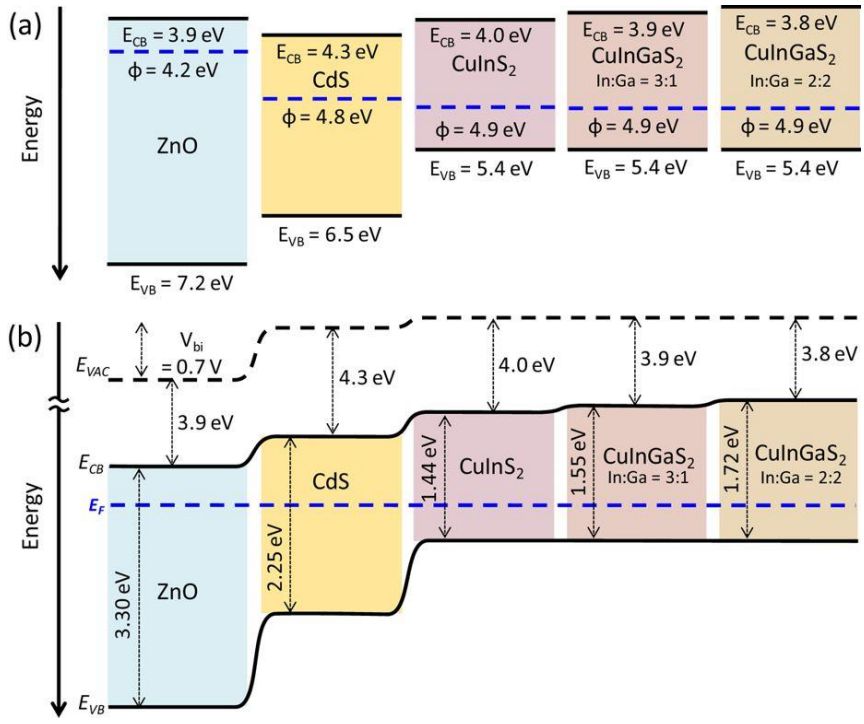

Figure 5. 14. Energy band diagrams. (a) Absolute work function, valence and conduction band energies of each material. (b) Band diagram constructed from UPS and UV-vis absorption data.

Solar cells were prepared by spin coating and annealing TAMTs onto conductive, transparent ITO substrates with an ITO/ZnO/CdS/$CuInS_2$/MoO_3/Au structure. $CuInS_2$ layers were spin cast with 1:1 molar ratio of CuTDT and InTDT and annealed at 300 ℃ for 45 min. CdS window layers were also fabricated from Cd thiolate precursor following a similar method developed by our group20. Current density versus potential (*J-V*) characteristics of different thickness of $CuInS_2$ solar cells are shown in **Figure 5.15a**. We controlled the thickness of the $CuInS_2$ layer by varying the number of coats. Using an overall concentration of 100 mg/mL in THF and a spin rate of 1500 rpm, a thickness of ~80–100 nm is obtained for each coat. Devices with 2 coats of $CuInS_2$ layer showed better current density (J_{SC}) and open circuit voltage (V_{OC}) compared to devices with 1 coat of $CuInS_2$. However, further increases in the thickness of the $CuInS_2$ layer caused a decrease in performance. We presume that the annealing temperature of 300 ℃ was not sufficient to fully crystallize the $CuInS_2$ phase, which leads to poor carrier extraction in thick films. A decrease in V_{OC} in the device with more than 2 coats of $CuInS_2$ indirectly verifies an increase in the charge carrier recombination rate in thicker $CuInS_2$ layers.

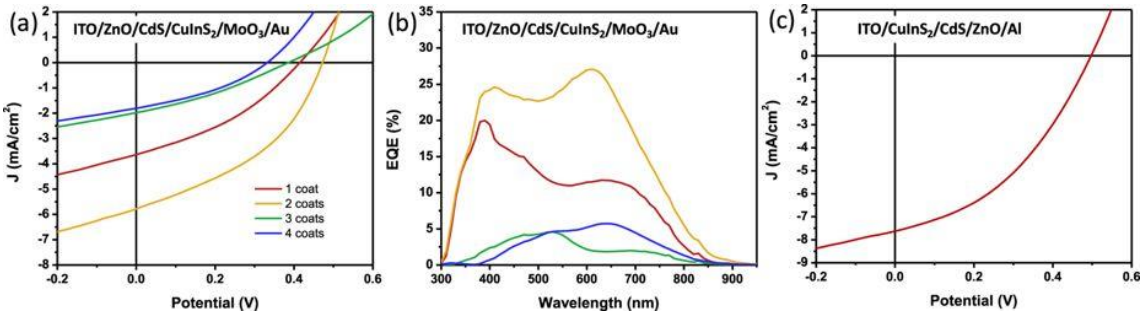

Figure 5. 15. Solar cell characteristics. (a) *J-V* characteristics and (b) EQE spectra of $CuInS_2$ solar cells prepared on ZnO/CdS substrates. (c) *J-V* characteristics of solar cells prepared on ITO substrates.

The solar cell characteristics of the device using an active layer comprising two coats of $CuInS_2$ include a J_{SC}, V_{OC}, FF and PCE of 5.8 mA/cm^2, 0.472 V, 0.408 and 1.11%, respectively. **Figure 5.15b** shows the external quantum efficiency (EQE) of the devices. We expected that the enhanced absorption of the thicker $CuInS_2$ layer would increase the J_{SC}. However, the EQE was significantly reduced after 2 coats of $CuInS_2$. This indicates that the reduced EQE can be attributed to lowered internal quantum efficiency of the device, or poor charge carrier extraction due to the ill-defined crystalline structure confirmed by Raman (**Figure 5.6**) and XRD patterns (**Figure 5.8**). The different spectral shape of the EQE depending on the thickness of the devices arises from optical interference effects inside the active layer due to the thickness of the active layer, which is comparable to the wavelengths of incident light. Although such optical interference effects are unusual in CIGS devices (which are typically thicker than 1000 nm) they are common in devices with thin active layers such as organic and perovskite solar cells. Devices were prepared in an inverted architecture by depositing the $CuInS_2$ film (two coats) first onto

glass/ITO substrates, followed by deposition of CdS and ZnO layers. A *J-V* curve corresponding to this device architecture is shown in **Figure 5.15c**. The performance in this architecture was somewhat improved, including a J_{SC}, V_{OC}, FF and PCE of 7.4 mA/cm^2, 0.497 V, 0.403 and 1.53%. These PCE values are comparable to other $CuInS_2$ devices prepared by solution processing methods such as NPs or other precursors without a high-temperature annealing or selenization step[103, 105, 123], however, are low compared to $CuInS_2$ or $Cu(In,Ga)Se_2$ devices which are grown epitaxially or selenized at high temperature. Although the films are chemically pure, the relatively low PCE and thin optimum active layer thickness are consistent with a disordered film structure with small crystal domains, where abundant grain boundaries lead to short minority carrier diffusion lengths and limit the active layer thickness. Initial attempts to increase the annealing temperature to 400 ℃ unfortunately led to a dramatic drop in V_{OC} and high rate of device failure, which we presume may be due to instability between the ITO substrates and deposited chalcogenide layers at high temperatures. Although the band structure of the Ga-doped films indicates a slope in the conduction band which should provide an increased driving force pushing photogenerated electrons towards the p-n junction, initial attempts to incorporate Ga into the device structure yielded low J_{SC} values. We are currently investigating methods to improve the crystallinity of the materials using higher annealing temperatures with alternative substrates such as molybdenum, as well as post-deposition selenization, which we anticipate will allow much higher efficiencies.

5.4 Conclusion

Various metal thiolates (Cu, In, Ga) were synthesized as effective metal sulfide precursors through a low-cost and straightforward synthetic strategy. Spin coated films could be easily processed using non-polar and non-toxic solvents and decomposed cleanly at moderate temperatures to yield films free of organic residue. The volatile decomposition products were identified as dialkyl sulfides indicating that the complexes decomposed via a well-defined SN_1 mechanism, analogously to the TBOC group. Binary, ternary, and even quaternary systems of metal sulfide films were solution-processed using mixed TAMT precursor solutions by spin casting followed by mild thermal annealing. The versatility of this method was demonstrated using four different metal complexes. The films were characterized electronically and exhibited band structures consistent with semiconducting Cu_2S, In_2S_3, $CuInS_2$ and $Cu(In,Ga)S_2$ films. Functional solar cells were fabricated using the same techniques and equipment used for polymer solar cells by successive deposition of metal sulfide layers. This report marks the first of its kind to demonstrate the preparation of environmentally friendly $CuInS_2$ type solar cells from non-polar thiolate precursors which are soluble in common organic solvents. In contrast with the widely used epitaxial growth methods used to prepare metal chalcogenide films, this approach constitutes a rapid, low-cost, strategy to prepare metal chalcogenide thin films, which is compatible with large-scale deposition methods such as printing or roll-to-roll coating. It offers great potential for application in the fabrication of a range of large-area semiconducting devices such as solar cells, LEDs, photodiodes and transistors, as well presenting the possibility for use in conjunction with solution-processed organic and hybrid semiconducting devices.

CHAPTER 6. Optically Tunable Plasmonic Two-Dimensional Ag Quantum Dot Arrays for Optimal Light Absorption in Polymer Solar Cells

The content of this chapter is published in *J. Phys. Chem. C.* **121**, 17569 (2017)

6.1 Research background

Low short-circuit current density of polymer solar cells has been one of the most critical concerns in polymer solar cells due to its tens of nanometers thick active layer for an optimal device operation.[95, 124] Incorporating metal nanoparticles inside the device can effectively improve the short-circuit current density owing to light-matter interaction between incident photons and conduction electrons of the metal nanoparticles at resonance frequency.[125-126] The excited collective oscillation of the electrons, which is spatially confined in the nanoparticles is called localized surface plasmon resonance (LSPR).[127] At the resonance frequency, LSPR induces a dipolar excitation of electric fields around the nanoparticles, which has the intensity of an order higher than the incident field intensity. Furthermore, an enhanced light scattering by the nanoparticles as scattering centers can be guided into the active layer. Careful control of two physical phenomena can be utilized to improve the short-circuit current density.

In order to place the resonance frequency where the device exhibits poor photon to electron conversion efficiency, the size, shape and its composition[128-130] are generally tuned. However, these generally bring chemical complexity during the nanoparticle synthesis step. Hence, it is more preferable to vary the refractive index of surrounding medium in solid form, which has not yet been studied in detail, as an efficient method to manage plasmonic characteristics of the nanoparticles.

In this manuscript, we prepare 2-dimensional array of Ag quantum dots (2D Ag QAs) on indium tin oxide (ITO) coated glass substrate by using the method called block copolymer micellar lithography. For a tune of plasmonic characteristics of 2D Ag QAs, two electron transport layers (ETLs), ZnO and TiO_2 are utilized as surrounding media of the QDs.

When dipolar excitation of the nanoparticles is only considered, which is common in ~ 10 nm diameter, extinction cross-section, C_{ext} of the spherical nanoparticles according to Mie's solution of Maxwell's equation is given as:[131]

$$C_{\mathrm{ext}} = \frac{24\pi^2 R^3 \varepsilon_m^{3/2} N}{\lambda \ln(10)} \frac{\varepsilon''}{(\varepsilon' + \chi \varepsilon_{\mathrm{m}})^2 + \varepsilon''} \quad (6\text{-}1)$$

where R is the radius of the nanoparticles, ε_m is the permittivity of the surrounding medium, N is the electron density, and ε' and ε'' is the real and imaginary part of the dielectric function of the metal. χ is the geometrical factor, which is 2 for the spherical particle. In this case, the surrounding media are transparent metal oxides, which exhibit extinction coefficient, $k \approx 0$. Consequently, the extinction cross-section of 2D Ag QAs is dependent predominantly on the refractive indices of the surrounding media according to the following relation:

$$\varepsilon = \varepsilon' + i\varepsilon'' = (n + ik)^2 = (n^2 - k^2) + i(2nk) \quad (6\text{-}2)$$

where n and k denote the real and imaginary parts of the complex index of refraction, respectively.

ZnO and TiO_2 are known as efficient electron transport materials for polymer solar cells, which they possess similar optical and electronic properties, while the refractive index of each material is far different. Each electron transport layer is prepared using metal oxide nanoparticles on the 2D Ag QA coated ITO substrate, which allows the least damage to the 2D Ag QAs for the device fabrication. We characterize optical and electronic properties of the plasmonic solar cells depending on the type of electron transport layer by both experiment and simulation. Through the deduced results, it is found that the main enhancement of the device performance mainly arises from the enhanced short-circuit current density by relatively stronger directional light scattering into the active layer by 2D Ag QAs rather than the induced dipolar excitation of 2D Ag QAs.

6.2 Experimental and computational details

Fabrication of 2D Ag QAs

2D Ag QAs were fabricated by block copolymer micelle lithography (BCML). Polystyrene-*block*-poly(2-vinylpyridine) (PS-*b*-P2VP) block copolymers (purchased from Polymer Source, Montreal) with molecular weights of 417 kg/mol (M_n^{PS} = 325 kg/mol, M_n^{P2VP} = 92 kg/mol), 214 kg/mol (M_n^{PS} = 172 kg/mol, M_n^{P2VP} = 42 kg/mol), 265 kg/mol (M_n^{PS} = 133 kg/mol, M_n^{P2VP} = 132 kg/mol), 428 kg/mol (M_n^{PS} = 213 kg/mol, M_n^{P2VP} = 215 kg/mol), and 793 kg/mol (M_n^{PS} = 440 kg/mol, M_n^{P2VP} = 353 kg/mol) were used. These copolymers were dissolved in toluene (0.5 wt % solution) as the precursor solutions. Then, silver nitrate ($AgNO_3$) was added to the precursor solutions with a molar ratio of 0.5 (Ag^+ ions/vinylpyridine repeat unit) and stirred overnight at room temperature. The precursor solutions were spin-cast on cleaned indium tin oxide (ITO) substrates at 3000 rpm for 40 s and then exposed to hydrogen (H_2) plasma for 3 min to etch the polymer template.

Polymer Solar Cells Fabrication and Characterization

Polymer solar cells were fabricated with an inverted configuration of ITO glass/2D Ag QAs/ZnO NPs or TiO_2 NPs/PTB7:$PC_{71}BM$/MoO_3/Ag, where ZnO NPs and TiO_2 NPs were synthesized following protocols reported elsewhere. The thicknesses of electron transfer layers were measured by profilometry.

Patterned ITO-coated glass substrates were cleaned by ultrasonication using detergent, distilled water, acetone, and isopropanol and dried in an oven overnight at 100 °C. After application of 2D Ag QAs (described above), ZnO NPs or TiO_2 NPs were spin-coated at 3000 or 1500 rpm for 40 s on top of patterned 2D Ag QAs, and baked at 100 °C for 10 min or 150 °C for 30 min, respectively. Photoactive layers were spin-cast from solutions containing a blend of PTB7:$PC_{71}BM$ dissolved in chlorobenzene (CB) solvent at a concentration of 12 mg/mL with additional (3% v/v) diiodooctane (DIO) as a solvent additive. After drying, MoO_3 (5 nm) and Ag (85 nm) anodes were sequentially deposited on top of the active layers by thermal evaporation under high vacuum ($<10^{-6}$ Torr).

Discrete Dipole Approximation (DDA) Method and Quantum Effects

DDA is a method to calculate the optical properties of an arbitrarily shaped target material, which is partitioned into a finite array of dipole points. To set appropriate dipole spacing, the criterion of $|m|kd < 1$ must be satisfied, where $|m|$ is the modulus of complex refractive index, k is the reciprocal value of the incident wavelength, and d is the dipole spacing. For the DDA calculations, we used the DDSCAT program (ver 7.3.0).[132-133] The dielectric functions of ITO, ZnO, and TiO_2 were taken from Sopra N&K Database (Sopra Group, Belfast, Ireland), literature,[134-135] and our own experimental measurements, respectively. The dielectric function of silver was determined as a function of quantum dot radius since quantum effects became significant as the size of the metal nanoparticles approached the mean free path

length of conduction electrons in the bulk metal. Also, intrinsic size and nonlocal effects were considered in this work. To apply these two quantum effects, we used the modified dielectric function of bulk metals as follows,

$$\varepsilon(k,\omega,R) = \varepsilon_{bound\ electrons}(\omega) + \varepsilon_{free-electrons}(k,\omega,R) \quad (6\text{-}3)$$

The first term includes the interband transition from d-band to the conduction sp-band. However, when the radius of the metal nanoparticle is over 1 nm, this term becomes independent of the size.[136] Hence, the quantum effects were not included in the first term and the bulk dielectric function of bound electrons, taken from Palik's handbook,[137] was used. But for the second term, the Drude-Sommerfeld model including the intrinsic size and nonlocal effects was used as follows,

$$\varepsilon_{free\ electrons}(k,\omega,R) = 1 - \frac{\omega_p^2}{\omega\left(\omega + i\gamma_{free}(R)\right) - \beta^2 k^2} \quad (6\text{-}4)$$

where ω_p is the bulk plasma frequency, which was 1.36×10^{16} Hz,[138] and γ_{free} is the damping constant for conduction electrons. The intrinsic size effect was implemented by adding the size-dependent term as follows,[136]

$$\gamma_{free}(R) = \gamma_{bulk} + \frac{\nu_F}{R} \quad (6\text{-}5)$$

where ν_F is the Fermi velocity, R is the radius of the particle, and C is a constant related to electron scattering. The values of γ_{bulk}, ν_F, and C were 1.36×10^{13} Hz, 1.39×10^{15} nm/s, and 0.75, respectively.[138-139] The $\beta^2 k^2$ trem represents the nonlocal effect,[140-141] where k (i.e., wave vector) is $2\pi/b$ (b is the particle size), and β^2 is $A\nu_F^2/D$ (D is the dimension of the target structure and $A = 1$ for low frequencies and $A = 3D/(D+2)$ for high frequencies). The values of D and A were set to be 3 and 1.8, respectively, in this work.

Model Systems

We considered three model systems (Figure 6.1) to investigate key factors, which affected the performance of PSC devices. First, to calculate optical properties (i.e., extinction spectra), model systems were constructed using Ag quantum dots with 10 nm diameter on top of ITO substrates with dimensions of 58 × 58 × 11 nm, and 20 nm (30 nm) thick ZnO (TiO_2) ETLs (Figure 6.1a). Second, to calculate the spatial distribution of the electric field (to observe the near-field effect), a 90 nm thick PTB7:$PC_{71}BM$ active layer was added to the previously described model system (Figure 6.1b). To calculate the far-field scattering, we assigned Ag quantum dots as the main scattering object and

changed the medium according to the corresponding ETL's refractive index (i.e., ZnO and TiO_2) as shown in Figure 6.1c. Periodic boundary conditions were applied to implement an infinite array into all systems. The ambient medium was air for the model systems used to obtain the optical properties and the near-field enhancements. For the far-field scattering calculation, the ambient medium was ZnO or TiO_2. The dipole spacing (d) was set to 1 nm for all systems.

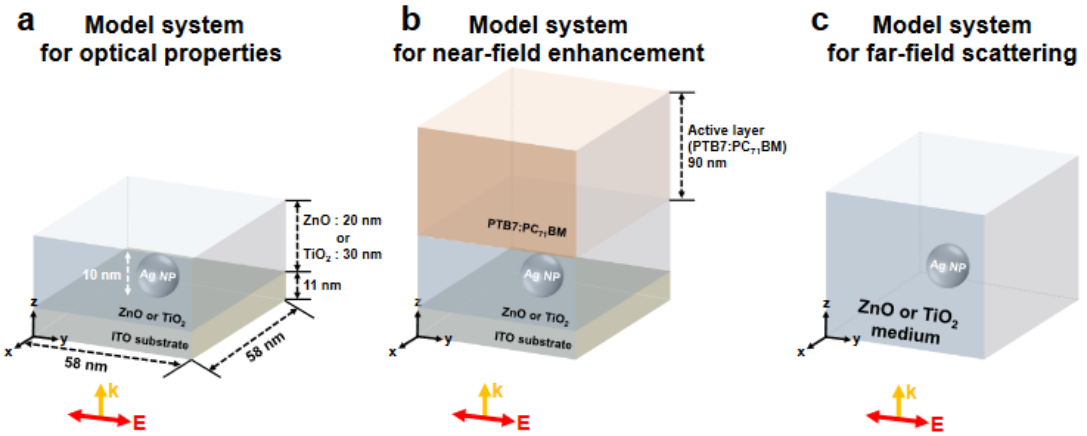

Figure 6. 1. Model systems used in the DDA calculation. (a) Model system for calculating the extinction spectra in ZnO or TiO_2 layer systems, which consisted of a total of 104,284 or 137,924 dipoles, respectively. (b) Model system used for calculating the near-field enhancement (i.e. electric field contour plot). An active layer (i.e. PTB7:$PC_{71}BM$) was added to the model system in (a), which consisted of 407,044 dipoles for the ZnO layer system and 440,684 dipoles for the TiO_2 layer system, respectively. (c) Model system for calculating the far-field scattering of 2D Ag QAs, which consisted of 552 dipoles in an infinite ZnO or TiO_2 medium. E (red arrows) and k (orange arrows) indicate the directions of electric field and incident light, respectively. Periodic boundary conditions (PBCs) in x- and y-axis directions were applied in all systems.

6.3 Results and discussion

Prior to the application of 2D Ag QAs into PSCs, it is necessary to optimize both the size of quantum dots and dot-to-dot spacing. Excessively large metal particles (>30 nm) may, for example, have an influence on the internal quantum efficiency (IQE) of the device arising from direct contact between photogenerated excitons and the metal. Additionally, excessively dense 2D Ag QAs can reduce the transmittance of light through the transparent substrate. For these reasons, BCML was carried out to achieve optimal quantum dot size and spacing. This method allows accurate control of the size of the quantum dots with a narrow distribution of particle diameters, while also allowing control of the density of quantum dots by varying the molecular weight of the block copolymers that are utilized as soft templates.[142-143]

In this work, polystyrene-*block*-poly(2-vinylpyridine) (PS-*b*-P2VP) block copolymers were used for BCML **(Figure 6.2a)**. A 0.5 wt % solution of PS-*b*-P2VP was prepared in toluene, which is a selective solvent for hydrophobic PS blocks, leading to the formation of a micellar structure with P2VP cores and PS coronas. $AgNO_3$ was added to the polymer solution with a molar ratio of 0.5 Ag^+ ions per vinylpyridine repeat unit. The solution was then stirred thoroughly for selective penetration of Ag^+ ions into the P2VP micellar cores. Ag^+-incorporated polymer micelle solutions were spin-cast onto ITO glass substrates, followed by removal of the polymer templates by hydrogen (H_2) plasma treatment to yield reduced 2D Ag QAs.

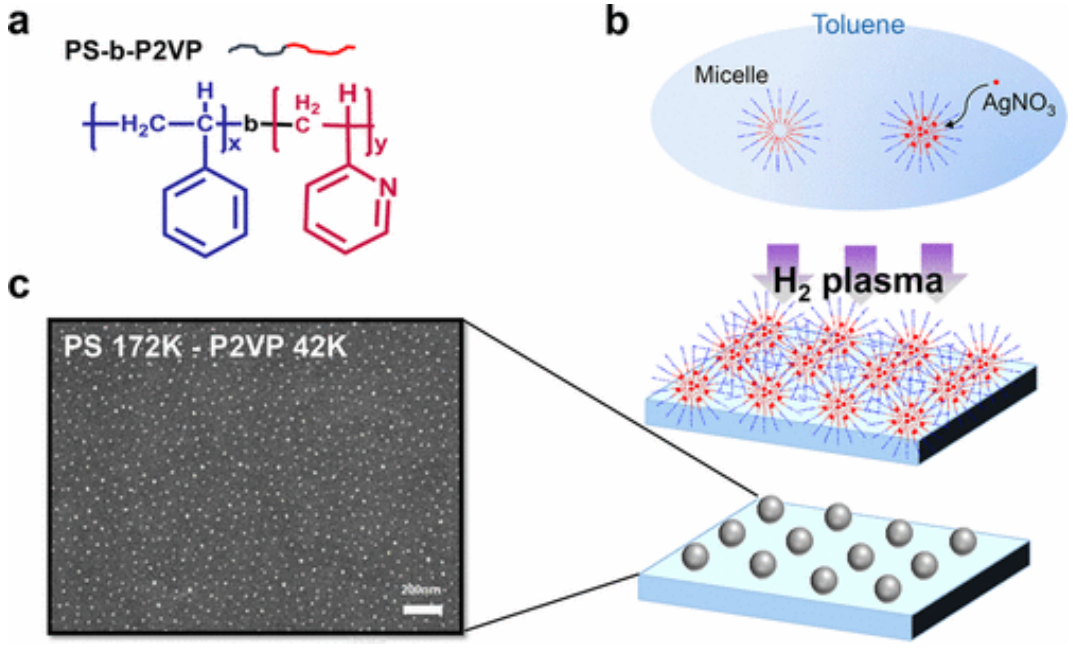

Figure 6. 2. (a) Chemical Structure of the Polystyrene (Blue) and Poly-2-vinylpyridine (Red) Block Copolymer Molecule; (b) Schematic View of the Fabrication of 2D Ag QAs via BCML; (c) SEM Image of 2D Ag QAs Using PS(172000)-*b*-P2VP (42000) Block Copolymer on an ITO Substrate

We prepared 2D Ag QAs using 214000 (PS 172000–P2VP 42000) PS-*b*-P2VP resulting in an average particle diameter of 10 ± 2 nm and a dot-to-dot spacing of 48 ± 2 nm, as shown in scanning electron microscopy (SEM) images **(Figure 6.2c**). A summary of intrinsic properties, SEM image statistics, and transmittance spectra of 2D Ag QAs as a function of the molecular weight of PS-*b*-P2VP polymers are summarized in **Figure 6.3** and **Table 6.1**. Various block copolymers were prepared as precursor materials, which could determine size and density with controllable distance of Ag QAs. In detail, since host solvent was toluene of hydrophobic property, micellar structures were formed with polystyrene (PS) coronas and poly(2-vinylpyridine) (P2VP) core. P2VP molecular number determined size of Ag QDs due to interpenetrated Ag^{+} ions into P2VP core, while that of PS coronas lead to interval of Ag QDs.

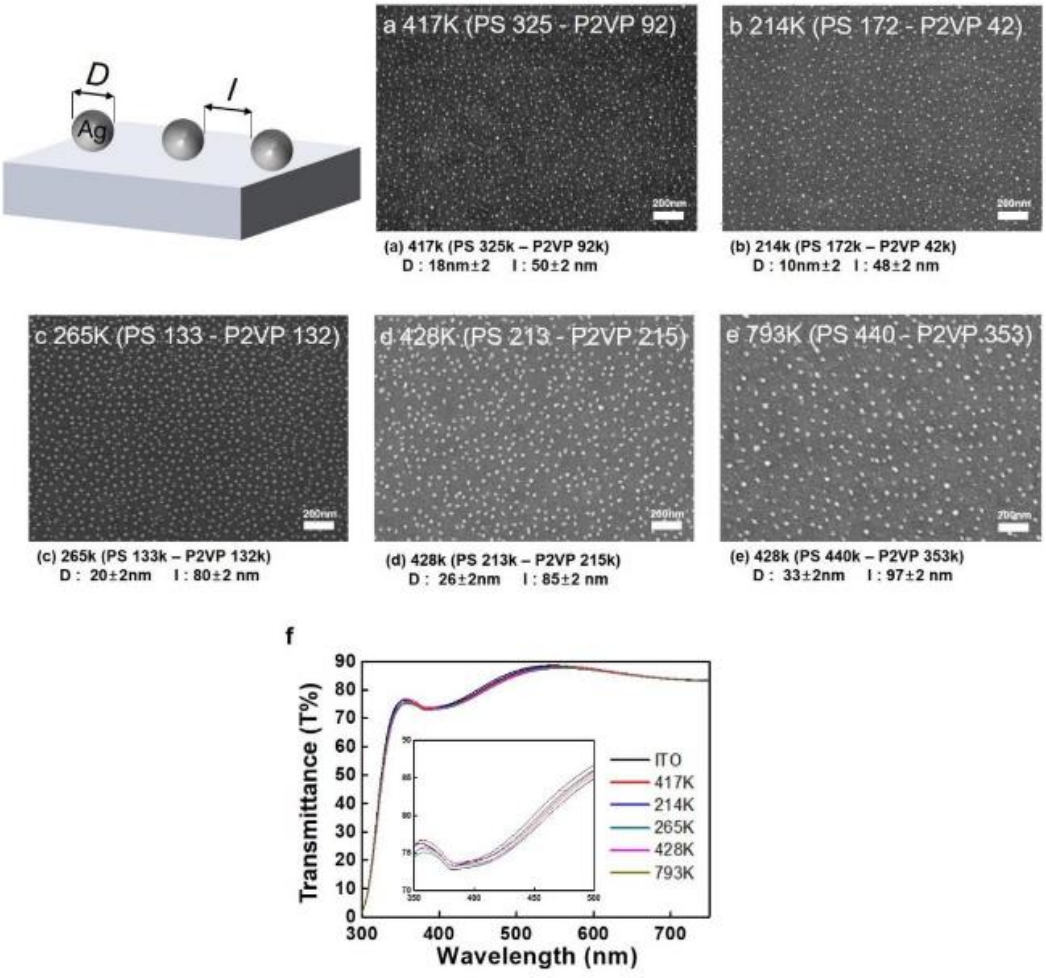

Figure 6. 3. Comparison of 2D Ag QAs using block copolymer micellar lithography (BCML): (a)-(e) SEM images of Ag quantum dot patterns on ITO substrates prepared using different block copolymers. The measured interval distances and quantum dot diameters are noted as I and D, respectively, below each image. (f) Transmittance spectra corresponding to the 2D Ag QAs shown in (a)-(e).

Table 6. 1. Number-average molecular weights and polydispersities of block copolymers compared to sizes, interval distances and PSCs performance of 2D Ag QAs with various geometric conditions.

BCP	PS (Mn kDa)	P2VP (Mn kDa)	PDI (Mw/Mn)	Average size of Ag quantum dots (nm)	Average distance between Ag quantum dots (nm)
A	325	92	1.06	18±2	50±2
B	172	42	1.08	10±2	48±2
C	133	132	1.15	20±2	80±2
D	213	215	1.29	26±2	82±2
E	440	353	1.19	33±2	97±2

Considering polymer solar cells (PSCs) fabrication, the transmittance of 2D Ag QAs coated ITO glass is important. Because incident light through ITO and 2D Ag QAs embedded in ETL have effect on charge generation in photoactive layer of PSCs, comparable transmittance of minimum absorption and reflection losses were required at visible wavelengths. As shown in **Figure 6.3f**, the BCML based on PS 172-P2VP 42 has the highest optical transmittance.

To characterize the optical properties inherent to synthesized 2D Ag QAs, we performed UV–vis absorption measurements. For the UV–vis measurements, 2D Ag QAs on ITO-coated glass substrates were covered with ZnO or TiO_2 layers (**Figure 6.4a**). Each metal oxide layer was spin-cast using nanoparticles which were prepared following procedures reported elsewhere.[144-145] **Figure 6.4b** shows the experimental absorbance spectra for two 2D Ag QAs samples embedded in ZnO and TiO_2 media. The LSPR extinction peak for ZnO-covered 2D Ag QAs occurs at 480 nm wavelength, while the peak for TiO_2-covered 2D Ag QAs exhibits a bathochromic shift of 40 nm. The higher refractive index of the TiO_2 layer relative to the ZnO layer clearly resulted in a bathochromic shift of the LSPR of the nanoparticles, consistent with Mie's theory.

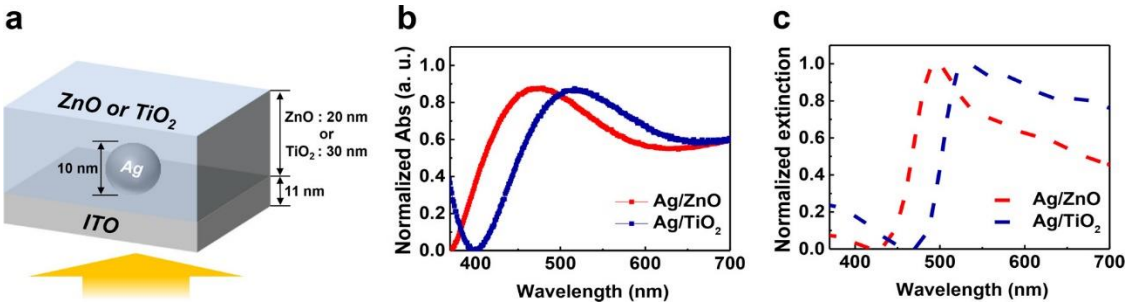

Figure 6. 4. (a) Schematic diagram of Ag quantum dots embedded in ZnO and TiO_2 electron transport layers (ETLs). The thicknesses of the ETLs were 20 nm for ZnO and 30 nm for TiO_2 layers, respectively. (b) Normalized experimental absorbance and (c) normalized extinction spectra of 2D Ag QAs in ETLs obtained via DDA calculation. Each extinction spectrum of the ZnO and TiO_2 systems was obtained from the difference of each film with and without 2D Ag QAs.

To confirm experimental observations, we performed DDA calculations.[132-135] Before performing the calculations, one critical issue was considered, which is whether the quantum confinement effects[136-139] significantly affected the properties of the small-sized metal nanoparticles used in this study. In previous studies, quantum effects have been neglected in the context of polymer solar cells due to the large size of metal nanoparticles (i.e., diameter >20 nm).[146-148] However, in our system, the size of Ag quantum dots was 10 nm. In general, when the diameter of metal nanoparticles is less than 20 nm, quantum effects appear which affect LSPR properties.

Considering quantum effects such as spatially nonlocal response of polarization and size dependent damping effects in our 10 nm Ag quantum dots, we implemented the hydrodynamic Drude model in

DDA calculations to calculate the extinction spectra (Figure 6.4c). The results were consistent with the measured UV–vis absorbance, as shown in Figure 6.4b. Furthermore, when we compared the extinction spectra including the quantum effects (Figure 6.4c) to nonquantum effects.[140-141] (**Figure 6.5**), the overestimated extinction spectra of ZnO and TiO_2 layers below 500 nm wavelength were reduced and subpeaks, which appeared over 550 nm wavelength, were smoothed out. These results indicated that quantum effects in 10 nm Ag quantum dots are ineluctable and must be dealt with to accurately model this system.

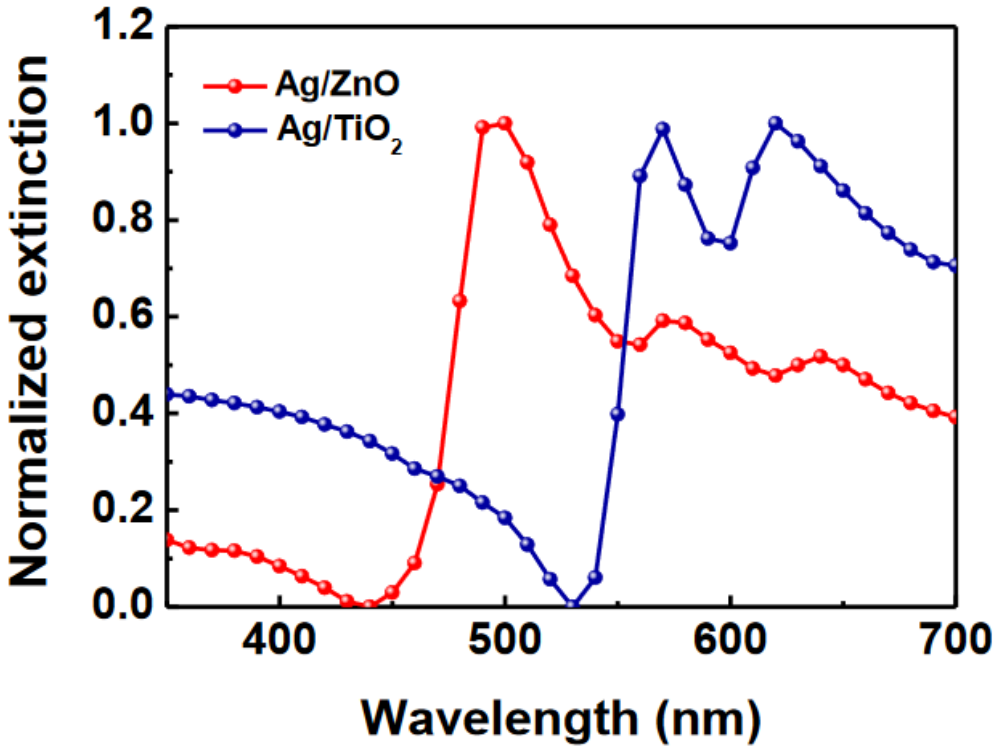

Figure 6. 5. Calculated extinction spectra of 2D Ag QAs in each ETL without applying quantum effects.

Next, to verify the effect of plasmon coupling between Ag quantum dots in 2D Ag QA systems, we calculated the extinction spectra of isolated Ag quantum dots, which consisted of one Ag quantum dot (**Figure 6.6a**) and compared this to an infinite array (**Figure 6.6b**). The isolated Ag quantum dot system showed a sharp extinction peak at its characteristic resonance wavelength, consistent with previously reported results from a number of plasmonic research studies.[149-151] In contrast, the arrayed Ag quantum dots exhibited a broad resonance peak with a bathochromic shift of ~30 nm. Thus, we infer that plasmon coupling between adjacent Ag quantum dots was one of the key mechanisms which led to the improved performance of PSC devices in this work.

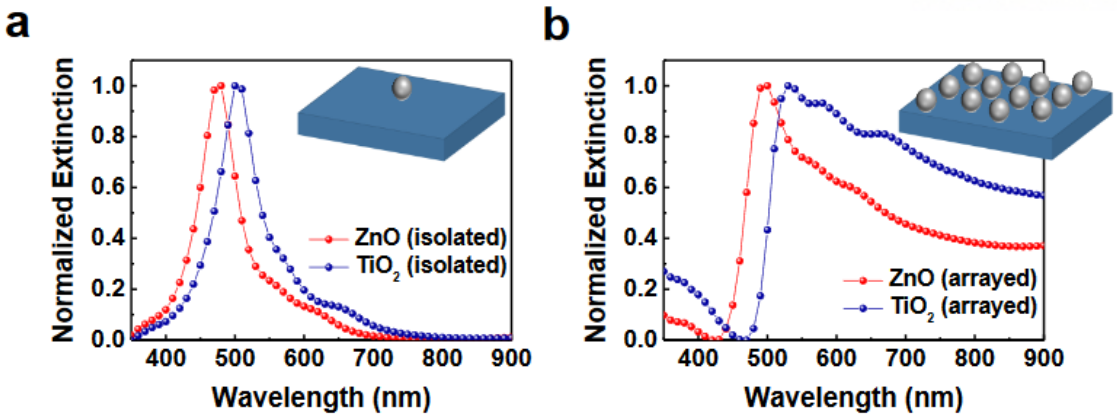

Figure 6. 6. Calculated extinction spectra of (a) isolated Ag quantum dot from Figure 6.1a, where the PBCs were not applied, and (b) two-dimensionally arrayed Ag quantum dots extended from Figure 6.1a with PBCs.

PSCs were constructed using a blend of [4,8-bis[(2-ethylhexyl)oxy]benzo[1,2-*b*:4,5-*b*′]dithiophene-2,6-diyl][3-fluoro-2-[(2-ethylhexyl)carbonyl]thieno[3,4-*b*]-thiophenediyl] (PTB7) and [6,6]-phenyl C_{71} butyric acid methyl ester ($PC_{71}BM$) as an active layer. The device architecture used was glass/ITO/Ag quantum dots/ZnO or TiO_2/PTB7:$PC_{71}BM$/MoO_3/Ag (**Figure 6.7a**). 2D Ag QAs were synthesized by BCML using 214000 (PS 172000–P2VP 42000) block copolymers. This block copolymer exhibited superior transmittance and PSC performance, without a reduction in fill factor (FF) compared to other PSCs incorporating 2D Ag QAs prepared using different molecular weight block copolymers. *J*–*V* characteristics of PSCs prepared using PS-*b*-P2VP with various molecular weights are summarized in **Table 6.2**. The optimal thicknesses of ZnO and TiO_2 layers for our structures were around 20 and 30 nm, respectively (see **Table 6.3**).

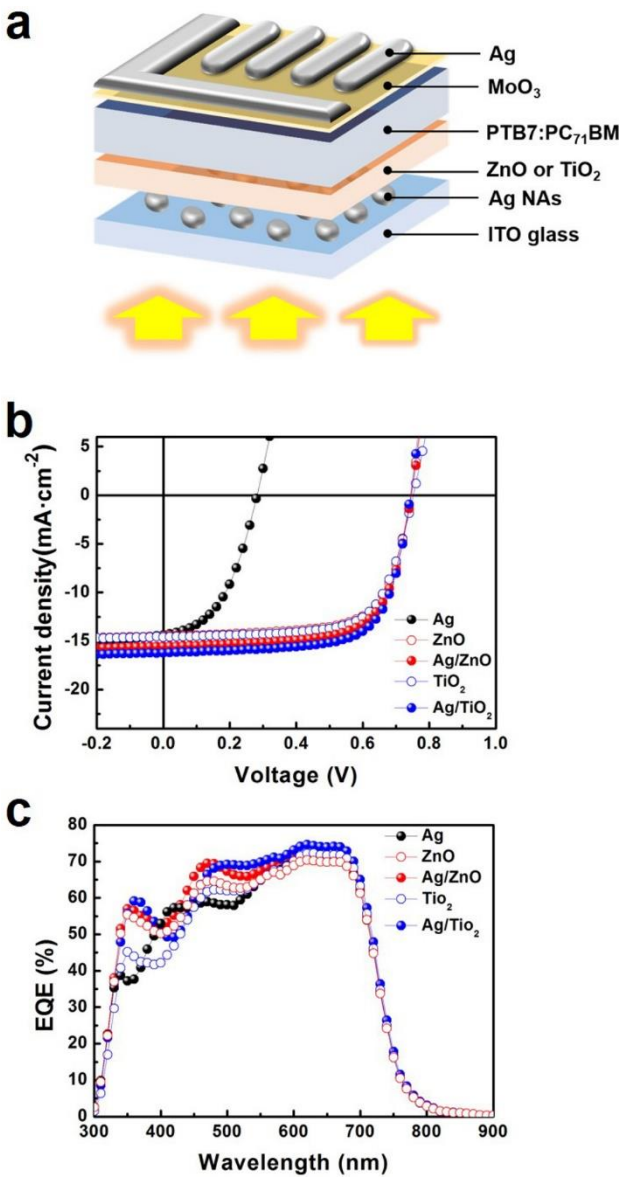

Figure 6. 7. (a) Device structure, (b) *J–V* characteristics under AM 1.5 illumination (100 mW/cm^2), and (c) EQE of OPVs. Black traces correspond to OPVs without ETLs, while red and blue traces correspond to ZnO and TiO_2 ETLs, respectively. Empty circles correspond to devices without 2D Ag QAs while filled circles are with 2D Ag QAs embedded in ZnO or TiO_2 layers.

Table 6. 2. Photovoltaic parameters of the devices using various 2D Ag QAs.

BCP	PS (Mn kDa)	P2VP (Mn kDa)	J_{SC} (mA cm^{-2})	V_{OC} (V)	FF	PCE (%)
-	-	-	14.8±0.88	0.74±0.01	0.66±0.01	7.30±0.12
A	325	92	15.2±1.21	0.74±0.01	0.59±0.04	6.63±0.45
B	172	42	15.4±1.08	0.75±0.01	0.67±0.02	7.66±0.09
C	133	132	15.6±2.63	0.69±0.03	0.46±0.06	5.00±1.21
D	213	215	13.8±3.24	0.55±0.10	0.43±0.11	3.23±2.01
E	440	353	14.6±2.21	0.71±0.07	0.49±0.06	5.06±1.64

Table 6. 3. Device characteristics with variable ETL thicknesses.

Configuration	ETL spin rate (rpm)	ETL average thickness (nm)	J_{SC} (mA cm^{-2})	V_{OC} (V)	FF	PCE (%)
ITO/ZnO NPs/PTB7:$PC_{71}BM$/MoO_3/Ag	800	35	14.8±0.30	0.71±0.01	0.67±0.01	7.34±0.08
	1500	26	15.0±0.38	0.74±0.01	0.66±0.01	7.26±0.06
	3000	20	15.1±0.22	0.74±0.01	0.66±0.01	7.61±0.11
	5000	14	14.8±0.43	0.74±0.01	0.63±0.01	7.45±0.09
ITO/TiO_2 NPs/PTB7:$PC_{71}BM$/MoO_3/Ag	800	42	15.1±2.18	0.74±0.01	0.61±0.06	6.82±0.98
	1500	30	14.8±0.028	0.74±0.01	0.68±0.01	7.45±0.07
	213	215	14.5±0.32	0.74±0.01	0.69±0.01	7.40±0.12
	440	353	13.8±1.21	0.74±0.01	0.67±0.03	6.83±1.05

Figure 6.7b,c shows the current density versus voltage (*J–V*) characteristics and external quantum efficiency (EQE) spectra of PSCs not only with and without 2D Ag QAs embedded in ZnO and TiO_2 but also 2D Ag QAs without ETLs deposited on ITO substrates. PSC parameters are summarized in **Table 6.4**. Devices comprising 2D Ag QAs without electron transport layers (ETLs) showed a low power conversion efficiency (PCE) of 1.87%, because of a low open-circuit voltage (V_{OC}) of 0.23 V, and a low fill factor (FF) of 0.46. The performance of devices with ETLs was dramatically improved, with significant increases in V_{OC} and FF, due to their roles of energy level alignment between the active layer and the electrodes, which facilitated balanced charge extraction as well as preventing charge carrier recombination which is mediated by direct contact between the active layer and metallic nanoparticles.[152-154]

Table 6. 4. Device characteristics of PTB7:$PC_{71}BM$ Based PSCs with or without 2D Ag QAs in different ETLs.

ETL	J_{SC} (mA cm^{-2})	V_{OC} (V)	FF	average PCE (%)	best PCE (%)	cal. J_{SC} (mA cm^{-2})
none	14.4±0.23	0.28±0.02	0.46±0.03	1.87	2.03	14.21
ZnO	14.5±0.17	0.74±0.01	0.69±0.01	7.39	7.40	14.67
Ag/ZnO	15.8±0.19	0.75±0.01	0.69±0.01	7.97	8.18	15.29
TiO_2	14.6±0.21	0.75±0.01	0.69±0.01	7.49	7.55	14.57
Ag/TiO_2	16.2±0.15	0.75±0.01	0.70±0.01	8.27	8.51	15.52

The use of a ZnO layer with 2D Ag QAs increased the PCE substantially, compared to that of the reference device without 2D Ag QAs. Specifically, the J_{SC} was significantly improved from 14.5 to 15.8 mA/cm^2, corresponding to a 9.0% increase upon incorporation of 2D Ag QAs. Likewise, the device using a TiO_2 layer on the 2D Ag QAs reached an optimal PCE of 8.51%. This improvement arose from a remarkable enhancement of J_{SC} from 14.6 to 16.2 mA/cm^2, corresponding to a 11.0% increase compared to reference devices without 2D Ag QAs. The open-circuit voltage and fill factor, however, showed no dramatic change in the presence or absence of 2D Ag QAs, implying that the 2D Ag QAs only increased the photocurrent generation via optical effects without greatly affecting the electronic properties of the devices. It is noteworthy that the insertion of 2D Ag QAs into ETLs resulted in negligible morphological changes of the ETL surface (see **Figure 6.8**). Consequently, the best PCEs were obtained in devices incorporating 2D Ag QAs with ETLs deposited atop the NAs, resulting in performance enhancements of 10.5% in the case of ZnO and 12.7% in the case of TiO_2.

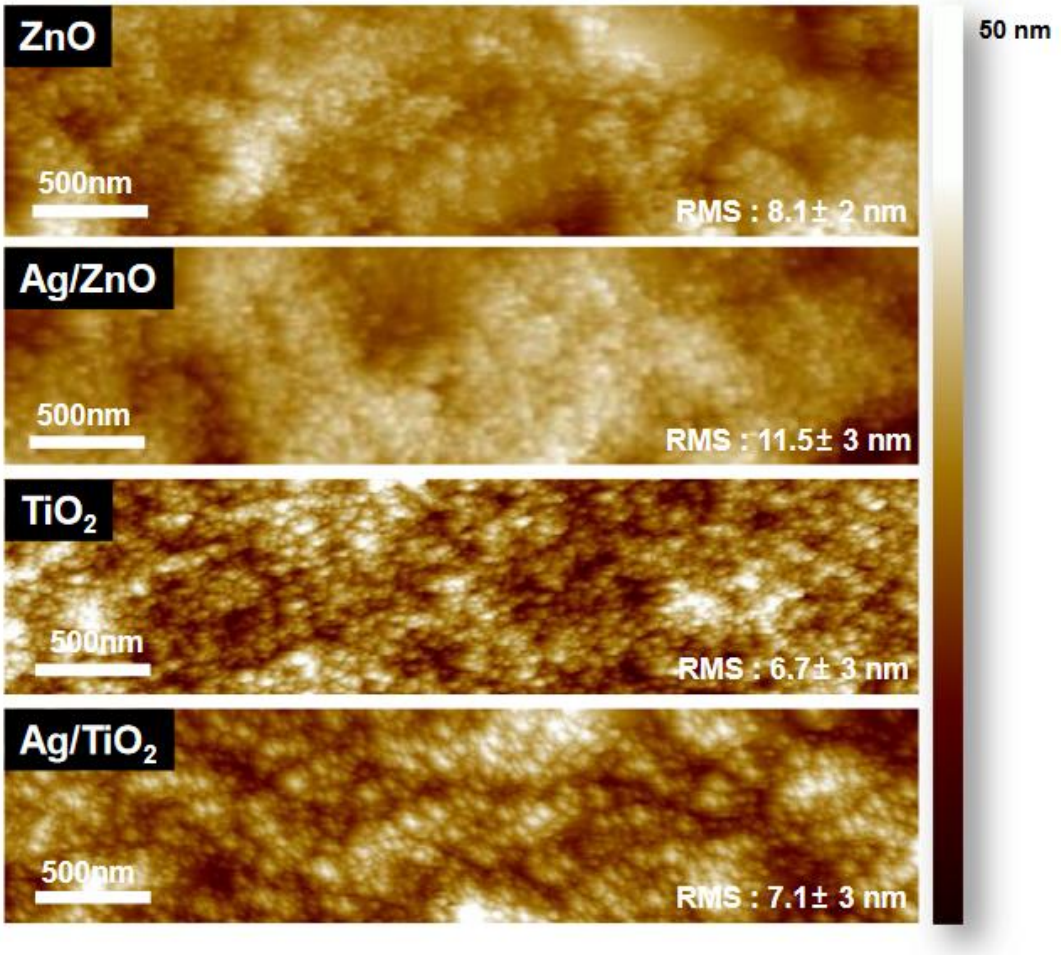

Figure 6. 8. AFM images (4 μm × 1 μm) of ETLs with and without embedded 2D Ag QAs.

To clarify the J_{SC} enhancement, EQE spectra as well as changes in EQE upon incorporating 2D Ag QAs are shown in **Figure 6.9a,c**. The EQE of devices incorporating 2D Ag QAs surrounded by ZnO exhibit enhanced photocurrent generation throughout the visible spectrum from 300 to 700 nm, with a distinct resonant peak at 470 nm, while the EQE spectra of devices with 2D Ag QAs inside TiO_2 also exhibited significantly increased photocurrent generation, with two peaks in improvement around 370 and 510 nm. The EQE enhancement from 350 to 400 nm is due to enhanced transmittance of the TiO_2 matrix after embedding 2D Ag QAs. The transmittance spectra of ETL layers with and without 2D Ag QAs are shown in **Figure 6.10**. We observed that the transmittance improved at wavelengths less than 400 nm, despite the incorporation of 2D Ag QAs. This change can be attributed to reduced scattering of ETL layers upon 2D Ag QAs insertion (see **Figure 6.11**), an effect which was confirmed via DDA modeling. The EQE enhancement from 440 to 570 nm can be attributed to the strong LSPR of the 2D Ag QAs.

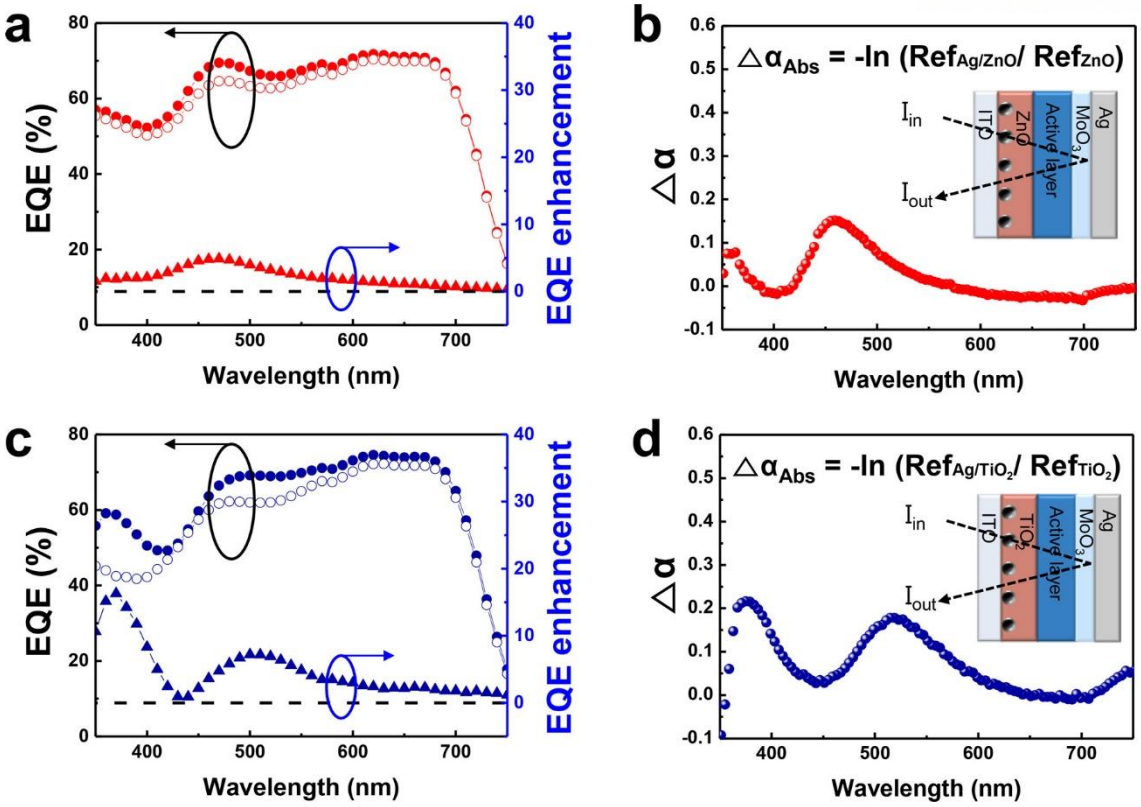

Figure 6. 9. EQE and EQE enhancement. (a, c) EQE with and without 2D Ag QAs embedded in ZnO and TiO_2 ETLs, respectively. (b, d) Measured absorption enhancement due to 2D Ag QAs embedded in ZnO and TiO_2 ETLs (difference in absorption with and without 2D Ag QAs), respectively. Insets depict the configuration of optical reflectance measurements.

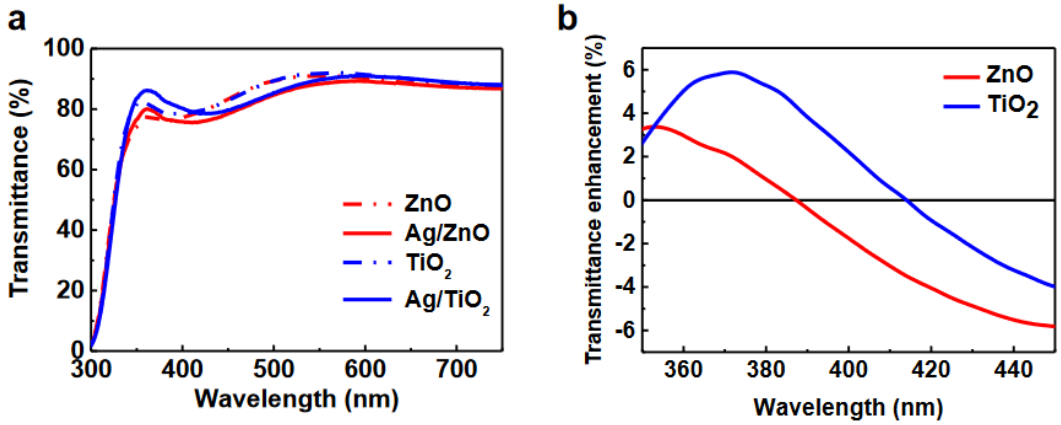

Figure 6. 10. Transmittance spectra. (a) Absolute transmittance of ZnO and TiO_2 layers with and without 2D Ag QAs. (b) Change in transmittance of ETLs with embedded Ag QAs.

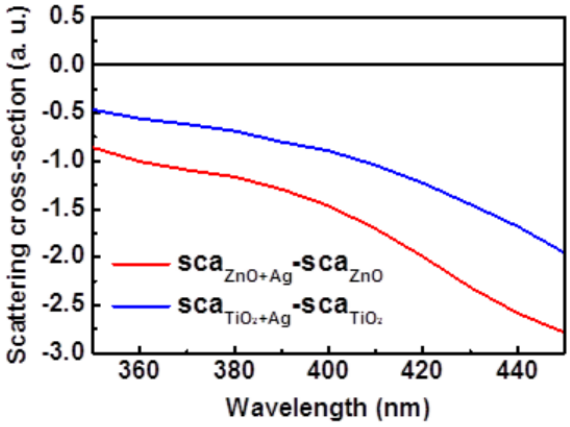

Figure 6. 11. Scattering cross-section difference between ETL + 2D Ag QAs and ETLs only.

Notably, the Ag QAs embedded in TiO_2 showed two strong enhancements at 370 and 510 nm, whereas Ag QAs embedded in ZnO showed only one peak at 470 nm. To understand this difference and to further investigate the effect of Ag quantum dots on the light absorption in the active layer, the absorption enhancement ($\Delta\alpha_{abs}$) was calculated from the following equation based on the reflectance spectra of each film (see **Figure 6.12**).[147]

$$\Delta\alpha_{\mathrm{abs}} = -\ln\left(R_{Ag/ETLs} - R_{ETLs}\right) \tag{6-6}$$

The $\Delta\alpha_{abs}$ spectrum strongly correlates with the EQE enhancement as shown in **Figure 6.7b,d**. This indicates that the enhanced photocurrent in devices with 2D Ag QAs can be attributed to additional absorption of the photoactive layer in these devices. The region of EQE enhancement and $\Delta\alpha_{abs}$ peak of devices with TiO_2 ETLs shifted toward longer wavelengths compared to devices with ZnO ETLs, a consequence of the greater index of refraction of the corresponding medium. This tendency shows excellent agreement with the tendency observed in UV–vis absorption spectra. In addition, it is found that the EQE enhancement and $\Delta\alpha_{abs}$ in the TiO_2 case is higher than that of ZnO. This can be attributed to the stronger intensity of LSPR-enhanced scattering in the case of TiO_2. Whereas ZnO showed a small increase in $\Delta\alpha_{abs}$ below 400 nm, TiO_2 showed a much stronger increase in absorption due to this increased scattering efficiency at short wavelengths, consistent with the increased scattering in TiO_2 predicted by DDA modeling (**Figure 6.11**). These attributes explain why 2D QAs embedded in TiO_2 showed an additional band of EQE enhancement at 370 nm compared to ZnO.

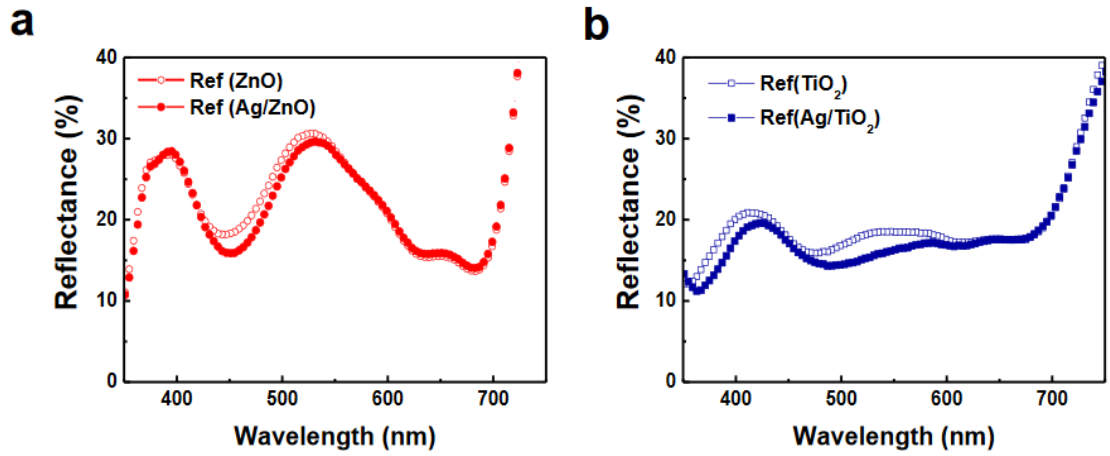

Figure 6. 12. Reflectance spectra of PSCs based on PTB7:PC71BM with 2D Ag QAs embedded in (a) ZnO and (b) TiO_2 layers.

To investigate the effect of 2D Ag QAs on the device performance in different media (i.e., ZnO and TiO_2), we calculated the near-field enhancement inside the devices through electric field contour plots, which show the spatial distribution of the electric field (**Figure 6.13a**), and the far-field scattering of Ag quantum dots (**Figure 6.13b**) at peak wavelengths, respectively.

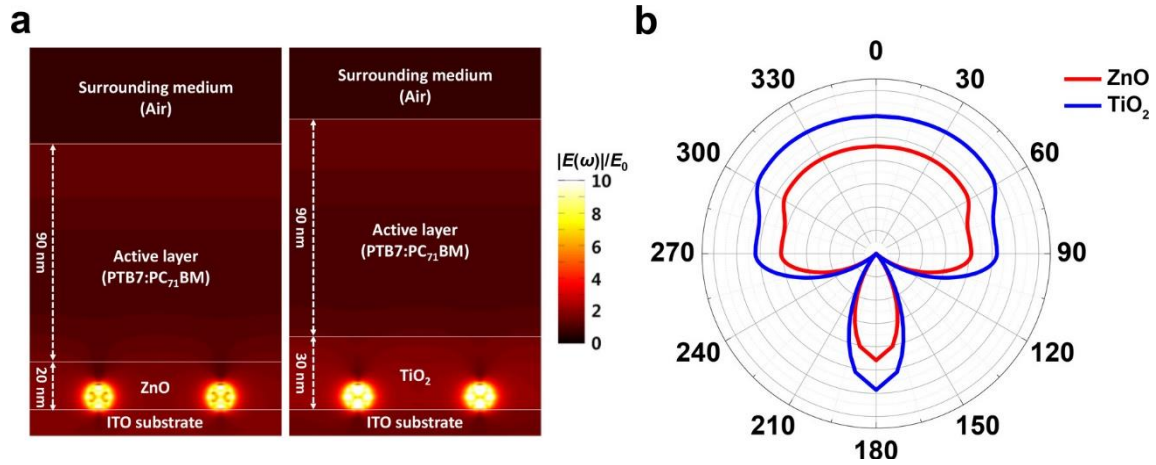

Figure 6. 13. Calculated near-field electric field enhancement and far-field scattering. (a) Spatial distribution of the electric field of the device with ZnO and TiO_2 layers. $E(\omega)$ is the induced electric field and E_0 is the external electric field. (b) Angular plot of the far-field scattering of 2D Ag QAs in each ETL. The results were obtained at a wavelength of 500 nm for ZnO and 530 nm for TiO_2, which were the peak wavelengths in the extinction spectra (as shown in Figure 6.4c).

The intensity of the electric field in the vicinity of the Ag quantum dots was enhanced by about 13–15 times in both ZnO and TiO_2 layers. However, the near-field effect is spatially confined near the surface of Ag quantum dots and cannot propagate to the active layer. Therefore, the active layer could not be significantly affected by the near-field enhancement of 2D Ag QAs, implying that the near-field

effect had only a minor influence on the device performance.[155] In contrast, the far-field scattering of Ag quantum dots showed quite different results (**Figure 6.13b**). When the incident light interacted with 2D Ag QAs, both ETL media showed that the forward direction (i.e., from 0° to 90° and from 270° to 360°) of light scattering was dominant in comparison to backward scattering (i.e., from 90° to 270°). This result indicated that LSPR-enhanced EM wave could effectively propagate to the active layer. The induced variation in the angle of the incident light increased the effective optical path length of light in the active layer; this phenomenon is often called light trapping or a wave-guided mode.[156-157] Similarly, in our system, the light-trapping effect led to increased exciton generation in the active layer. Furthermore, because the far-field scattering shows a large propagation distance, direct contact between excitons and Ag quantum dots is not necessary, confirming that charge recombination by the metallic nanoparticles could be avoided. Overall, we have identified the far-field scattering effect was the main mechanism for enhanced performance in PSC devices. In particular, the higher EQE enhancement in devices using TiO_2 ETLs could be explained largely by the stronger far-field scattering in comparison to ZnO.

6.4 Conclusion

In conclusion, we have demonstrated highly enhanced performance in polymer solar cells using 2D Ag QAs synthesized by BCML. The LSPR peaks of 2D Ag QAs were tuned by varying the index of refraction of the surrounding medium. Ten-nanometer-sized 2D Ag QAs did not greatly affect the transmittance of ITO films; however, they did exhibit strong LSPR intensity in the visible range. DDA calculations of near-field enhancement and far-field scattering, considering quantum effects (i.e., intrinsic size effect and nonlocal effect) demonstrated that the far-field scattering of incident light led to light trapping in the active layer and was the primary reason for enhancement in device performance. Optimized 2D Ag QAs embedded in a TiO_2 ETL resulted in a champion PCE of 8.51%. We believe that the environment-sensitive tunability of LSPR peaks in plasmonic nanomaterials offers a new and powerful method to tune the properties of plasmonic materials for a broad range of applications in various polymer-based optoelectronic devices.

CHAPTER 7. Coordination Complex Triggered High Colloidal Stability of ZnO Nanoparticles for Organic Optoelectronics

The content of this chapter is in preparation for the publication in a journal.

7.1 Research background

ZnO is known as a multifunctional material, which possesses high electrical conductivity[158] and visible transparency (optical band gap, E_{opt} > 3.3 eV), photostability[159-160], and, photocatalytic ability[161-162]. In particular, it has been often utilized as a highly efficient n-type buffer layer of organic optoelectronic devices due to its proper energy level alignment to the active layer with ideal band dispersion[163] for the selective charge extraction (or injection). Sol-gel and sputtering methods are being widely adopted for the preparation of ZnO thin film.[164-168] But the methods cause inevitable damages by thermal annealing or ion bombardments on underlying layers during the deposition processes. It forces their applications to optoelectronic devices only with inverted structure, which the underlying layer is robust oxide layer in most cases. Consequently, synthesis of ZnO NPs have been intensively studied as an alternative method, which are able to reduce processing temperature under 150 °C[169-170] or even requires no thermal annealing[171] to form ZnO thin film. Most studies dispersed the NPs in nonpolar solvent with steric stabilization using long alkyl acid or amine ligands,[172-173] or dispersed in the mixture of polar and nonpolar solvents, which greatly improves colloidal stability compared to the stability of the NPs in mono-solvent.[174-175] The presence of nonpolar solvent in the solution, however, forces NPs to be used only in the inverted structure in the same manner as sol-gel or sputtering processed ZnO. Therefore, it is of great importance to improve colloidal stability of ZnO NPs in polar solvent to improve a versatility of the NPs in device applications. Methanol is one of the best candidates as an appropriate solvent for the NPs to form a thin film on organic layer with least damages, due to its solvent orthogonality and high volatility.[176-178] Li et at. reported methanol treatment on PTB7-Th:$PC_{71}BM$ blend could rearrange the blend morphology toward favorable morphology and achieved the enhanced power conversion efficiency (PCE) by 9.8%.[176] Guo et al.[177] tested alcohol treatment on the active blend using various alcohols of methanol, ethanol, 2-propanol, and 1-butanol. Among them, methanol efficiently reconstructed the inner structure of the blend and altered the energy level at the interfaces between the active layer and the top electrode for better charge extraction. Based on the previous studies, it is expected that ZnO NPs in methanol would possess the advantages of both materials; methanol reconstructs the molecular packing of the active layer toward better morphology and ZnO NPs act as an efficient electron transport layer in the device. Despite of the prescribed advantages, poor colloidal

stability of ZnO NPs in methanol frustrates their applications in the organic optoelectronics with conventional structure and comprehensive studies on improving colloidal stability of ZnO NPs in methanol solvent have been hardly studied so far.

In this manuscript, we report the greatly improved colloidal stability of ZnO NPs in methanol by adding coordination complex, titanium diisopropoxide bis(acetylacetonate) (Ti(acac)) as an efficient stabilizer. Metal acetylacetonates have been widely used as efficient metal precursor to synthesize metal nanoparticles. But few studies have provided systematic analysis on metal acetylacetonates as a stabilizer. We find that Ti(acac) is readily dissociated in methanol and forms Zn-acac bonds at the surface of ZnO NPs and Ti element, from Ti(acac), exists as Ti^{4+} state in oxide lattice. Additional electrons provided by Ti atoms effectively filled up deep trap levels, which results in the reduction of green luminescence from the NPs. In addition, acac functionalized ZnO NPs (fZnOs) exhibit significantly reduced aggregation between NPs in methanol and show long-term (for months) colloidal stability not only in methanol, but also in isopropanol and even nonpolar solvent such as chlorobenzene. Superior colloidal stability of fZnOs was further proved in polymer solar cell applications. PTB7-Th:$PC_{71}BM$[179] devices using 2 months-aged pristine ZnOs (pZnOs) resulted in significantly decreased power conversion efficiency by 38.4%, compared to the devices with as-prepared pZnOs, which is attributed to the aggregation of the NPs. While, the devices with as-prepared and 2 months-aged fZnO exhibited nearly identical power conversion efficiency. The results provide simple and efficient routes to improve colloidal stability of metal nanoparticles and extend their applications to a variety of device structures of organic (opto)electronic devices.

7.2 Experimental details

Materials

All reagents were purchased from Aldrich, Alfa Aesar, or TCI Korea and used without further purification. [6,6]-Phenyl-C71-butyric acid methyl ester (PCBM) was purchased from Organic Semiconductor Materials (OSM, Republic of Korea). 3,9-bis(2-methylene-(3-(1,1-dicyanomethylene)-indanone))-5,5,11,11-tetrakis(4-hexylphenyl)-dithieno- [2,3-d:2′,3′-d′]-s-indaceno[1,2-b:5,6-b′]dithiophene (ITIC), Poly[4,8-bis(5-(2-ethylhexyl)thiophen-2-yl)benzo[1,2-b;4,5-b']dithiophene-2,6-diyl-alt-(4-(2-ethylhexyl)-3-fluorothieno[3,4-b]thiophene-)-2-carboxylate-2-6-diyl)] (PTB7-Th), IEICO-4F, Poly[(2,6-(4,8-bis(5-(2-ethylhexyl)thiophen-2-yl)-benzo[1,2-b:4,5-b']dithiophene))-alt-(5,5-(1',3'-di-2-thienyl-5',7'-bis(2-ethylhexyl)benzo[1',2'-c:4',5'-c']dithiophene-4,8-dione)] (PBDB-T) and 3,9-bis(2-methylene-((3-(1,1-dicyanomethylene)-6/7-methyl)-indanone))-5,5,11,11-tetrakis(4-hexylphenyl)-dithieno[2,3-d:2',3'-d']-s-indaceno[1,2-b:5,6-b']dithiophene (IT-M) were purchased from 1-Material.

ZnO nanoparticle synthesis

ZnO NP solutions were prepared using the method reported elsewhere with a slight modificatoin. [1, 2] Briefly, Zinc acetate dihydrate (2.95 g, 13.4 mmol) was dissolved in 135 mL of methanol at 60 ℃. KOH solution (26.7 mmol of KOH in 55 mL methanol) was added dropwise to the zinc acetate solution under vigorous stirring and kept at 60 ℃ for 2 hours and 15 minutes. As-synthesized ZnO NPs were precipitated by centrifugation and washed twice using methanol. The precipitants were finally dispersed in methanol at high concentration as a stock solution (20 ~ 50 mg/mL). Before using it, the stock solution was diluted to the desired concentration (5~20 mg/mL).

Material Characterization

UV-vis absorption spectra were obtained in the wavelength range of 200 to 800 nm using an Agilent Cary 5000 UV-Vis-NIR spectrometer at room temperature. PL spectra were recorded between 350 to 800 nm wavelength using a Varian Cary Eclipse fluorescence spectrophotometer at room temperature. Highly diluted solutions were prepared in 1 cm path-length quartz cuvettes in order not to exceed the highest possible intensity measured in the instruments, mostly occurs at short wavelengths. XPS spectra were collected using a Thermo Fisher scientific ESCALAB250XI with a monochromated Al-Kα X-ray source at a base pressure of 1.0×10^{-9} Torr. The samples were prepared by spin-coating onto 80 nm gold films on Si substrates with room condition. XRD measurement was carried out using a Bruker AXS D8 Advance X-ray Diffractometer with CuKα radiation. The samples were examined in the range of 20 to 80° by 0.02° (2θ) and the scan rate is 2.4° min^{-1}. AFM height and phase images were taken with a Veeco DI-3100 AFM microscope in the tapping mode. The samples were prepared by spin-coating on ITO

substrate. FT-IR absorption spectra were recorded on Varian 670 / 620 FT-IR Microscopes in ATR mode. The samples were diluted in MeOH before the measurement. The TEM images were collected by JEOL JEM-2100F Field Emission Electron Microscope. The samples were prepared by a drop-dry method on carbon-coated copper grids.

Device fabrication and characterization

Polymer solar cells were fabricated with conventional structure. ITO patterned glass substrates were sequentially cleaned with distilled water, acetone, and isopropanol by ultrasonication for 10 min. The substrates were dried at 100 ℃ overnight. PEDOT:PSS (AI4083) was spin-coated onto the cleaned ITO substrate and annealed at 140°C for 10min.

For PTB7-Th:$PC_{71}BM$ based devices, the mixture of donor and acceptor with a 1:1.5 weight ratio (11mg/ml) were dissolved in chlorobenzene (CB) :diphenyl ether (DPE) (97:3 v/v). Two non-fullerene blend solutions were prepared with a 1:1.25 weight ratio (12 mg/ml) dissolved in CB:1-chloronaphthalene (CN) (98:2 v/v) and 1:1 weight ratio (11 mg/ml) in CB:1,8-diiodooctane (DIO) (99.5:0.5 v/v) for PTB7-Th:IEICO-4F and PBDB-T:IT-M, respectively. The solutions were magnetically stirred for 3h at 60 ℃. The polymeric blend solutions were spin-cast onto PEDOT:PSS layer in a nitrogen (N_2)-filled glove box. Especially, PBDB-T:IT-M layer was annealed at 100 ºC for 10 min. after spin-cast. ZnO NP solutions were spin-coated on the photoactive layer. Subsequently, the device was pumped down under vacuum ($<10^{-6}$ Torr), and Ag (85 nm, for PTB7-Th:$PC_{71}BM$) and Al (100 nm, for PTB7-TH:IEICO-4F and PBDB-T:IT-M) were deposited by thermal evaporation. J-V characteristics of the devices were obtained using a Keithley 2635A source measure unit in the N_2 filled glove box. A mask (3.51mm^2) made of a thin metal was attached to each cell before characterization under AM 1.5G illumination at 100mW cm^{-2}. EQE of the devices were determined using a PV Measurements QE system using monochromatic light from a xenon lamp under ambient conditions. The monochromatic light was chopped at 100Hz, and the intensity was calibrated relative to a standard Si photodiode.

7.3 Results and discussion

For the preparation of stable ZnO NP solutions in methanol, 20.5 μM, 41.0 μM, and 82.0 μM of Ti(acac) was added to the ZnO NP solutions which were prepared by using previously reported method.[180-181] The detailed procedure can be found in Supporting Information. In the following, each functionalized ZnO NP solution is denoted as fZnO-L, fZnO-M, and fZnO-H (low, mid, and high in concentration), respectively. ZnO NP solution without Ti(acac) was also studied as a reference (denoted as pZnO – pristine ZnO NPs).

Figure 7.1a shows photographs of the prepared solutions with three different Ti(acac) concentrations. As-prepared pZnOs were translucent and easily filtered via 0.45 μm pore-sized PTFE filter. The addition of Ti(acac) with three different concentration (low, mid, and high) made the solutions transparent. 2 weeks later, pZnO showed milky suspension, implying that strong aggregation occurred between NPs because of their high surface energy, while fZnO-L, M, and H maintained its high transparency. This observation suggests that the addition of Ti(acac) successfully prevents NPs from the aggregation in methanol solvent. **Figure 7.1b** exhibits the UV-Vis absorption spectra of the solutions with different Ti(acac) concentrations. Absorption onset of the reference solution was 368 nm, corresponding to 3.37 eV of optical bandgap. The addition of Ti(acac) led to blueshift of absorption onset to 361 nm (3.43 eV) for fZnO-L and M, and 359 nm (3.45 eV) for fZnO-H. The slight widening in bandgap is due to weak quantum confinement of ZnO nanoparticles, caused by a loss of bulk properties after the segregation, as well as reduced light scattering by NP agglomerates.[182]

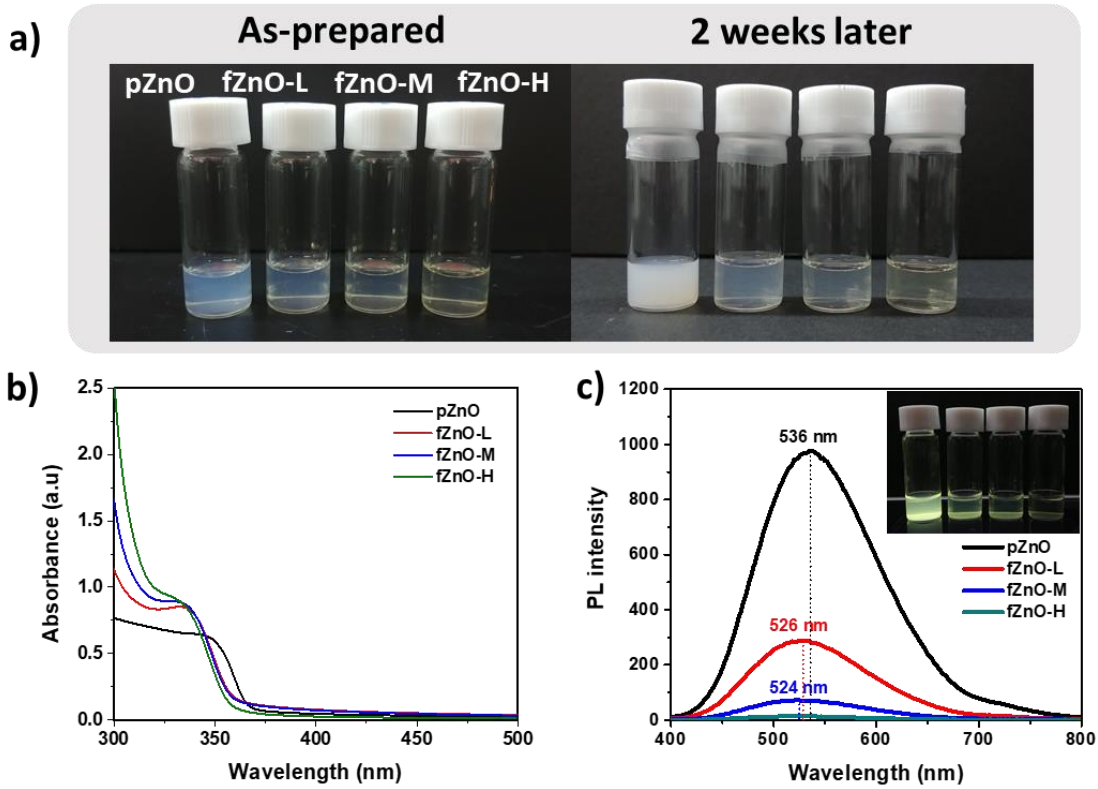

Figure 7. 1. Stabilized ZnO NP solutions after the addition of Ti(acac). a) photographs of ZnO NP solutions dispersed in MeOH. b) UV-vis absorption and c) photoluminescence spectra of ZnO NP solutions.

Figure 7.2 shows that pZnO exhibits stronger light scattering over whole wavelengths as it is stored longer, while fZnOs maintain sharp absorption onset. Same tendency was observed in photoluminescence (PL) spectra in **Figure 1c**. As increasing the concentration of Ti(acac), PL peak at 536 nm was blue-shifted to 524 nm with decreasing the peak intensity and finally disappeared in fZnO-H. Despite the fact that its exact origin is still under debates,[183-186] green luminescence (GL) of ZnO is generally attributed to point defects which introduce deep level traps inside band gap. The decreases in the peak intensity could be attributed to filling up of the deep level states by providing additional electrons of substitutional Ti atoms in the lattice or at the surface. Later, we discuss in detail whether Ti is actually involved in ZnO NPs via X-ray photoemission spectroscopy (XPS).

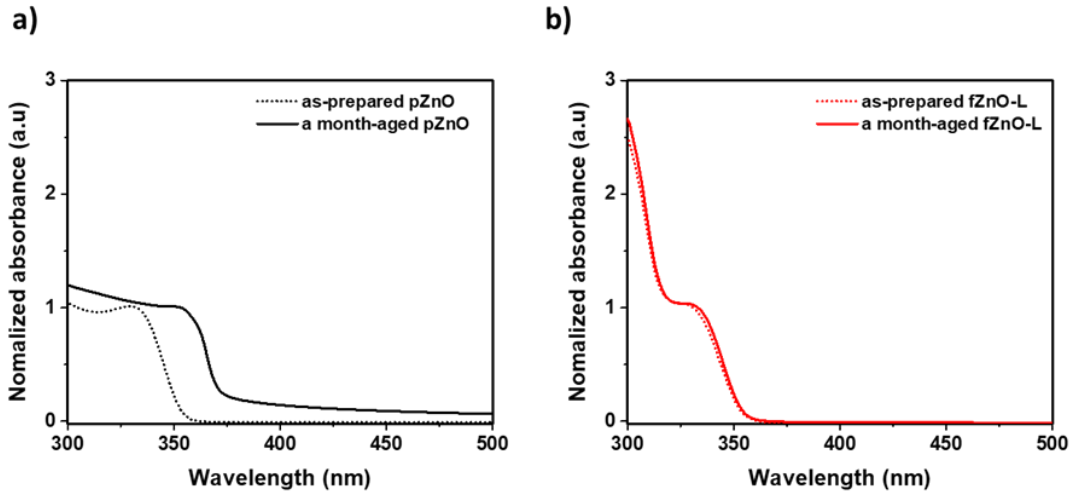

Figure 7. 2. Comparison of UV-vis absorption spectra of (a) pZnO and (b) fZnO under ambient conditions (25℃ and 50-70% RH) for a month.

Same tendency was observed in digital images of the NPs dispersed in less and nonpolar solvents such as isopropanol and chlorobenzene (**Figure 7.3**).

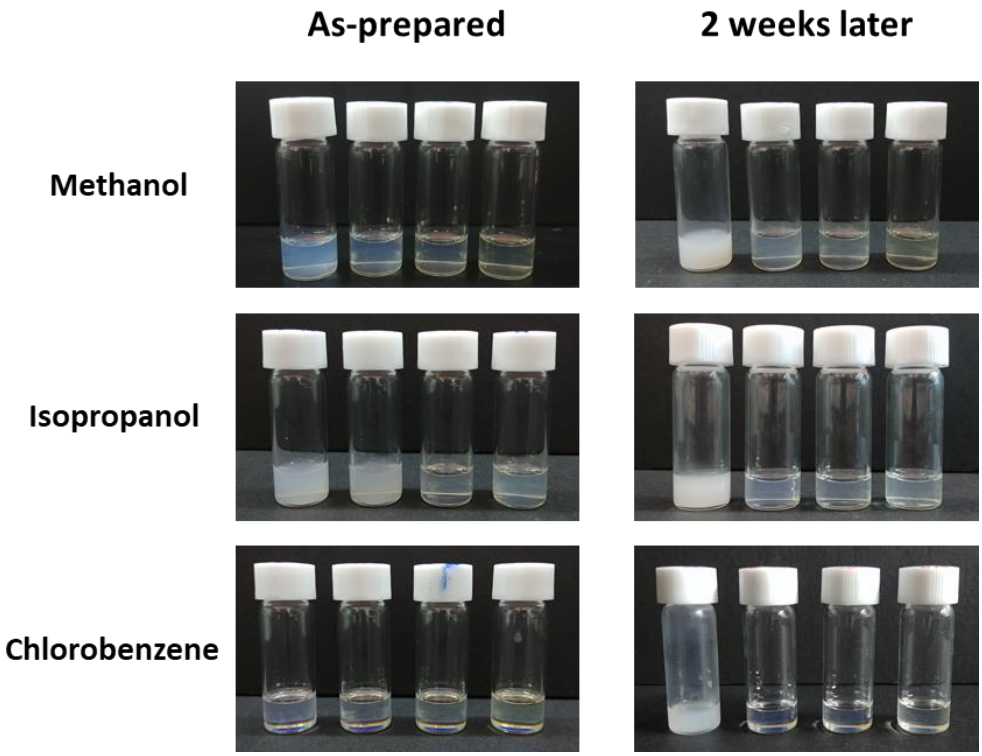

Figure 7. 3. Colloidal stability of ZnO NPs in a variety of solvents.

The influence of Ti(acac) on ZnO NPs at the atomic scale was investigated via transmission electron microscope (TEM, **Figure 7.4a**). For pristine NPs, it was observed that dozens of spherical NPs formed

huge agglomerates. While, the addition of Ti(acac) triggered to reduce the degree of aggregation and each NP was homogeneously distributed throughout the images for fZnOs. Magnified images, shown as inset in each image, reveals that the size and shape of NPs were maintained regardless of the Ti(acac) concentration. **Figure 7.4b** represents the X-ray diffraction (XRD) patterns of ZnO NPs. Strong and well-defined diffraction patterns of reference NPs at 2θ = 31.8°, 34.4°, 36.3°, 47.5°, 56.6°, 62.9°, and 68.0° correspond to (100), (002), (101), (102), (110), (103), and, (112) of Wurtzite ZnO, respectively. As increasing the concentration of Ti(acac), the peaks became weaker and broader, which was commonly observed in nanostructures compared to its bulk counterpart. While, the peaks were observed at same positions, regardless of Ti(acac) treatment.

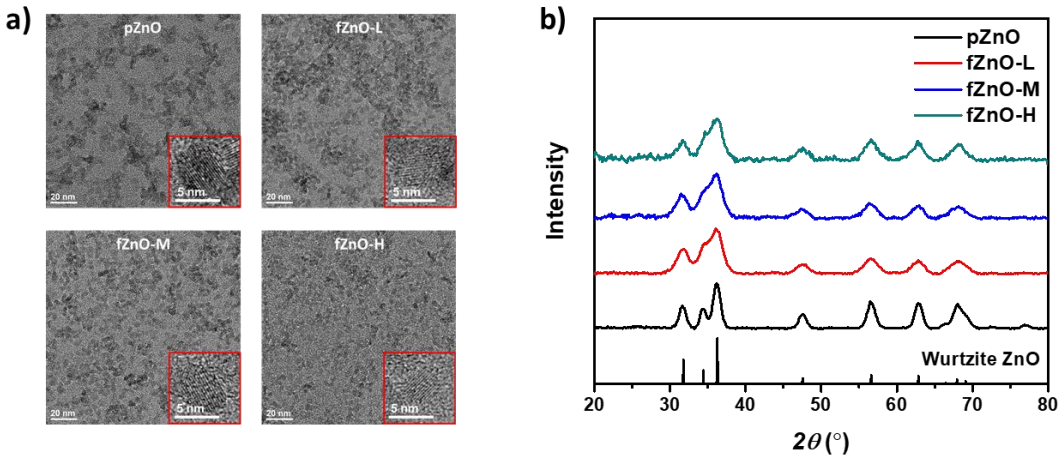

Figure 7. 4. Transmission electron microscope images and X-ray diffraction patterns of Ti(acac) treated ZnO NPs (Inset: magnified images of individual nanoparticles).

In **Figure 7.5**, reduced surface RMS roughness of fZnO thin films to less than a half (2.10, 1.54, and 1.26 nm for fZnO-L, fZnO-M, and fZnO-H, respectively), compared to pZnO thin film (4.01 nm) further proves the effectiveness of Ti(acac) to prevent NPs from interparticle attraction.

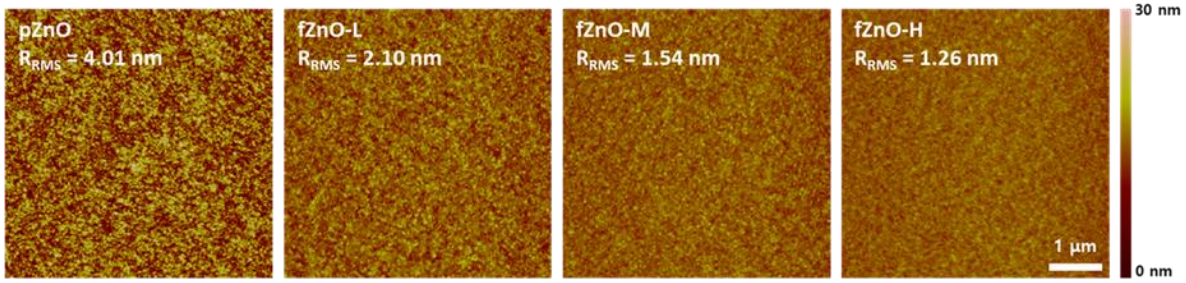

Figure 7. 5. Atomic force microscope topographs of ZnO thin films prepared on ITO substrates using Ti(acac) treated ZnO NPs.

IR spectroscopy is an efficient tool to characterize the organic-functionalized surface of inorganic NPs. In order to identify interactions between Ti(acac) and the surface of ZnO NPs, IR spectra of pZnO, fZnO-L, M, and H are collected and compared in **Figure 7.6a**. Two weak vibrational bands of pZnO were observed at ~1570 cm^{-1}, ~1420 cm^{-1}, which is attributed to the residual acetate ligands on the surface of pZnO. For three fZnOs, strong vibrational bands were observed at 1586, 1520, and 1437 cm^{-1}, which correspond to the C=O and C=C vibrational bands of zinc acetylacetonate (Zn(acac)),[187-188] with a slight spectral shift to lower wavenumbers. The shift can be caused by lengthened bond length of Zn-O at the surface of the NPs compared to tightly bound metal-ligand bond in Zn(acac) complex.[187, 189] Nearly identical IR intensities of fZnO-M and H at three bands reveals that the amount of acetylacetonates on the surface of the NPs is likely to be saturated after 41 uM of Ti(acac) addition.

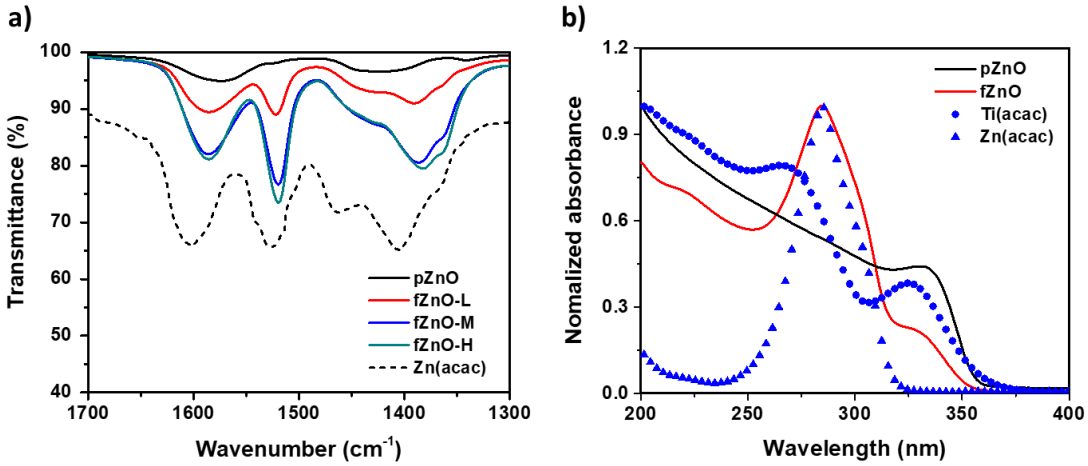

Figure 7. 6. (a) IR spectra of Ti(acac) treated ZnO NPs. Dashed line exhibits the spectrum of Zn(acac) taken from reference 31. (b) UV-vis absorption spectra of pZnO, fZnO, Zn(acac), and Ti(acac) at UV region.

It is found that fZnOs exhibit reduced surface hydroxyl groups (broad vibrational band around 3400 cm^{-1}, see **Figure 7.7**) as increasing the concentration of Ti(acac).

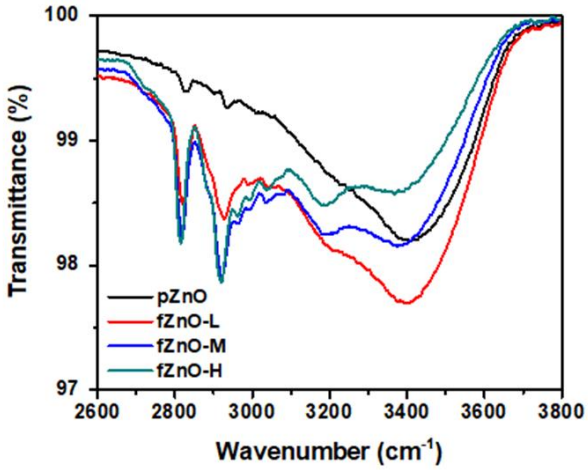

Figure 7. 7. FT-IR spectra of Ti(acac) treated ZnO NPs in the range between 2600 and 3800 cm^{-1}.

The strong correlation between surface RMS roughness and IR intensity at three featured vibrational bands (**Figure 7.8**) supports our statement that reduced NP aggregation is mainly due to surface functionalization of ZnO NPs by Ti(acac). It is noteworthy that most metal acetylacetonate complexes exhibit similar IR responses,[190-191] which may give rise to the concerns that the collected vibrational bands might arises from Ti(acac) rather than new Zn-(acac) bonds formed at the Zn rich surface of the NPs. Yet, strong doublet peaks around 1600 cm^{-1}, which is a distinct feature of Ti(acac), were not observed in **Figure 7.6a**. This suggests that Ti(acac) is dissolved in methanol in the form of Ti^{4+} and bidentate $(acac)^-$ ligands, which is, then, attached to the surface of the NPs. The dissociation of Ti(acac) and the formation of Zn(acac) in fZnOs were further confirmed in **Figure 7.6b**. Two strong absorption peaks of Ti(acac) at 270.5 and 324.5 nm are not shown in fZnO spectrum. Rather, its strong absorption at 285 nm corresponds to distinct absorption feature of Zn(acac). The feature from Zn(acac) explains strong light absorption of fZnOs in the wavelengths below 320 nm, shown in **Figure 7.1b**. This result is consistent with the discussion on **Figure 7.6a**.

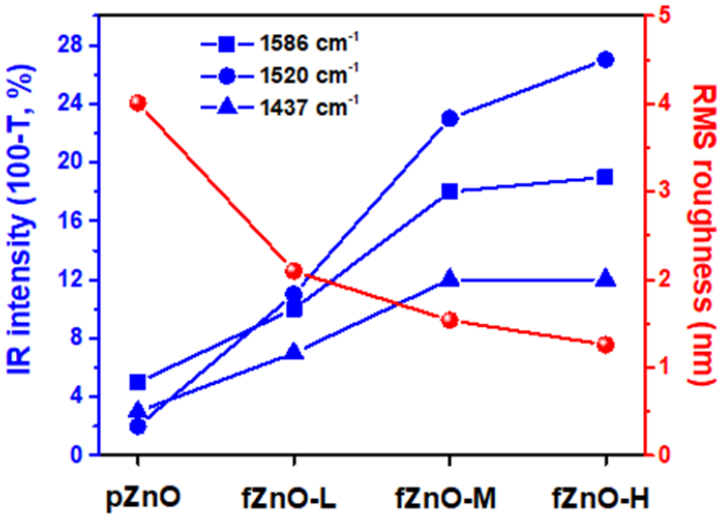

Figure 7. 8. The relation between IR intensities and RMS roughness of Ti(acac) treated ZnO NPs.

X-ray photoelectron spectroscopy was carried out to characterize chemical composition of the processed ZnO thin films. O1s spectra in **Figure 7.9** exhibit two peaks at 531.5 and 530.0 eV. The former corresponds to surface hydroxyl group of ZnO and the latter to Zn-O bond in the lattice.[192] Increasing intensities at 531.5 eV was observed as increasing the concentration of Ti(acac), which possibly be interpreted as a result of increased number of surface OH^- group. However, it is controversial to the observation of reduced OH groups in fZnO samples as shown in **Figure 7.7**. Another possible explanation is based on the fact that Ti-O bond in Ti doped ZnO is also observed at 531.5 eV.[193-194] It is found that Ti atoms are involved in the thin film as two sharp peaks at 464.0 and 458.3 eV were shown in Ti 2p spectra, which corresponds to Ti $2p_{1/2}$ and $2p_{3/2}$ peaks of TiO_2. Moreover, a slight shift of peaks to higher binding energy in Zn 2p spectra is possibly due to the de-shielding of positive charge of Zn nucleus caused by strong attractive force of substitutional Ti atoms to Zn core electrons, resulting in increased binding energy. From XPS results, it is found that Ti atoms are involved in the ZnO thin film and affect to the electronic structure of ZnO thin film, which is also confirmed via reduced PL intensities in **Figure 7.1c**. Yet, it is not certain whether Ti is actually positioned at the surface of the NPs or inside the oxide lattice. A further study with more focus on it is therefore required.

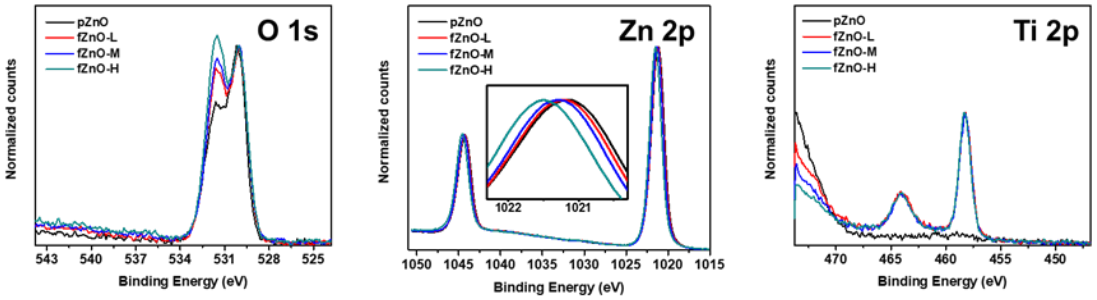

Figure 7. 9. X-ray photoelectron spectra of Ti(acac) treated ZnO NP thin film prepared on Au coated silicon substrate.

We fabricated PTB7-Th:$PC_{71}BM$ based bulk heterojunction solar cells using p- and fZnOs. The device structure comprises sequential deposition of ITO/PEDOT:PSS/PTB7-Th:$PC_{71}BM$/ZnO/Ag. ZnO layer was prepared using 5 mg/ml of ZnO NP solutions. Ag was intentionally used as top metal electrode to introduce energy level mismatch in the device where electron transfer from the active layer to Ag is energetically not favorable. The mismatch is corrected only when ZnO works as electron transport layer properly. *J-V* characteristics of the device with p- and fZnO are shown in **Figure 7.10a** and **b**, respectively. Photovoltaic parameters of the devices are summarized in **Table 7.1**.

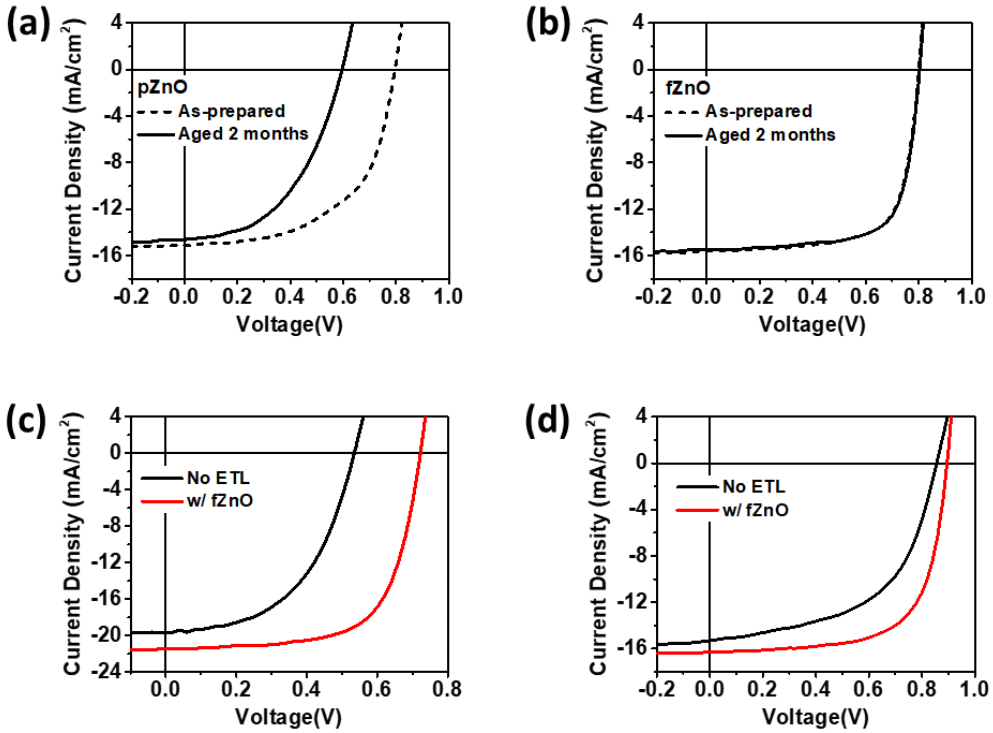

Figure 7. 10. *J-V* characteristics of polymer solar cells based on three different polymeric blends. PTB7-Th:$PC_{71}BM$ based polymer solar cells using (a) pristine and (b) Ti(acac) treated ZnO NPs as ETLs. (c) PTB7-Th:IEICO-4F and (d) PBDB-T:IT-M based polymer solar cells with Ti(acac) treated ZnO NPs as efficient ETLs.

Table 7. 1. Summary of photovoltaic parameters of PTB7-Th:$PC_{71}BM$ based polymer solar cells.

ETL	Aging	J_{SC} [mA cm^{-2}]	V_{OC} [V]	*FF*	PCE [%]
pZnO	As-prepared	15.12 (14.90±0.22)	0.80 (0.80±0.00)	0.56 (0.55±0.01)	7.09 (6.87±0.14)
	2 months	14.63 (14.49±0.23)	0.60 (0.58±0.01)	0.48 (0.47±0.01)	4.37 (4.14±0.14)
fZnO	As-prepared	15.63 (15.24±0.28)	0.80 (0.80±0.00)	0.71 (0.71±0.01)	9.32 (9.07±0.15)
	2 months	15.49 (15.04±0.30)	0.80 (0.80±0.00)	0.72 (0.71±0.01)	9.32 (9.03±0.21)

When as-prepared NPs were used in the device, fZnO devices exhibited higher performance compared to the device with pZnO, especially in J_{SC} (15.12 -> 15.63 mA/cm^2), and *FF* (0.56 -> 0.71). It may be attributed to passivated deep level traps of fZnOs by Ti, which results in reduced charge carrier recombination at the blend/ZnO interface.[195] We confirmed colloidal stability of ZnO by aging NPs for 2 months in ambient condition. The devices with aged pZnO exhibited significant reduction in all three parameters, resulting in decreased power conversion efficiency (PCE) by 38.4%. It is ascribed to the strong aggregation in the aged NP solutions as confirmed in **Figure 7.1** and **7.4**. The aggregation causes ZnO thin film with poor coverage on the active layer at low concentration and V_{OC} of the devices significantly decrease by the direct contact of partially exposed active layer with energetically mismatched Ag electrode. Interestingly, it is apparent from **Figure 7.10b** that fZnO devices maintained nearly identical *J-V* characteristics. The summarized device parameters, shown in **Table 7.1**, prove that improved colloidal stability of fZnO enables negligible change in the quality of ZnO thin film despite 2 months aging under ambient condition. Efficient electron transporting ability of fZnO was further confirmed by fabricating polymer solar cells using two peculiar polymeric blend, PTB7-Th:IEICO-4F[196] and PBDB-T:IT-M,[197] which the former exhibits high J_{SC} and the latter exhibits high V_{OC}. For two devices, Al electrode was adopted instead of Ag electrode for the better energy level alignment in conventional structure. *J-V* characteristics of PTB7-Th:IEICO-4F and PBDB-T:IT-M based solar cells are shown in **Figure 7.10c** and **d**, respectively, and the parameters are summarized in **Table 7.2**. PTB7-Th:IEICO-4F blend exhibited strong dependence on the presence of ZnO layer. The enhancement was particularly pronounced in V_{OC} (0.53 -> 0.72 V) and *FF* (0.48 -> 0.66), which is commonly observed in nonfullerene based polymer solar cells without ETL. The use of ZnO boosted averaged PCE from 4.67 to 10.49% corresponding to ~125% enhancement. 10.80% of high PCE was achieved at optimal condition. While, PBDB-T:IT-M devices exhibited less dependence on ZnO layer compared to PTB7-

Th:IEICO-4F based devices, but still considerable performance enhancement. 10.28% of the best PCE was achieved at optimal condition with 9.81% of averaged PCE corresponding to 38% enhancement. External quantum efficiencies from the corresponding devices can be seen in **Figure 7.11**. Integrated J_{SC}s of each device, deduced from the spectra, are well consistent with those shown in **Figure 7.10**.

Table 7. 2. Summary of photovoltaic parameters for PTB7:IEICO-4F and PBDB-T:IT-M based polymer solar cells.

Active layer	ETL	J_{SC} [mA cm^{-2}]	V_{OC} [V]	*FF*	PCE [%]
PTB7-Th:IEICO-4F	**X**	19.07 (17.48±1.68)	0.54 (0.53±0.05)	0.52 (0.48±0.06)	5.57 (4.67±0.88)
	fZnO	21.49 (21.07±0.32)	0.72 (0.72±0.00)	0.67 (0.66±0.01)	10.80 (10.49±0.19)
PBDB-T:IT-M	**X**	15.32 (15.35±0.33)	0.86 (0.85±0.00)	0.54 (0.52±0.01)	7.45 (7.12±0.24)
	fZnO	16.29 (15.80±0.34)	0.90 (0.90±0.00)	0.67 (0.66±0.01)	10.28 (9.81±0.23)

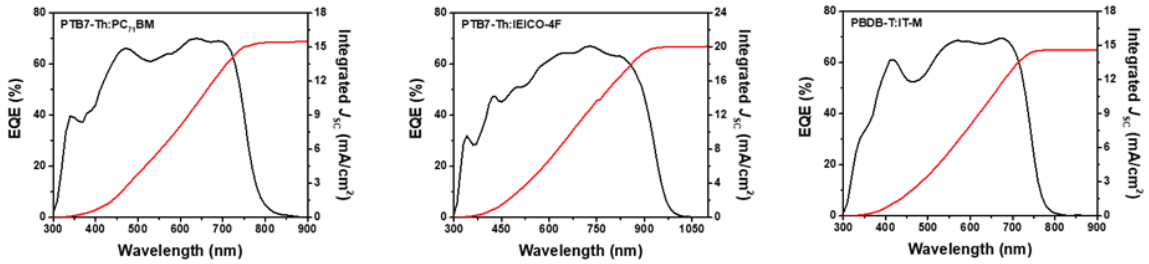

Figure 7. 11. External quantum efficiency of polymer solar cells with three different polymeric blends at optimal condition.

7.4 Conclusion

In conclusion, a coordination complex, Ti(acac), was employed as an efficient stabilizer in ZnO NP dispersed in methanol. The surfaces of the NPs were successfully functionalized with acac, which effectively reduced agglomerates of the nanoparticles confirmed by TEM images. The suppression of agglomerates formation in the NP solutions led to smoother surface roughnesses of ZnO thin films. Tetravalent Ti atoms in ZnO lattice passivated deep-level traps of the NPs, which led to significant reduction in green luminescence. It was also found that Ti(acac) exhibited its functionality even in other solvents with different polarities such as isopropanol and chlorobenzene. fZnO was then employed to the polymer solar cells with three different polymeric blends. PTB7-Th:$PC_{71}BM$ devices using as-prepared and aged fZnO were compared and exhibited nearly identical *J-V* characteristics. The versatility of fZnO was further proved in two nonfullerene polymeric blends, PTB7-Th:IEICO-4F and PBDB-T:IT-M. We found that fZnO works as an efficient electron transport layer in both devices without deteriorating optimized polymeric blends morphology.

We demonstrated simple and universal method to improve colloidal stability of ZnO nanoparticles and successfully applied them to the polymer solar cells with conventional structure, proving long-term stability of ZnO nanoparticle solution. Cheap, robust, and stable ZnO NPs dispersed in methanol will provide availability of conventional structure for highly stable and efficient polymer solar cells, which have been mostly achieved in inverted structure so far. Furthermore, the availability of the method in solvent with opposite polarity provides their potential applications in perovskite solar cells.

CHAPTER 8. Summary

In the thesis, newly developed solution-processing methods for highly efficient oxide and sulfide thin films were discussed from their synthesis to device applications.

For oxide thin films, less perilous 2-methoxyethanol was utilized as a solvent for metal precursors. Hafnium and zirconium isopropoxides and tantalum ethoxide were readily dissolved in 2-methoxyethanol followed by subsequent ligand exchange of metal alkoxides to metal 2-methoxyethoxides. Spincoating the precursor solutions in N_2 atmosphere effectively suppressed the solution from a violent reaction with O_2 and H_2O. And thermal annealing of the prepared samples in ambient air led to condensation and densification of the films, resulting in amorphous metal oxide thin films. 5.89, 5.48, and 4.67 eV of wide band gap were observed in HfO_2, ZrO_2, and Ta_2O_5 thin films, respectively, which show their potential application to transparent electronic devices. The optimized processing allowed the oxide films to achieve atomic scale smooth surface rms roughness < 0.2 nm, which is a vital factor for the efficient charge carrier transport in thin film transistors. Thin film transistors were fabricated using the oxide dielectrics. The devices exhibit comparable carrier mobilities with those of the devices using SiO_2 gate dielectrics, while significantly reduced operating voltage by 95%. The results introduce a simple and chemically less toxic approach for metal oxide preparation and suggest their potential for applications to low-power electronic device.

In chapter 4 and 5, I introduced a facile solution-processable method for sulfide thin films. The idea was that tertiary butoxycarbonyl groups are often utilized thermally cleavable agents on polymers, I designed thermally cleavable metal thiolates as sulfide precursors. Metal thiolates were synthesized by simple mixing of metal acetate or isopropoxide with tertiary dodecane (or nonane) thiols. Rapid acid-base reaction readily led to the formation of metal thiolates, and acetic acid or isopropanol as byproducts. Metal thiolate solutions were solution-processed on prepared substrates and thermally annealed to promote cleavages of the precursors. X-ray photoelectron spectra of the thin films identified that the films were successfully turned out to be metal sulfides. Weight losses during the transition was consistent to the mass loss from thiolate compounds to the expected metal sulfides. Chemical analysis on byproducts during thermal annealing revealed that the byproduct is a dialkylsulfide which is formed when the reaction is SN_1 reaction. Furthermore, there was no carbon residue in the resultant sulfide films. It was found that the ternary and quaternary sulfide compounds could be prepared by simply mixing metal thiolate precursors with a desired molar ratio. The sulfide films were applied to thin film

transistors and solar cells. CdS transistor exhibited 61 cm^2/Vs of extremely high electron mobility with high I_{ON}/I_{OFF} ratio of > 10^5. CuInS2 solar cells were fabricated by mixing Cu and In thiolate precursors with 1:1 molar ratio. The device exhibited 1.11% and 1.53% of power conversion efficiency in the structures, ITO/ZnO/CdS/$CuInS_2$/MoO_3/Au and ITO/$CuInS_2$/CdS/ZnO/Al, respectively. Relatively low power conversion efficiencies may be attributed to the poor crystallinity of selenization-less $CuInS_2$ layer and energetically unoptimized device structures. These reports marked, for the first time, the preparation of non-toxic solution processable sulfide thin films from nonpolar ink with a clarified decomposition chemistry.

Last two chapters moved our attention to metal oxide nanoparticles that are an alternative way to form metal oxide thin films via solution processing. In chapter 6, we focused on utilizing an advantage of nanoparticle approach that there needs no or little thermal annealing to form a thin film. Two-dimensional array of Ag quantum dots was applied to polymer solar cells to improve short-circuit current density of the devices using localized surface plasmon resonance. To make an efficient electron transport pathway to an anode, indium tin oxide (ITO), ZnO and TiO_2 nanoparticles were synthesized and coated on Ag quantum dots. It is found that high refractive index of TiO_2 induced redshift of LSPR peak of Ag quantum dots compared to that of the dots surrounded by ZnO. Calculated extinction spectra via discrete dipole approximation method was also consistent with the results. Duplication of the experimental results was possible when the calculation is under two assumptions that the dielectric function follows Drude-Sommerfeld model and the incident photon – conduction electron interaction is affected by neighboring quantum dots. In the polymer solar cells, both ZnO and TiO_2 devices exhibited similar J-V characteristics with negligible photovoltaic parameters when plasmonic enhancement was not considered. However, two-dimensional Ag quantum dot array significantly improved power conversion efficiency of the devices especially in the case of TiO_2. In order to find out the underlying physics on the improvement, near-field enhancement and far-field scattering by the quantum dots were calculated. In the near-field distribution, it was found that the dipolar excitation of the localized surface plasmon in the vicinity of the quantum dots were confined to the extremely local region, which are not reach to the active layer of the devices in both cases. However directional far-field scattering of incident photons to the active layer by the quantum dots were observed in both cases, especially stronger in TiO_2 case. This observation was well consistent with the experimental results. I found that ZnO and TiO_2 nanoparticles could be a good choice for the formation of electron transport layer on Ag quantum dots with least amount of damage. As a result, the device performance was successfully enhanced by utilizing plasmonic phenomenon of Ag quantum dots.

Finally, a simple and efficient strategy to improve colloidal stability of ZnO nanoparticles was demonstrated in chapter 7. Titanium diisopropoxide bis(acetylacetonate) (Ti(acac)) was added, as a

stabilizer, to the nanoparticles dispersed in methanol. The coordination complex was readily dissociated in methanol and formed new Zn-acac bond at the surface of the nanoparticles. UV-vis absorption in the regions from 200 to 400 nm wavelengths and FT-IR spectra exhibited that Ti(acac) is completely dissociated and Zn(acac) is formed. The surface functionalization led to the segregation of ZnO agglomerates naturally formed in the solution. XPS identified that Ti is involved in ZnO lattice and it provides additional electrons to ZnO, resulting in a passivation of deep level traps of ZnO. The trap passivation was further confirmed in the reduced green luminescence of the coordination complex treated ZnO nanoparticles. Interestingly, it is found that the method is also applicable in other solvents such as isopropanol and chlorobenzene. The colloidal stability of Ti(acac) treated ZnO nanoparticle solutions were verified in the device application. Two ZnO samples, that one is fresh and the other is 2 months aged under ambient air, showed nearly identical power conversion efficiency of polymer solar cells. At optimal condition, 10.80% of the highest power conversion efficiency was achieved in PTB7-Th:IEICO-4F solar cells. The universal approach for high colloidal stability ZnO nanoparticle enables structure-independent preparation of device-grade ZnO thin films and provides more chances for researchers to improve the performance of optoelectronic devices.

I have demonstrated solution-processing strategies of oxide and sulfide thin films for optoelectronic device applications. For sol-gel approach, the precursors were designed focusing on 1) environmentally friendly synthetic scheme, 2) simple preparation, and 3) carbon-free products while maintaining their thin film qualities. In the case of nanocrystal approach, I have tried to apply them to polymer solar cells as efficient electron transport layers by considering its advantage that no post treatment is required to form a target thin film. Both sol-gel and nanocrystal methods have their own advantages and the projects introduced in the thesis have utilized the methods under the consideration. It will offer a great potential for macroelectronic device application in preparing oxide and sulfide thin films with dramatically reduced processing cost and additional process flexibility.

References

(1) Razavi, B., *Design of Analog CMOS Integrated Circuits*. McGraw-Hill, Inc.: 2001; p 704.

(2) Emilio, M. D. P., *Data Acquisition Systems: From Fundamentals to Applied Design*. Springer Publishing Company, Incorporated: 2013; p 152.

(3) Di Paolo Emilio, M., Review of Microelectronics. In *Microelectronics: From Fundamentals to Applied Design*, Springer International Publishing: Cham, 2016; pp 1-18.

(4) Johansen, I.; Arntzen, R.; Bergmann, S.; Husa, S.; Ingebrigtsen, K. A.; Johannessen, J. S.; Sandved, J. S., Examples of thin film applications in electronic devices. *Thin Solid Films* **1978,** *50*, 171-185.

(5) Alam, M. A.; Pimparkar, N.; Ray, B., The Future of Microelectronics is … Macroelectronics. *Future Trends in Microelectron.* **2010**.

(6) Fortunato, E.; Barquinha, P.; Martins, R., Oxide Semiconductor Thin-Film Transistors: A Review of Recent Advances. *Adv. Mater.* **2012,** *24*, 2945-2986.

(7) Sheng, J.; Jeong, H.-J.; Han, K.-L.; Hong, T.; Park, J.-S., Review of recent advances in flexible oxide semiconductor thin-film transistors. *J. Inf. Disp.* **2017,** *18*, 159-172.

(8) Azimi, H.; Hou, Y.; Brabec, C. J., Towards low-cost, environmentally friendly printed chalcopyrite and kesterite solar cells. *Energy Environ. Sci.* **2014,** *7*, 1829-1849.

(9) Saran, R.; Curry, R. J., Lead sulphide nanocrystal photodetector technologies. *Nat. Photonics* **2016,** *10*, 81.

(10) Eslamian, M., Inorganic and Organic Solution-Processed Thin Film Devices. *Nano-Micro Lett.* **2016,** *9*, 3.

(11) Pasquarelli, R. M.; Ginley, D. S.; O'Hayre, R., Solution processing of transparent conductors: from flask to film. *Chem. Soc. Rev.* **2011,** *40*, 5406-5441.

(12) Calvert, P., Inkjet Printing for Materials and Devices. *Chem. Mater.* **2001,** *13*, 3299-3305.

(13) Ding, X.; Liu, J.; Harris, T. A. L., A review of the operating limits in slot die coating processes. *AIChE J.* **2016,** *62*, 2508-2524.

(14) Chang, Y.-H.; Tseng, S.-R.; Chen, C.-Y.; Meng, H.-F.; Chen, E.-C.; Horng, S.-F.; Hsu, C.-S., Polymer solar cell by blade coating. *Org. Electron.* **2009,** *10*, 741-746.

(15) Tedde, S. F.; Kern, J.; Sterzl, T.; Fürst, J.; Lugli, P.; Hayden, O., Fully Spray Coated Organic Photodiodes. *Nano Lett.* **2009,** *9*, 980-983.

(16) Sahu, N.; Parija, B.; Panigrahi, S., Fundamental understanding and modeling of spin coating process: A review. *Indian J. Phys.* **2009,** *83*, 493-502.

(17) Song, S.; Lee, K. T.; Koh, C. W.; Shin, H.; Gao, M.; Woo, H. Y.; Vak, D.; Kim, J. Y., Hot slot die

coating for additive-free fabrication of high performance roll-to-roll processed polymer solar cells. *Energy Environ. Sci.* **2018,** *11*, 3248-3255.

(18) Ziemniak, S. E., Metal oxide solubility behavior in high temperature aqueous solutions. *J. Solution Chem.* **1992,** *21*, 745-760.

(19) Kolthoff, I. M., The Solubilities and Solubility Products of Metallic Sulphides in Water. *J. Phys. Chem.* **1930,** *35*, 2711-2721.

(20) Mayer, A. C.; Scully, S. R.; Hardin, B. E.; Rowell, M. W.; McGehee, M. D., Polymer-based solar cells. *Mater. Today* **2007,** *10*, 28-33.

(21) Zhang, Z.; Feng, L.; Xu, S.; Liu, Y.; Peng, H.; Zhang, Z.-G.; Li, Y.; Zou, Y., A New Electron Acceptor with meta-Alkoxyphenyl Side Chain for Fullerene-Free Polymer Solar Cells with 9.3% Efficiency. *Adv. Sci.* **2017,** *4*, 1700152-1700152.

(22) Eastham, N. D.; Logsdon, J. L.; Manley, E. F.; Aldrich, T. J.; Leonardi, M. J.; Wang, G.; Powers-Riggs, N. E.; Young, R. M.; Chen, L. X.; Wasielewski, M. R.; Melkonyan, F. S.; Chang, R. P. H.; Marks, T. J., Hole-Transfer Dependence on Blend Morphology and Energy Level Alignment in Polymer: ITIC Photovoltaic Materials. *Adv. Mater.* **2017,** *30*, 1704263.

(23) Bin, H.; Gao, L.; Zhang, Z.-G.; Yang, Y.; Zhang, Y.; Zhang, C.; Chen, S.; Xue, L.; Yang, C.; Xiao, M.; Li, Y., 11.4% Efficiency non-fullerene polymer solar cells with trialkylsilyl substituted 2D-conjugated polymer as donor. *Nat. Commun.* **2016,** *7*, 13651.

(24) Burkhard, G. F.; Hoke, E. T.; McGehee, M. D., Accounting for Interference, Scattering, and Electrode Absorption to Make Accurate Internal Quantum Efficiency Measurements in Organic and Other Thin Solar Cells. *Adv. Mater.* **2010,** *22*, 3293-3297.

(25) Sah, C. T., A New Semiconductor Tetrode-The Surface-Potential Controlled Transistor. *Proc. IRE* **1961,** *49*, 1623-1634.

(26) Fortunato, E. M. C.; Barquinha, P. M. C.; Pimentel, A. C. M. B. G.; Gonçalves, A. M. F.; Marques, A. J. S.; Pereira, L. M. N.; Martins, R. F. P., Fully Transparent ZnO Thin-Film Transistor Produced at Room Temperature. *Adv. Mater.* **2005,** *17*, 590-594.

(27) Sirringhaus, H.; Brown, P. J.; Friend, R. H.; Nielsen, M. M.; Bechgaard, K.; Langeveld-Voss, B. M. W.; Spiering, A. J. H.; Janssen, R. A. J.; Meijer, E. W.; Herwig, P.; de Leeuw, D. M., Two-dimensional charge transport in self-organized, high-mobility conjugated polymers. *Nature* **1999,** *401*, 685.

(28) Walker, B.; Kim, G.-H.; Heo, J.; Chae, G. J.; Park, J.; Seo, J. H.; Kim, J. Y., Solution-processed CdS transistors with high electron mobility. *RSC Adv.* **2014,** *4*, 3153-3157.

(29) Richard, P. D.; Markunas, R. J.; Lucovsky, G.; Fountain, G. G.; Mansour, A. N.; Tsu, D. V., Remote plasma enhanced CVD deposition of silicon nitride and oxide for gate insulators in (In, Ga)As FET devices. *J. Vac. Sci. Technol. A* **1985,** *3*, 867-872.

(30) Lucovsky, G.; Richard, P. D.; Tsu, D. V.; Lin, S. Y.; Markunas, R. J., Deposition of silicon dioxide

and silicon nitride by remote plasma enhanced chemical vapor deposition. *J. Vac. Sci. Technol. A* **1986,** *4*, 681-688.

(31) Muller, D. A.; Sorsch, T.; Moccio, S.; Baumann, F. H.; Evans-Lutterodt, K.; Timp, G., The electronic structure at the atomic scale of ultrathin gate oxides. *Nature* **1999,** *399*, 758.

(32) Wilk, G. D.; Wallace, R. M.; Anthony, J. M., High-κ gate dielectrics: Current status and materials properties considerations. *J. Appl. Phys.* **2001,** *89*, 5243-5275.

(33) Neaton, J. B.; Muller, D. A.; Ashcroft, N. W., Electronic Properties of the $\mathrm{Si}/{\mathrm{SiO}}_{2}$ Interface from First Principles. *Phys. Rev. Lett.* **2000,** *85*, 1298-1301.

(34) Jamison, P. C.; Tsunoda, T.; Vo, T. A.; Li, J.; Jagannathan, H.; Shinde, S. R.; Paruchuri, V. K.; Gall, D., SiO2 Free HfO2 Gate Dielectrics by Physical Vapor Deposition. *IEEE Trans. Electron Devices* **2015,** *62*, 2878-2882.

(35) Chang, Y. C.; Chang, W. H.; Chang, Y. H.; Kwo, J.; Lin, Y. S.; Hsu, S. H.; Hong, J. M.; Tsai, C. C.; Hong, M., Drain current enhancement and negligible current collapse in GaN MOSFETs with atomic-layer-deposited HfO2 as a gate dielectric. *Microelectron. Eng.* **2010,** *87*, 2042-2045.

(36) Robertson, J., High dielectric constant oxides. *Eur. Phys. J. Appl. Phys.* **2004,** *28*, 265-291.

(37) John, R., High dielectric constant gate oxides for metal oxide Si transistors. *Rep. Prog. Phys.* **2006,** *69*, 327.

(38) Frunză, R. C.; Kmet, B.; Jankovec, M.; Topič, M.; Malič, B., Ta2O5-based high-K dielectric thin films from solution processed at low temperatures. *Mater. Res. Bull.* **2014,** *50*, 323-328.

(39) Park, J.; Park, B. K.; Cho, M.; Hwang, C. S.; Oh, K.; Yang, D. Y., Chemical Vapor Deposition of HfO2 Thin Films Using a Novel Carbon-Free Precursor: Characterization of the Interface with the Silicon Substrate. *J. Electrochem. Soc.* **2002,** *149*, G89-G94.

(40) Koo, J. B.; Lim, J. W.; Kim, S. H.; Yun, S. J.; Ku, C. H.; Lim, S. C.; Lee, J. H., Pentacene thin-film transistors and inverters with plasma-enhanced atomic-layer-deposited Al2O3 gate dielectric. *Thin Solid Films* **2007,** *515*, 3132-3137.

(41) Liao, M.; Ishiwara, H.; Ohmi, S., Excellent Current Drivability and Environmental Stability in Room-Temperature-Fabricated Pentacene-Based Organic Field-Effect Transistors With HfO_2 Gate Insulators. *IEEE Transactions on Electron Devices* **2014,** *61*, 569-575.

(42) Park, N.-G., Perovskite solar cells: an emerging photovoltaic technology. *Mater. Today* **2015,** *18*, 65-72.

(43) Shirasaki, Y.; Supran, G. J.; Bawendi, M. G.; Bulović, V., Emergence of colloidal quantum-dot light-emitting technologies. *Nat. Photonics* **2012,** *7*, 13.

(44) Tetzner, K.; Schroder, K. A.; Bock, K., Photonic curing of sol–gel derived HfO2 dielectrics for organic field-effect transistors. *Ceram. Int.* **2014,** *40*, 15753-15761.

(45) Suzuki, K.; Kato, K., Sol–Gel Synthesis of High-k HfO2 Thin Films. *J. Am. Ceram. Soc.* **2008,**

92, S162-S164.

(46) He, W.; Xu, W.; Peng, Q.; Liu, C.; Zhou, G.; Wu, S.; Zeng, M.; Zhang, Z.; Gao, J.; Gao, X.; Lu, X.; Liu, J. M., Surface Modification on Solution Processable ZrO2 High-k Dielectrics for Low Voltage Operations of Organic Thin Film Transistors. *J. Phys. Chem. C* **2016,** *120*, 9949-9957.

(47) Esro, M.; Vourlias, G.; Somerton, C.; Milne, W. I.; Adamopoulos, G., High-Mobility ZnO Thin Film Transistors Based on Solution-processed Hafnium Oxide Gate Dielectrics. *Adv. Funct. Mater.* **2014,** *25*, 134-141.

(48) Ndiege, N.; Wilhoite, T.; Subramanian, V.; Shannon, M. A.; Masel, R. I., Sol−Gel Synthesis of Thick Ta2O5 Films. *Chem. Mater.* **2007,** *19*, 3155-3161.

(49) Gritsenko, V. A.; Perevalov, T. V.; Islamov, D. R., Electronic properties of hafnium oxide: A contribution from defects and traps. *Phys. Rep.* **2016,** *613*, 1-20.

(50) Barreca, D.; Milanov, A.; Fischer, R. A.; Devi, A.; Tondello, E., Hafnium oxide thin film grown by ALD: An XPS study. *Surf. Sci. Spectra* **2007,** *14*, 34-40.

(51) Kumar, S.; Kumar, S.; Tiwari, S.; Srivastava, S.; Srivastava, M.; Yadav, B. K.; Kumar, S.; Tran, T. T.; Dewan, A. K.; Mulchandani, A.; Sharma, J. G.; Maji, S.; Malhotra, B. D., Biofunctionalized Nanostructured Zirconia for Biomedical Application: A Smart Approach for Oral Cancer Detection. *Adv. Sci.* **2015,** *2*, 1500048.

(52) Brenier, R.; Mugnier, J.; Mirica, E., XPS study of amorphous zirconium oxide films prepared by sol–gel. *Appl. Surf. Sci.* **1999,** *143*, 85-91.

(53) Nilgün, Ö.; Yongxiang, H.; Carl, M. L. In *Characterization of Tantalum Oxide Films Prepared by Sol-Gel Process for electrochemical devices*, 1994/.

(54) Krishnan, S.; Stefanakos, E.; Bhansali, S., Effects of dielectric thickness and contact area on current–voltage characteristics of thin film metal–insulator–metal diodes. *Thin Solid Films* **2008,** *516*, 2244-2250.

(55) Kukli, K.; Forsgren, K.; Ritala, M.; Leskelä, M.; Aarik, J.; Haårsta, A., Dielectric Properties of Zirconium Oxide Grown by Atomic Layer Deposition from Iodide Precursor. *J. Electrochem. Soc.* **2001,** *148*, F227-F232.

(56) Martinez-Duart, J. M.; Velilla, J. L.; Albella, J. M.; Rueda, F., Dielectric properties of thin Ta2O5 films. *Phys. Status Solidi A* **1974,** *26*, 611-615.

(57) Arreola-Jardón, G.; González, L. A.; García-Cerda, L. A.; Gnade, B.; Quevedo-López, M. A.; Ramírez-Bon, R., Ammonia-free chemically deposited CdS films as active layers in thin film transistors. *Thin Solid Films* **2010,** *519*, 517-520.

(58) Gan, F. Y.; Shih, I., Preparation of thin-film transistors with chemical bath deposited CdSe and CdS thin films. *IEEE Trans. Electron Devices* **2002,** *49*, 15-18.

(59) Marjanovic, N.; Hammerschmidt, J.; Perelaer, J.; Farnsworth, S.; Rawson, I.; Kus, M.; Yenel, E.; Tilki, S.; Schubert, U. S.; Baumann, R. R., Inkjet printing and low temperature sintering of CuO and

CdS as functional electronic layers and Schottky diodes. *J. Mater. Chem.* **2011,** *21*, 13634-13639.

(60) Meth, J. S.; Zane, S. G.; Sharp, K. G.; Agrawal, S., Patterned thin film transistors incorporating chemical bath deposited cadmium sulfide as the active layer. *Thin Solid Films* **2003,** *444*, 227-234.

(61) Perez, M. R.; Mejia, I.; Salas-Villasenor, A. L.; Stiegler, H.; Trachtenberg, I.; Gnade, B. E.; Quevedo-Lopez, M. A., Hybrid CMOS thin-film devices based on solution-processed CdS n-TFTs and TIPS-Pentacene p-TFTs. *Org. Electron.* **2012,** *13*, 3045-3049.

(62) Voss, C.; Subramanian, S.; Chang, C. H., Cadmium sulfide thin-film transistors fabricated by low-temperature chemical-bath deposition. *J. Appl. Phys.* **2004,** *96*, 5819-5823.

(63) Fritz, S. E.; Kelley, T. W.; Frisbie, C. D., Effect of Dielectric Roughness on Performance of Pentacene TFTs and Restoration of Performance with a Polymeric Smoothing Layer. *J. Phys. Chem. B* **2005,** *109*, 10574-10577.

(64) Stassen, A. F.; de Boer, R. W. I.; Iosad, N. N.; Morpurgo, A. F., Influence of the gate dielectric on the mobility of rubrene single-crystal field-effect transistors. *Appl. Phys. Lett.* **2004,** *85*, 3899-3901.

(65) Li, G.; Zhu, R.; Yang, Y., Polymer solar cells. *Nat. Photonics* **2012,** *6*, 153.

(66) von Hauff, E.; Dyakonov, V.; Parisi, J., Study of field effect mobility in PCBM films and P3HT:PCBM blends. *Sol. Energy Mater. Sol. Cells* **2005,** *87*, 149-156.

(67) Manoli, K.; Patrikoussakis, M. M.; Magliulo, M.; Dumitru, L. M.; Mulla, M. Y.; Sabbatini, L.; Torsi, L., Pulsed voltage driven organic field-effect transistors for high stability transient current measurements. *Org. Electron.* **2014,** *15*, 2372-2380.

(68) Sun, Y.; Rogers, J. A., Inorganic Semiconductors for Flexible Electronics. *Adv. Mater.* **2007,** *19*, 1897-1916.

(69) Arias, A. C.; MacKenzie, J. D.; McCulloch, I.; Rivnay, J.; Salleo, A., Materials and Applications for Large Area Electronics: Solution-Based Approaches. *Chem. Rev.* **2010,** *110*, 3-24.

(70) Schwierz, F., Graphene transistors. *Nat. Nanotechnol.* **2010,** *5*, 487.

(71) Ridley, B. A.; Nivi, B.; Jacobson, J. M., All-Inorganic Field Effect Transistors Fabricated by Printing. *Science* **1999,** *286*, 746.

(72) Talapin, D. V.; Lee, J.-S.; Kovalenko, M. V.; Shevchenko, E. V., Prospects of Colloidal Nanocrystals for Electronic and Optoelectronic Applications. *Chem. Rev.* **2010,** *110*, 389-458.

(73) Radisavljevic, B.; Radenovic, A.; Brivio, J.; Giacometti, V.; Kis, A., Single-layer MoS2 transistors. *Nat. Nanotechnol.* **2011,** *6*, 147.

(74) Zuleeg, R., Electrical evaluation of thin film CdS diodes and transistors. *Solid-State Electron.* **1963,** *6*, 645-655.

(75) Ma, R. M.; Dai, L.; Huo, H. B.; Yang, W. Q.; Qin, G. G.; Tan, P. H.; Huang, C. H.; Zheng, J., Synthesis of high quality n-type CdS nanobelts and their applications in nanodevices. *Appl. Phys. Lett.* **2006,** *89*, 203120.

(76) Lee, J.-S.; Kovalenko, M. V.; Huang, J.; Chung, D. S.; Talapin, D. V., Band-like transport, high

electron mobility and high photoconductivity in all-inorganic nanocrystal arrays. *Nature Nanotechnology* **2011,** *6*, 348.

(77) Chung, D. S.; Lee, J.-S.; Huang, J.; Nag, A.; Ithurria, S.; Talapin, D. V., Low Voltage, Hysteresis Free, and High Mobility Transistors from All-Inorganic Colloidal Nanocrystals. *Nano Lett.* **2012,** *12*, 1813-1820.

(78) Simon, U., Charge Transport in Nanoparticle Arrangements. *Adv. Mater.* **1999,** *10*, 1487-1492.

(79) Mitzi, D. B.; Copel, M.; Chey, S. J., Low-Voltage Transistor Employing a High-Mobility Spin-Coated Chalcogenide Semiconductor. *Adv. Mater.* **2005,** *17*, 1285-1289.

(80) Seon, J.-B.; Lee, S.; Kim, J. M.; Jeong, H.-D., Spin-Coated CdS Thin Films for n-Channel Thin Film Transistors. *Chem. Mater.* **2009,** *21*, 604-611.

(81) Resta, V.; Laera, A. M.; Piscopiello, E.; Schioppa, M.; Tapfer, L., Highly Efficient Precursors for Direct Synthesis of Tailored CdS Nanocrystals in Organic Polymers. *J. Phys. Chem. C* **2010,** *114*, 17311-17317.

(82) Lu, W.; Chen, M.; Wu, L., Easy method for preparing nanocrystalline CdS hollow spheres using miniemulsion droplets as templates. *J. Colloid Interface Sci.* **2008,** *324*, 220-224.

(83) Khon, E.; Lambright, S.; Khon, D.; Smith, B.; O'Connor, T.; Moroz, P.; Imboden, M.; Diederich, G.; Perez-Bolivar, C.; Anzenbacher, P.; Zamkov, M., Inorganic Solids of CdSe Nanocrystals Exhibiting High Emission Quantum Yield. *Adv. Funct. Mater.* **2012,** *22*, 3714-3722.

(84) Di Benedetto, F.; Camposeo, A.; Persano, L.; Laera, A. M.; Piscopiello, E.; Cingolani, R.; Tapfer, L.; Pisignano, D., Light-emitting nanocomposite CdS–polymer electrospun fibres via in situ nanoparticle generation. *Nanoscale* **2011,** *3*, 4234-4239.

(85) Antolini, F.; Ghezelbash, A.; Esposito, C.; Trave, E.; Tapfer, L.; Korgel, B. A., Laser-induced nanocomposite formation for printed nanoelectronics. *Mater. Lett.* **2006,** *60*, 1095-1098.

(86) Masala, S.; Del Gobbo, S.; Borriello, C.; Bizzarro, V.; La Ferrara, V.; Re, M.; Pesce, E.; Minarini, C.; De Crescenzi, M.; Di Luccio, T., Hybrid polymer-CdS solar cell active layers formed by in situ growth of CdS nanoparticles. *J. Nanopart. Res.* **2011,** *13*, 6537-6544.

(87) Kräuter, G.; Rees, W. S., Cadmium bis(alkylthiolate) complexes as precursors for cadmium sulfide: a mild route to hawleyite. *J. Mater. Chem.* **1995,** *5*, 1265-1267.

(88) Rees, W. S.; Kräuter, G., Preparation and characterization of several group 12 element (Zn, Cd)-bis(thiolate) complexes and evaluation of their potential as precursors for 12–16 semiconducting materials. *J. Mater. Res.* **1996,** *11*, 3005-3016.

(89) Bube, R. H., The Basic Significance of Oxygen Chemisorption on the Photoelectronic Properties of CdS and CdSe. *J. Electrochem. Soc.* **1966,** *113*, 793-798.

(90) Gu, Y.; Lauhon, L. J., Space-charge-limited current in nanowires depleted by oxygen adsorption. *Appl. Phys. Lett.* **2006,** *89*, 143102.

(91) Liang, Y.; Xu, Z.; Xia, J.; Tsai, S.-T.; Wu, Y.; Li, G.; Ray, C.; Yu, L., For the Bright Future—

Bulk Heterojunction Polymer Solar Cells with Power Conversion Efficiency of 7.4%. *Adv. Mater.* **2010,** *22*, E135-E138.

(92) Beek, W. J. E.; Slooff, L. H.; Wienk, M. M.; Kroon, J. M.; Janssen, R. A. J., Hybrid Solar Cells Using a Zinc Oxide Precursor and a Conjugated Polymer. *Adv. Funct. Mater.* **2005,** *15*, 1703-1707.

(93) Masson, G. M., M.; Orlandi, S. Snapshot of Global PV. (accessed Apr/12).

(94) Edenhofer, O. P.-M., R.; Sokona, Y.; Minx, J. C.; Farahani, E.; Kadner, S.; Seyboth, K.; Adler, A.; Baum, I; Brunner, S.; Eickemeier, P.; Kriemann, B.; Savolainen, J.; Schlomer, S.; Stechow, C. v.; Zwickel, T., *Climate Change 2014: Mitigation of Climate Change. Contribution of Working Group III to the Fifth Assessment Report of the Intergovernmental Panel on Climate Change*. Cambridge University Press: 2014.

(95) Lu, L.; Zheng, T.; Wu, Q.; Schneider, A. M.; Zhao, D.; Yu, L., Recent Advances in Bulk Heterojunction Polymer Solar Cells. *Chem. Rev.* **2015,** *115*, 12666-12731.

(96) Lee, C.-P.; Lin, R. Y.-Y.; Lin, L.-Y.; Li, C.-T.; Chu, T.-C.; Sun, S.-S.; Lin, J. T.; Ho, K.-C., Recent progress in organic sensitizers for dye-sensitized solar cells. *RSC Adv.* **2015,** *5*, 23810-23825.

(97) Carey, G. H.; Abdelhady, A. L.; Ning, Z.; Thon, S. M.; Bakr, O. M.; Sargent, E. H., Colloidal Quantum Dot Solar Cells. *Chem. Rev.* **2015,** *115*, 12732-12763.

(98) Lewerenz, H. J.; Goslowsky, H.; Husemann, K. D.; Fiechter, S., Efficient solar energy conversion with CuInS2. *Nature* **1986,** *321*, 687.

(99) Jackson, P.; Hariskos, D.; Lotter, E.; Paetel, S.; Wuerz, R.; Menner, R.; Wischmann, W.; Powalla, M., New world record efficiency for Cu(In,Ga)Se2 thin-film solar cells beyond 20%. *Prog. Photovoltaics* **2011,** *19*, 894-897.

(100) Contreras, M. A.; Tuttle, J.; Gabor, A.; Tennant, A.; Ramanathan, K.; Asher, S.; Franz, A.; Keane, J.; Wang, L.; Scofield, J.; Noufi, R. In *High efficiency Cu(In,Ga)Se/sub 2/-based solar cells: processing of novel absorber structures*, Proceedings of 1994 IEEE 1st World Conference on Photovoltaic Energy Conversion - WCPEC (A Joint Conference of PVSC, PVSEC and PSEC), 5-9 Dec. 1994; 1994; pp 68-75 vol.1.

(101) Hou, W. W.; Bob, B.; Li, S.-h.; Yang, Y., Low-temperature processing of a solution-deposited CuInSSe thin-film solar cell. *Thin Solid Films* **2009,** *517*, 6853-6856.

(102) Todorov, T. K.; Gunawan, O.; Gokmen, T.; Mitzi, D. B., Solution-processed Cu(In,Ga)(S,Se)2 absorber yielding a 15.2% efficient solar cell. *Proc. Photovoltaics* **2012,** *21*, 82-87.

(103) Panthani, M. G.; Akhavan, V.; Goodfellow, B.; Schmidtke, J. P.; Dunn, L.; Dodabalapur, A.; Barbara, P. F.; Korgel, B. A., Synthesis of CuInS2, CuInSe2, and Cu(InxGa1-x)Se2 (CIGS) Nanocrystal "Inks" for Printable Photovoltaics. *J. Am. Chem. Soc.* **2008,** *130*, 16770-16777.

(104) Kolny-Olesiak, J.; Weller, H., Synthesis and Application of Colloidal CuInS2 Semiconductor Nanocrystals. *ACS Appl. Mater. Interfaces* **2013,** *5*, 12221-12237.

(105) Akhavan, V. A.; Goodfellow, B. W.; Panthani, M. G.; Reid, D. K.; Hellebusch, D. J.; Adachi, T.;

Korgel, B. A., Spray-deposited CuInSe2 nanocrystal photovoltaics. *Energy Environ. Sci.* **2010,** *3*, 1600-1606.

(106) Wang, G.; Wang, S.; Cui, Y.; Pan, D., A Novel and Versatile Strategy to Prepare Metal–Organic Molecular Precursor Solutions and Its Application in Cu(In,Ga)(S,Se)2 Solar Cells. *Chem. Mater.* **2012,** *24*, 3993-3997.

(107) Rath, T.; Edler, M.; Haas, W.; Fischereder, A.; Moscher, S.; Schenk, A.; Trattnig, R.; Sezen, M.; Mauthner, G.; Pein, A.; Meischler, D.; Bartl, K.; Saf, R.; Bansal, N.; Haque, S. A.; Hofer, F.; List, E. J. W.; Trimmel, G., A Direct Route Towards Polymer/Copper Indium Sulfide Nanocomposite Solar Cells. *Adv. Energy Mater.* **2011,** *1*, 1046-1050.

(108) Mario, A.; Manfred, G.; Michael, E.; Wernfried, H.; Ferdinand, H.; Neha, B.; Luke, X. R.; Saif, A. H.; Karin, Z.; Gregor, T.; Thomas, R., Influence of morphology and polymer:nanoparticle ratio on device performance of hybrid solar cells—an approach in experiment and simulation. *Nanotechnology* **2013,** *24*, 484005.

(109) Fradler, C.; Rath, T.; Dunst, S.; Letofsky-Papst, I.; Saf, R.; Kunert, B.; Hofer, F.; Resel, R.; Trimmel, G., Flexible polymer/copper indium sulfide hybrid solar cells and modules based on the metal xanthate route and low temperature annealing. *Sol. Energy Mater. Sol. Cells* **2014,** *124*, 117-125.

(110) Castro, S. L.; Bailey, S. G.; Raffaelle, R. P.; Banger, K. K.; Hepp, A. F., Nanocrystalline Chalcopyrite Materials (CuInS2 and CuInSe2) via Low-Temperature Pyrolysis of Molecular Single-Source Precursors. *Chem. Mater.* **2003,** *15*, 3142-3147.

(111) Uhl, A. R.; Katahara, J. K.; Hillhouse, H. W., Molecular-ink route to 13.0% efficient low-bandgap CuIn(S,Se)2 and 14.7% efficient Cu(In,Ga)(S,Se)2 solar cells. *Energy Environ. Sci.* **2016,** *9*, 130-134.

(112) Li, L.; Coates, N.; Moses, D., Solution-Processed Inorganic Solar Cell Based on in Situ Synthesis and Film Deposition of CuInS2 Nanocrystals. *J. Am. Chem. Soc.* **2010,** *132*, 22-23.

(113) Rawal, V. H.; Cava, M. P., Thermolytic removal of t-butyloxycarbonyl (BOC) protecting group on indoles and pyrroles. *Tetrahedron Lett.* **1985,** *26*, 6141-6142.

(114) Zambounis, J. S.; Hao, Z.; Iqbal, A., Latent pigments activated by heat. *Nature* **1997,** *388*, 131.

(115) Sytnyk, M.; Głowacki, E. D.; Yakunin, S.; Voss, G.; Schöfberger, W.; Kriegner, D.; Stangl, J.; Trotta, R.; Gollner, C.; Tollabimazraehno, S.; Romanazzi, G.; Bozkurt, Z.; Havlicek, M.; Sariciftci, N. S.; Heiss, W., Hydrogen-Bonded Organic Semiconductor Micro- And Nanocrystals: From Colloidal Syntheses to (Opto-)Electronic Devices. *J. Am. Chem. Soc.* **2014,** *136*, 16522-16532.

(116) Lee, J.; Han, A. R.; Hong, J.; Seo, J. H.; Oh, J. H.; Yang, C., Inversion of Dominant Polarity in Ambipolar Polydiketopyrrolopyrrole with Thermally Removable Groups. *Adv. Funct. Mater.* **2012,** *22*, 4128-4138.

(117) WebBook, N. C. NIST Standard Reference Database Number 69. (accessed 18th April).

(118) Bryant, M. A.; Pemberton, J. E., Surface Raman scattering of self-assembled monolayers formed

from 1-alkanethiols: behavior of films at gold and comparison to films at silver. *J. Am. Chem. Soc.* **1991,** *113*, 8284-8293.

(119) Ken-ichi, K.; Susumu, N.; Katsuaki, S., Raman Scattering Studies of CuInS 2 Films Grown by RF Ion Plating. *Jpn. J. Appl. Phys.* **1998,** *37*, 5728.

(120) Alvarez-García, J.; Pérez-Rodríguez, A.; Romano-Rodríguez, A.; Jawhari, T.; Morante, J. R.; Scheer, R.; Calvet, W., Raman scattering structural evaluation of CuInS2 thin films. *Thin Solid Films* **2001,** *387*, 216-218.

(121) Mane, R. S.; Lokhande, C. D., Studies on structural, optical and electrical properties of indium sulfide thin films. *Mater. Chem. Phys.* **2003,** *78*, 15-17.

(122) Izadneshan, H.; Gremenok, V. F., Influence of Annealing on the Optical Parameters of In2S3 Thin Films Produced by Thermal Evaporation. *J. Appl. Spectrosc.* **2014,** *81*, 293-296.

(123) Scheunemann, D.; Wilken, S.; Parisi, J.; Borchert, H., Towards depleted heterojunction solar cells with CuInS2 and ZnO nanocrystals. *Appl. Phys. Lett.* **2013,** *103*, 133902.

(124) Chen, L.-M.; Hong, Z.; Li, G.; Yang, Y., Recent Progress in Polymer Solar Cells: Manipulation of Polymer:Fullerene Morphology and the Formation of Efficient Inverted Polymer Solar Cells. *Adv. Mater.* **2009,** *21*, 1434-1449.

(125) Atwater, H. A.; Polman, A., Plasmonics for improved photovoltaic devices. *Nat. Mater.* **2010,** *9*, 205.

(126) Linic, S.; Christopher, P.; Ingram, D. B., Plasmonic-metal nanostructures for efficient conversion of solar to chemical energy. *Nat. Mater.* **2011,** *10*, 911.

(127) Petoukhoff, C. E.; O'Carroll, D. M., Absorption-induced scattering and surface plasmon out-coupling from absorber-coated plasmonic metasurfaces. *Nat. Commun.* **2015,** *6*, 7899.

(128) Yao, M.; Shen, P.; Liu, Y.; Chen, B.; Guo, W.; Ruan, S.; Shen, L., Performance Improvement of Polymer Solar Cells by Surface-Energy-Induced Dual Plasmon Resonance. *ACS Appl. Mater. Interfaces* **2016,** *8*, 6183-6189.

(129) Yao, K.; Salvador, M.; Chueh, C.-C.; Xin, X.-K.; Xu, Y.-X.; deQuilettes, D. W.; Hu, T.; Chen, Y.; Ginger, D. S.; Jen, A. K. Y., A General Route to Enhance Polymer Solar Cell Performance using Plasmonic Nanoprisms. *Adv. Energy Mater.* **2014,** *4*, 1400206.

(130) Baek, S.-W.; Noh, J.; Lee, C.-H.; Kim, B.; Seo, M.-K.; Lee, J.-Y., Plasmonic Forward Scattering Effect in Organic Solar Cells: A Powerful Optical Engineering Method. *Sci. Rep.* **2013,** *3*, 1726.

(131) Fan, X.; Zheng, W.; Singh, D. J., Light scattering and surface plasmons on small spherical particles. *Light Sci. Appl.* **2014,** *3*, e179.

(132) T. Draine, B., *The Discrete-Dipole Approximation and Its Application to Interstellar Graphite Grains*. 1988; Vol. 333, p 848-872.

(133) Draine, B. T.; Flatau, P. J., Discrete-Dipole Approximation For Scattering Calculations. *J. Opt. Soc. Am. A* **1994,** *11*, 1491-1499.

(134) Bass, M. D., C.; Enoch, J.; Lakshminarayanan, V.; Li, G.; MacDonald, C.; Mahajan, V.; Van Stryland, E., *Handbook of Optics, Third ed.: Optical Properties of Materials, Nonlinear Optics, Quantum Optics (Set)*. McGraw-Hill Education: New York, 2009; Vol. 4.

(135) Bond, W. L., Measurement of the Refractive Indices of Several Crystals. *J. Appl. Phys.* **1965,** *36*, 1674-1677.

(136) Lucía, B. S.; Jorge, O. T., Size dependence of refractive index of gold nanoparticles. *Nanotechnology* **2006,** *17*, 1309.

(137) Palik, E. D., *Handbook of Optical Constants of Solids*. Academic Press: Orlando, 1985.

(138) Ashcroft, N. W. M., N. D. , *Solid State Physics, International Edition*. Holt-Saunders: Philadelphia, 1976.

(139) Coronado, E. A.; Schatz, G. C., Surface plasmon broadening for arbitrary shape nanoparticles: A geometrical probability approach. *J. Chem. Phys.* **2003,** *119*, 3926-3934.

(140) McMahon, J. M.; Gray, S. K.; Schatz, G. C., Calculating nonlocal optical properties of structures with arbitrary shape. *Phys. Rev. B* **2010,** *82*, 035423.

(141) McMahon, J. M.; Gray, S. K.; Schatz, G. C., Nonlocal Optical Response of Metal Nanostructures with Arbitrary Shape. *Phys. Rev. Lett.* **2009,** *103*, 097403.

(142) Heo, M.; Cho, H.; Jung, J.-W.; Jeong, J.-R.; Park, S.; Kim, J. Y., High-Performance Organic Optoelectronic Devices Enhanced by Surface Plasmon Resonance. *Adv. Mater.* **2011,** *23*, 5689-5693.

(143) Cho, H.; Choi, S.; Kim, J. Y.; Park, S., Fabrication of gold dot, ring, and corpuscle arrays from block copolymer templates via a simple modification of surface energy. *Nanoscale* **2011,** *3*, 5007-5012.

(144) Wang, J.; Polleux, J.; Lim, J.; Dunn, B., Pseudocapacitive Contributions to Electrochemical Energy Storage in TiO2 (Anatase) Nanoparticles. *J. Phys. Chem. C* **2007,** *111*, 14925-14931.

(145) Beek, W. J. E.; Wienk, M. M.; Kemerink, M.; Yang, X.; Janssen, R. A. J., Hybrid Zinc Oxide Conjugated Polymer Bulk Heterojunction Solar Cells. *J. Phys. Chem. B* **2005,** *109*, 9505-9516.

(146) Seo, E.; Ko, S.-J.; Min, S. H.; Kim, J. Y.; Kim, B.-S., Plasmonic Transition via Interparticle Coupling of Au@Ag Core–Shell Nanostructures Sheathed in Double Hydrophilic Block Copolymer for High-Performance Polymer Solar Cell. *Chem. Mater.* **2015,** *27*, 4789-4798.

(147) Choi, H.; Lee, J.-P.; Ko, S.-J.; Jung, J.-W.; Park, H.; Yoo, S.; Park, O.; Jeong, J.-R.; Park, S.; Kim, J. Y., Multipositional Silica-Coated Silver Nanoparticles for High-Performance Polymer Solar Cells. *Nano Lett.* **2013,** *13*, 2204-2208.

(148) Choi, H.; Ko, S.-J.; Choi, Y.; Joo, P.; Kim, T.; Lee, B. R.; Jung, J.-W.; Choi, H. J.; Cha, M.; Jeong, J.-R.; Hwang, I.-W.; Song, M. H.; Kim, B.-S.; Kim, J. Y., Versatile surface plasmon resonance of carbon-dot-supported silver nanoparticles in polymer optoelectronic devices. *Nat. Photonics* **2013,** *7*, 732.

(149) Xu, W.; Min, X.; Chen, X.; Zhu, Y.; Zhou, P.; Cui, S.; Xu, S.; Tao, L.; Song, H., Ag-SiO2-Er2O3 Nanocomposites: Highly Effective Upconversion Luminescence at High Power Excitation and High

Temperature. *Sci. Rep.* **2014,** *4*, 5087.

(150) Pillai, S.; Catchpole, K. R.; Trupke, T.; Green, M. A., Surface plasmon enhanced silicon solar cells. *J. Appl. Phys.* **2007,** *101*, 093105.

(151) Attia, Y. A.; Buceta, D.; Requejo, F. G.; Giovanetti, L. J.; López-Quintela, M. A., Photostability of gold nanoparticles with different shapes: the role of Ag clusters. *Nanoscale* **2015,** *7*, 11273-11279.

(152) Boix, P. P.; Ajuria, J.; Etxebarria, I.; Pacios, R.; Garcia-Belmonte, G.; Bisquert, J., Role of ZnO Electron-Selective Layers in Regular and Inverted Bulk Heterojunction Solar Cells. *J. Phys. Chem. Lett.* **2011,** *2*, 407-411.

(153) Kim, J. Y.; Kim, S. H.; Lee, H. H.; Lee, K.; Ma, W.; Gong, X.; Heeger, A. J., New Architecture for High-Efficiency Polymer Photovoltaic Cells Using Solution-Based Titanium Oxide as an Optical Spacer. *Adv. Mater.* **2006,** *18*, 572-576.

(154) Wu, B.; Wu, X.; Guan, C.; Fai Tai, K.; Yeow, E. K. L.; Jin Fan, H.; Mathews, N.; Sum, T. C., Uncovering loss mechanisms in silver nanoparticle-blended plasmonic organic solar cells. *Nat. Commun.* **2013,** *4*, 2004.

(155) Fung, D. D. S.; Qiao, L.; Choy, W. C. H.; Wang, C.; Sha, W. E. I.; Xie, F.; He, S., Optical and electrical properties of efficiency enhanced polymer solar cells with Au nanoparticles in a PEDOT–PSS layer. *J. Mater. Chem.* **2011,** *21*, 16349-16356.

(156) Lee, Y.-C.; Huang, C.-F.; Chang, J.-Y.; Wu, M.-L., Enhanced light trapping based on guided mode resonance effect for thin-film silicon solar cells with two filling-factor gratings. *Opt. Express* **2008,** *16*, 7969-7975.

(157) Khaleque, T.; Magnusson, R. In *Light management through guided-mode resonances in thin-film silicon solar cells*, SPIE: 2014; p 14.

(158) Miller, P. H., The Electrical Conductivity of Zinc Oxide. *Phys. Rev.* **1941,** *60*, 890-895.

(159) Kislov, N.; Lahiri, J.; Verma, H.; Goswami, D. Y.; Stefanakos, E.; Batzill, M., Photocatalytic Degradation of Methyl Orange over Single Crystalline ZnO: Orientation Dependence of Photoactivity and Photostability of ZnO. *Langmuir* **2009,** *25*, 3310-3315.

(160) Han, C.; Yang, M. Q.; Weng, B.; Xu, Y. J., Improving the photocatalytic activity and anti-photocorrosion of semiconductor ZnO by coupling with versatile carbon. *Phys. Chem. Chem. Phys.* **2014,** *16*, 16891-16903.

(161) Wang, Y. J.; Shi, R.; Lin, J.; Zhu, Y. F., Enhancement of photocurrent and photocatalytic activity of ZnO hybridized with graphite-like C3N4. *Energy Environ. Sci.* **2011,** *4*, 2922-2929.

(162) Paracchino, A.; Laporte, V.; Sivula, K.; Gratzel, M.; Thimsen, E., Highly active oxide photocathode for photoelectrochemical water reduction. *Nat. Mater.* **2011,** *10*, 456-461.

(163) Janotti, A.; Van de Walle, C. G., Fundamentals of zinc oxide as a semiconductor. *Rep. Prog. Phys.* **2009,** *72*, 29.

(164) Lin, B. X.; Fu, Z. X.; Jia, Y. B., Green luminescent center in undoped zinc oxide films deposited

on silicon substrates. *Appl. Phys. Lett.* **2001,** *79*, 943-945.

(165) Carcia, P. F.; McLean, R. S.; Reilly, M. H.; Nunes, G., Transparent ZnO thin-film transistor fabricated by rf magnetron sputtering. *Appl. Phys. Lett.* **2003,** *82*, 1117-1119.

(166) Sun, Y. M.; Seo, J. H.; Takacs, C. J.; Seifter, J.; Heeger, A. J., Inverted Polymer Solar Cells Integrated with a Low-Temperature-Annealed Sol-Gel-Derived ZnO Film as an Electron Transport Layer. *Adv. Mater.* **2011,** *23*, 1679.

(167) Ohyama, M.; Kozuka, H.; Yoko, T., Sol-gel preparation of ZnO films with extremely preferred orientation along (002) plane from zinc acetate solution. *Thin Solid Films* **1997,** *306*, 78-85.

(168) Lee, J. H.; Ko, K. H.; Park, B. O., Electrical and optical properties of ZnO transparent conducting films by the sol-gel method. *J. Cryst. Growth* **2003,** *247*, 119-125.

(169) Jeong, J.; Kim, H.; Yoon, Y. J.; Walker, B.; Song, S.; Heo, J.; Park, S. Y.; Kim, J. W.; Kim, G.-H.; Kim, J. Y., Formamidinium-based planar heterojunction perovskite solar cells with alkali carbonate-doped zinc oxide layer. *RSC Adv.* **2018,** *8*, 24110-24115.

(170) Beek, W. J. E.; Wienk, M. M.; Janssen, R. A. J., Efficient hybrid solar cells from zinc oxide nanoparticles and a conjugated polymer. *Adv. Mater.* **2004,** *16*, 1009-+.

(171) Jung, S.; Lee, J.; Seo, J.; Kim, U.; Choi, Y.; Park, H., Development of Annealing-Free, Solution-Processable Inverted Organic Solar Cells with N-Doped Graphene Electrodes using Zinc Oxide Nanoparticles. *Nano Lett.* **2018,** *18*, 1337-1343.

(172) Liu, X.; Swihart, M. T., A general single-pot heating method for morphology, size and luminescence-controllable synthesis of colloidal ZnO nanocrystals. *Nanoscale* **2013,** *5*, 8029-8036.

(173) Cozzoli, P. D.; Kornowski, A.; Weller, H., Colloidal Synthesis of Organic-Capped ZnO Nanocrystals via a Sequential Reduction−Oxidation Reaction. *J. Phys. Chem. B* **2005,** *109*, 2638-2644.

(174) Sun, D.; Wong, M.; Sun, L.; Li, Y.; Miyatake, N.; Sue, H.-J., Purification and stabilization of colloidal ZnO nanoparticles in methanol. *J. Sol-Gel Sci. Technol.* **2007,** *43*, 237-243.

(175) Li, P.; Jiu, T.; Tang, G.; Wang, G.; Li, J.; Li, X.; Fang, J., Solvents Induced ZnO Nanoparticles Aggregation Associated with Their Interfacial Effect on Organic Solar Cells. *ACS Appl. Mater. Interfaces* **2014,** *6*, 18172-18179.

(176) Li, C.; Sun, X.; Ni, J.; Huang, L.; Xu, R.; Li, Z.; Cai, H.; Li, J.; Zhang, Y.; Zhang, J., Methanol solvent treatment: A simple strategy to significantly boost efficiency and stability of air-processed ternary organic solar cells based on PTB7-Th:PCDTBT:PC70BM. *Org. Electron.* **2017,** *50*, 63-69.

(177) Guo, S.; Cao, B.; Wang, W.; Moulin, J.-F.; Müller-Buschbaum, P., Effect of Alcohol Treatment on the Performance of PTB7:PC71BM Bulk Heterojunction Solar Cells. *ACS Appl. Mater. Interfaces* **2015,** *7*, 4641-4649.

(178) Guo, B.; Zhou, W.; Wu, M.; Lv, J.; Yu, C.; Li, F.; Hu, Z., Improving the efficiency of polymer solar cells via a treatment of methanol : water on the active layers. *J. Mater. Chem. A* **2016,** *4*, 9644-9652.

(179) Liao, S.-H.; Jhuo, H.-J.; Cheng, Y.-S.; Chen, S.-A., Fullerene Derivative-Doped Zinc Oxide Nanofilm as the Cathode of Inverted Polymer Solar Cells with Low-Bandgap Polymer (PTB7-Th) for High Performance. *Adv. Mater.* **2013,** *25*, 4766-4771.

(180) Pacholski, C.; Kornowski, A.; Weller, H., Self-Assembly of ZnO: From Nanodots to Nanorods. *Angew. Chem., Int. Ed.* **2002,** *41*, 1188-1191.

(181) Beek, W. J. E.; Wienk, M. M.; Kemerink, M.; Yang, X.; Janssen, R. A. J., Hybrid Zinc Oxide Conjugated Polymer Bulk Heterojunction Solar Cells. *J. Phys. Chem. B* **2005,** *109*, 9505-9516.

(182) Jong-Jin, L.; Jungsik, B.; Heesun, Y., Highly stable colloidal ZnO nanocrystals by MgO passivation. *J. Phys. D: Appl. Phys.* **2009,** *42*, 025305.

(183) Fabbri, F.; Villani, M.; Catellani, A.; Calzolari, A.; Cicero, G.; Calestani, D.; Calestani, G.; Zappettini, A.; Dierre, B.; Sekiguchi, T.; Salviati, G., Zn vacancy induced green luminescence on non-polar surfaces in ZnO nanostructures. *Sci. Rep.* **2014,** *4*, 5158.

(184) Wang, X. J.; Vlasenko, L. S.; Pearton, S. J.; Chen, W. M.; Buyanova, I. A., Oxygen and zinc vacancies in as-grown ZnO single crystals. *J. Phys. D: Appl. Phys.* **2009,** *42*, 175411.

(185) Janotti, A.; Van de Walle, C. G., Native point defects in ZnO. *Phys. Rev. B* **2007,** *76*, 165202.

(186) Choi, S.; Phillips, M. R.; Aharonovich, I.; Pornsuwan, S.; Cowie, B. C. C.; Ton-That, C., Photophysics of Point Defects in ZnO Nanoparticles. *Adv. Opt. Mater.* **2015,** *3*, 821-827.

(187) Bahers, T. L.; Pauporté, T.; Labat, F.; Lefèvre, G.; Ciofini, I., Acetylacetone, an Interesting Anchoring Group for ZnO-Based Organic−Inorganic Hybrid Materials: A Combined Experimental and Theoretical Study. *Langmuir* **2011,** *27*, 3442-3450.

(188) Smith, A. L., *The Coblentz Society Desk Book of Infrared Spectra, Second Edition*. The Coblentz Society: Kirkwood, MO, 1982.

(189) Villarreal, E.; Li, G. G.; Zhang, Q.; Fu, X.; Wang, H., Nanoscale Surface Curvature Effects on Ligand–Nanoparticle Interactions: A Plasmon-Enhanced Spectroscopic Study of Thiolated Ligand Adsorption, Desorption, and Exchange on Gold Nanoparticles. *Nano Lett.* **2017,** *17*, 4443-4452.

(190) Nakamoto, K.; McCarthy, P. J.; Martell, A. E., Infrared Spectra of Metal Chelate Compounds. III. Infrared Spectra of Acetylacetonates of Divalent Metals1. *J. Am. Chem. Soc.* **1961,** *83*, 1272-1276.

(191) Lawson, K. E., The infrared absorption spectra of metal acetylacetonates. *Spectrochim. Acta* **1961,** *17*, 248-258.

(192) Ilyas, U.; Rawat, R. S.; Tan, T. L.; Lee, P.; Chen, R.; Sun, H. D.; Fengji, L.; Zhang, S., Oxygen rich p-type ZnO thin films using wet chemical route with enhanced carrier concentration by temperature-dependent tuning of acceptor defects. *J. Appl. Phys.* **2011,** *110*, 093522.

(193) Younis, A.; Chu, D.; Li, S., Bi-stable resistive switching characteristics in Ti-doped ZnO thin films. *Nanoscale Res. Lett.* **2013,** *8*, 154.

(194) Chen, H.; Ma, S.; Li, Y.; Ma, L.; Huang, X. In *Microstructures and optical absorption of Ti-doped ZnO films*, 2011 International Conference on Electronics, Communications and Control (ICECC),

9-11 Sept. 2011; 2011; pp 906-909.

(195) Chen, S.; Small, C. E.; Amb, C. M.; Subbiah, J.; Lai, T.-h.; Tsang, S.-W.; Manders, J. R.; Reynolds, J. R.; So, F., Inverted Polymer Solar Cells with Reduced Interface Recombination. *Adv. Energy Mater.* **2012,** *2*, 1333-1337.

(196) Song, X.; Gasparini, N.; Ye, L.; Yao, H.; Hou, J.; Ade, H.; Baran, D., Controlling Blend Morphology for Ultrahigh Current Density in Nonfullerene Acceptor-Based Organic Solar Cells. *ACS Energy Lett.* **2018,** *3*, 669-676.

(197) Li, S.; Ye, L.; Zhao, W.; Zhang, S.; Mukherjee, S.; Ade, H.; Hou, J., Energy-Level Modulation of Small-Molecule Electron Acceptors to Achieve over 12% Efficiency in Polymer Solar Cells. *Adv. Mater.* **2016,** *28*, 9423-9429.

Acknowledgements

6년 6개월의 짧다면 짧고 길다면 길 수 있는 학위 기간을 이렇게 마무리하게 되었습니다. 긴 기간 정말 많은 동료와 교수님들의 도움이 있었습니다. 모두에게 감사하다는 말씀 먼저 드리고 싶습니다. 게으른 제가 이렇게 과분한 성과를 내고 긴 thesis를 가득히 채울 수 있었던 건 모두 덕분입니다.

저는 한 가지에 빠지게 되면 정말 쉽게 집중하고 배우는 편이지만 굉장히 쉽게 싫증을 냅니다. 어릴 적 컴퓨터에 관심이 많아 대학교 진학 후 컴퓨터과학 전공을 하였지만 금세 지겨워져 6개월 뒤 에너지 공학으로 전과하게 되었습니다. 진로에 대한 확신이 없던 시기에 우연히 듣게 된 전자소자 수업에서 지도교수님이신 김진영 교수님을 만나게 된 건 제 인생 최고의 행운이었습니다. 3학년이라는 이른 시기에 연구실 경험을 할 수 있게 되면서 자연스레 목표가 생겨났습니다. 학부에서 화학을 전공하고 온 제가 대학원 전공을 물리학으로 바꾸고 싶다는 억지스러운 요청도 흔쾌히 받아들여 주셔서 제가 꿈에도 그리던 4대 역학을 배울 수 있었고 컴퓨터 시뮬레이션을 배우고 싶다는 말에도 학부의 우수한 교수님들을 소개해주시면서 저의 좁은 견문을 확장해 주셨습니다. 이렇게 다양한 분야의 지식을 배운 덕분인지 실험실에서 집중하는 연구 분야와는 조금 다른 연구 분야에 손을 대었지만 수월하게 해나갈 수 있었고 연구실적도 남부럽지 않게 만들어 냈습니다. 교수님이 아니었다면 대학원에서 이렇게 다양한 경험을 할 수 없었을 거로 생각합니다. 정말 감사합니다.

대학원에 갓 입학한 저에게 교수님은 상당히 유망하지만, 도전적인 주제를 제안해 주시면서 Bright Walker 박사님을 소개해주셨습니다. 지금 와서 얘기해보면 당시 처음 대학원생이 된 저의 연구를 봐주는 사람이 외국인이라는 사실에 조금은 당황했었지만 지금 와서 생각해보면 제 인생의 전환점 아니었나 싶습니다. Bright Walker 박사님은 제 미숙한 연구에 화 한번 안 내시고 자상하게 가르쳐주시고 돌봐주셨습니다. 그뿐만 아니라 소자에 집중하는 실험실 성격상 화학적인 분석에는 부족함이 조금 있었지만, 화학을 전공하셨던 박사님 덕분에 물리와 화학 모두 신경 쓰면서 수월하게 해나갈 수 있었습니다. 정말 감사합니다. 경희대에서도 좋은 결과 많이 내시길 기원하겠습니다.

전, 현 NGEL 멤버들에게도 정말 감사하다는 말씀드리고 싶습니다. 항상 쓴 조언 아끼지 않았던 기환이 형, 힘들 때마다 얘기 들어주고 공감해준 태효 형, 열심히 하고 열정적인 모습으로 후배들에게 좋은 모습 보여준 혜림이 누나, 6개월 선배로서 옆에서 항상 많

은 자극이 되었던 학범이 형, 재기 형, 세영이 누나, 그리고 열심히 고생하면서도 각자의 특기를 키워나가 제 연구에 많은 도움을 줬던 송이, 택호, 강택이 형, 영진이, 나경이, 재원이, 형수, 윤섭이, 혜원이, 그리고 종득이, 지우, 우진이 등 후배들에게도 정말 고맙다는 말 전하고 싶습니다.

학위 논문 심사위원으로서 제 연구를 평가해주시고 조언을 아끼지 않으셨던 박혜성 교수님, 이준희 교수님, 전영철 교수님, 서정화 교수님께도 감사드립니다.

또 유니스트를 갓 입학한 학생에게 연구 기회를 제공해주신 기계항공 및 원자력 공학부 김태성 교수님께 특별히 감사하다는 말씀 전하고 싶습니다. 교수님께서 제공해주신 연구 기회들이 고된 대학원 생활을 헤쳐나갈 수 있는 큰 양분이 되었습니다.

마지막으로 늦은 나이까지 공부하는 아들, 오빠를 믿고 기다려주고 항상 든든하게 지원해주는 우리 가족에게 감사하고 사랑한다고 전하고 싶습니다.

길고 길었던 대학원 생활을 마무리한다고 생각하기 조금 슬프기도 하고 후련하기도 합니다. 앞으로 더 힘든 과정이 남아 있는 걸 누구보다도 잘 알고 있지만 여태까지 도움을 주셨던 많은 분에게 받은 힘으로 계속해서 달려나가고자 합니다. 앞으로도 좋은 연구 성과 많이 내고 좋은 교육 & 연구환경을 제공해준 내 모교 유니스트의 이름에 먹칠하지 않는 허정우 되겠습니다. 다시 한번 감사드립니다.